FLIGHT TESTS OF VIKING PARACHUTE SYSTEM IN THREE MACH NUMBER REGIMES

II - Parachute Test Results

by Richard J. Bendura, Reginald R. Lundstrom,
Philip G. Renfroe, and Stewart R. LeCroy

Langley Research Center
Hampton, Va. 23665

1. Report No. NASA TN D-7734	2. Government Accession No.	3. Recipient's Catalog No.
4. Title and Subtitle FLIGHT TESTS OF VIKING PARACHUTE SYSTEM IN THREE MACH NUMBER REGIMES II – PARACHUTE TEST RESULTS		5. Report Date November 1974
		6. Performing Organization Code
7. Author(s) Richard J. Bendura, Reginald R. Lundstrom, Philip G. Renfroe, and Stewart R. LeCroy		8. Performing Organization Report No. L-9537
9. Performing Organization Name and Address NASA Langley Research Center Hampton, Va. 23665		10. Work Unit No. 815-20-09-03
		11. Contract or Grant No.
12. Sponsoring Agency Name and Address National Aeronautics and Space Administration Washington, D.C. 20546		13. Type of Report and Period Covered Technical Note
		14. Sponsoring Agency Code

16. Abstract

Four tests of the Viking 16.15-meter (53-ft) nominal-diameter disk-gap-band parachute were conducted at Mach number and dynamic pressure conditions which bracketed the range postulated for the Viking '75 mission to Mars. Parachutes were deployed at supersonic, transonic, and subsonic speeds behind a simulated Viking entry capsule. All parachutes successfully deployed, inflated, and exhibited sufficient drag and stability for mission requirements. Basic parachute data including loads, drag coefficients, pull-off angles, and canopy area ratios are presented. Trajectory reconstruction and onboard camera data methods were combined to yield continuous histories of both parachute and test-vehicle angular motions which are presented for the period from parachute deployment through steady inflation.

17. Key Words (Suggested by Author(s)) Parachutes Mars entry High-altitude parachute test Viking	18. Distribution Statement Unclassified – Unlimited STAR Category 31
19. Security Classif. (of this report) Unclassified	20. Security Classif. (of this page) Unclassified

19. Security Classif. (of this report)	20. Security Classif. (of this page)	21. No. of Pages	22. Price*
Unclassified	Unclassified	96	$4.00

FLIGHT TESTS OF VIKING PARACHUTE SYSTEM

IN THREE MACH NUMBER REGIMES

II – PARACHUTE TEST RESULTS

By Richard J. Bendura, Reginald R. Lundstrom,
Philip G. Renfroe,* and Stewart R. LeCroy*
Langley Research Center

SUMMARY

Four flight-qualification tests of the Viking 16.15-meter (53-ft) nominal-diameter disk-gap-band parachute were conducted at Mach number and dynamic pressure conditions which bracketed the range postulated for the Viking '75 mission to Mars. The parachute was deployed at supersonic, transonic, and subsonic velocities in the wake of a full-scale simulated Viking entry capsule and at dynamic pressures from 240 to 675 N/m^2 (5.0 to 14.1 lb/ft^2). Basic parachute data including drag coefficients, loads and related pull-off angles, and canopy projected area ratio variations are presented. The parachutes successfully deployed, inflated, and exhibited acceptable drag and stability characteristics for Viking '75 mission flight-test requirements. Two canopy disk gores were torn during the first supersonic test without any degradation in parachute performance. A dip in the curve of variation of drag coefficient with Mach number was observed at transonic speeds for both the flight-test data and the wind-tunnel tests. Wind-tunnel drag coefficients were less than flight results throughout the transonic and supersonic Mach number ranges. Separation of the aeroshell from the remainder of the test vehicle occurred successfully for all tests and had no effect on parachute performance or stability. To give a new insight toward understanding parachute behavior, trajectory reconstruction and onboard camera data methods were combined to yield continuous histories of both parachute and test-vehicle angular motions relative to the Earth, free airstream, and each other for the time period from parachute deployment initiation through steady inflation.

INTRODUCTION

A series of four high-altitude flight tests, the Viking Balloon Launched Decelerator Tests (BLDT), were conducted to qualify the Viking parachute system design behind a full-scale simulated Viking entry capsule at Mach numbers and dynamic pressures bracketing those expected on Mars. Test results are presented in two separate reports.

---

*Philip G. Renfroe and Stewart R. LeCroy are associated with LTV Aerospace Corporation, Hampton Technical Center, Hampton, Va.

Parachute test results are discussed in this report, whereas test-vehicle description, test operations, and performance are discussed in reference 1.

The Viking '75 mission is to soft land two scientific payloads on the surface of Mars. Each lander uses a mortar-deployed disk-gap-band parachute in the landing sequence. The parachute is designed to perform its mission throughout the range of atmospheric and entry conditions currently postulated for Mars, which requires parachute deployment to occur at Mach numbers from 2.2 to subsonic speeds and at dynamic pressures from 383 N/m^2 (8 lb/ft^2) to 240 N/m^2 (5 lb/ft^2).

Much Viking parachute system development and qualification activity preceded the BLDT test series. Wind-tunnel tests (ref. 2) showed that the Viking entry capsule, a relatively large bluff body, creates a large turbulent wake, during flight, in which the parachute must operate. A second series of wind-tunnel tests (ref. 3) were conducted to provide information about performance and stability of the parachute while immersed in this wake at several trailing distances behind the Viking spacecraft. In addition, a development series of subsonic low-altitude flight tests, using the selected parachute trailing distance and mortar design but using a small diameter forebody, were conducted to verify the structural design of the parachute. These tests, discussed in reference 4, were conducted at dynamic pressures producing up to 1.5 times the parachute loads expected on Mars. Concurrent with the parachute tests, parachute mortar development and qualification tests were being conducted. (See ref. 5.) The primary purpose of the BLDT series was to insure that parachute inflation, drag, and stability characteristics were satisfactory, with adequate margin, over its postulated operating range. In addition to this report and reference 1, basic parachute test results and a description of the test system are reported in references 6 to 12.

The purpose of this report is twofold: first, to present a summary of parachute performance data from the four flights; second, to present both vehicle and parachute dynamic motion data obtained by using statistical trajectory reconstruction techniques and covering the highly dynamic portion of the test from mortar fire to stable parachute inflation. These dynamic data combined with parachute load histories, trajectory data, and system physical characteristics give a more complete understanding of a parachute system response to its flight environment than previously available. This information is important to a dynamicist interested in checking out his theoretical analysis dealing with any given phase of parachute deployment, inflation, stability, or stability of the system after inflation. An analysis of this type is presented in reference 13.

SYMBOLS

Values are given in both SI and U.S. Customary Units. The measurements and calculations were made in U.S. Customary Units.

a_X, a_Y, a_Z components of test-vehicle acceleration at center of gravity along test vehicle X-, Y-, and Z-axis, respectively, m/sec^2 (ft/sec^2)

C_A axial-force coefficient, based on S_O

$C_{A,p}$ parachute axial-force coefficient, based on S_O

$C_{A,t}$ total axial-force coefficient, based on S_O

C_D drag coefficient, based on S_O

$C_{D,p}$ parachute drag coefficient, based on S_O

D_O nominal parachute diameter, $(4S_O/\pi)^{1/2}$, m   (ft)

g acceleration due to gravity

I_{XX}, I_{YY}, I_{ZZ} moments of inertia about the X-, Y-, and Z-axis, respectively, $kg\text{-}m^2$ $(slug\text{-}ft^2)$

M free-stream Mach number

P_{XY}, P_{XZ}, P_{YZ} products of inertia about the X,Y-, X,Z-, and Y,Z-axis, respectively $kg\text{-}m^2$ $slug\text{-}ft^2)$

p, q, r components of test-vehicle angular velocity about the test vehicle X-, Y-, and Z-axis, respectively, rad/sec

S_O nominal surface area of parachute including vents and gaps, m^2 (ft^2)

t time from test-vehicle release from balloon, sec

X, Y, Z test-vehicle axes system with origin at center of gravity and X-axis parallel to axis of symmetry (see fig. 2)

x, y, z distance along X-, Y-, and Z-axis, respectively, cm   (in.)

x' distance measured from the test-vehicle theoretical apex to the Y,Z plane, cm   (in.)

y'	distance measured from the test vehicle axis of symmetry to the X,Z plane, cm (in.)

| z' | distance measured from the test vehicle axis of symmetry to the X,Y plane, cm (in.) |

α, β test-vehicle angle of attack and angle of sideslip, respectively, deg

γ_p flight-path pitch angle relative to the Earth's surface, deg

γ_y flight-path azimuth angle measured clockwise from true north, deg

$\overline{\Delta R}, \overline{\Delta AZ}, \overline{\Delta EL}$ mean deviation between radar and trajectory reconstruction values of range, m; azimuth, deg; and elevation, deg, respectively

$\overline{\Delta \psi}, \overline{\Delta \theta}, \overline{\Delta \phi}$ mean Euler angle deviation between trajectory reconstruction and camera data, deg

δ_p, ϵ_p angles between vehicle center line and the projections of the parachute center line on the X,Z plane and the X,Y plane, respectively, deg (see fig. 33)

δ_t, ϵ_t angles between vehicle center line and the projections of the parachute load vector on the X,Z plane and the X,Y plane, respectively, deg (see fig. 33)

η test-vehicle total angle of attack, deg

$\sigma_R, \sigma_{AZ}, \sigma_{EL}$ standard deviation from mean deviation between radar and trajectory reconstruction values of range, m; azimuth, deg; and elevation, deg, respectively

$\sigma_\psi, \sigma_\theta, \sigma_\phi$ standard Euler angle deviation from mean Euler angle deviation between trajectory reconstruction and camera values, respectively, deg

ψ, θ, ϕ Euler angles: test-vehicle yaw, pitch, and roll angles, respectively, relative to an Earth-fixed geocentric axes system, deg (round Earth)

TEST ARTICLE

The test article was the Viking parachute system which consists of a single-stage, mortar-deployed Viking disk-gap-band (DGB) parachute having a nominal diameter D_O of 16.15 m (53.0 ft) and a suspension line length of $1.7D_O$. The leading edge of the canopy is 8.5 body diameters aft of the test-vehicle maximum diameter. The parachute has a swivel at the suspension-line confluence point and is attached to the test vehicle by

three bridle legs. The geometric relationship between the deployed parachute and the test vehicle is shown in figure 1. A sketch of the test vehicle showing bridle attachment points (tensiometers) is shown in figure 2. Viking mission constraints required the parachute materials used for BLDT to be scoured to eliminate all oils and cloth "sizing" and the entire system was subjected to a heat sterilization environment of 138° C (280° F) for 200 hours prior to the tests.

Parachute Construction

Nominal constructed parachute geometric characteristics prior to sterilization are listed in table I. Detailed preflight and postflight parachute measurements are included in references 6 to 9.

The parachute had 48 gores and 48 suspension lines. Parachute gore construction and nominal dimensions are shown in figure 3. The parachute was fabricated entirely of Dacron 52 material except for the swivel (steel and aluminum), bridle legs (Dupont fiber B), and the parachute deployment bag (Nomex). The parachute was constructed with the weave of the cloth diagonal to the tapes. The disk cloth was 76.3 g/m^2 (2.25 oz/yd^2) rip-stop weave material and the band cloth was 51.9 g/m^2 (1.53 oz/yd^2) rip-stop weave material. The minimum strength of the radial tapes, circumferential tapes, gap tapes, and suspension lines was 4000 N (900 lb), 8000 N (1800 lb), 4000 N (900 lb), and 3910 N (880 lb), respectively. The bridle legs were four-ply material with a break strength of 60 050 N (13 500 lb) per ply. The swivel was designed for a minimum strength of 118 500 N (26 650 lb) which includes a safety factor of 1.5.

The parachute was packed in a deployment bag to a density of about 640 kg/m^3 (40 lb/ft^3). The nominal total ejected parachute mass was 44 kg (97 lb) and was distributed as shown in table II. The parachute linear mass distribution is presented in figure 4.

Mortar

The mortar had a volume of 0.062 m^3 (2.2 ft^3) and was designed to eject a total mass of 46 kg (102 lb) at muzzle velocities near 34.1 m/sec (112 ft/sec). The mortar was characterized by an erodible orifice designed to maintain constant pressure in the mortar tube during ejection. A detailed discussion of the design, environmental requirements, manufacture, and testing of the Viking mortar system is included in reference 5.

The mortar was located in the aft end of the BLDT vehicle and was offset from but parallel to the vehicle center line. (See fig. 2.) At the time of deployment, the packed parachute was ejected rearward by the mortar and the reaction force was directed through the vehicle center of gravity. A sketch of the parachute installed in the mortar is shown in figure 5. The force from the expanding gasses in the mortar tube was trans-

mitted to the parachute pack by means of a sabot shown in the figure. The sabot was retained shortly after it left the mortar tube to insure that it would not damage the parachute during deployment. The retention method consisted of using flame-resistant straps to connect the sabot internally to the mortar base plate.

TEST METHOD

A combination of balloons and rockets was employed to reach the desired parachute test initiation conditions over the White Sands Missile Range (WSMR). A typical sequence of events for the powered flights (supersonic and transonic parachute tests) is shown in figure 6. For the subsonic parachute test, no rockets were used and the test conditions were attained by allowing the test vehicle to free fall from the balloon.

A detailed discussion of the BLDT test method, from test point selection through launch operations to recovery, is included in references 1 and 10.

TEST OBJECTIVES

BLDT test conditions were selected to bracket the entire range of dynamic pressure and Mach number predicted for parachute operation for the Viking '75 mission. For parachute tests of this nature where aerodynamic loads, opening characteristics, stability, and steady-state drag are desired, Mach number and dynamic pressure have been established to be the most important parameters to be simulated. (See ref. 14.) Since the composition of the Martian atmosphere is such that its speed of sound is much lower than that of the Earth's atmosphere, the velocities of these Earth tests would be appreciably higher than they would be on Mars for equivalent Mach numbers. Test-point dynamic pressure for the BLDT series was adjusted downward to compensate for increased aerodynamic heating and parachute load amplification effects during the Earth tests, and adjusted upward to account for the interplanetary cruise degradation which will occur on the Mars flight. These adjustments were small; for example, for the supersonic tests, the net adjustment in dynamic pressure was 3 percent downward.

Two BLDT tests (designated AV-1 and AV-4) were conducted at supersonic speeds, and one each at transonic (AV-2) and subsonic (AV-3) speeds. Specific test objectives for each flight are as follows:

AV-1: Demonstrate performance and structural integrity at deployment conditions in excess of maximum Mars dynamic pressure and in excess of Mach 2.0.

AV-2: Demonstrate performance at deployment conditions in the transonic region and at a dynamic pressure lower than the lowest expected for Mars.

AV-3: Demonstrate parachute deployment at a velocity less than the minimum expected for Mars.

AV-4: Repeat of supersonic flight (because of parachute damage during AV-1 flight) but targeted to a lower dynamic pressure based on data from Mariner 9 which was available just prior to this flight test.

Combined conditions of Mach number and dynamic pressure occur at unique altitudes for Earth flight tests. For the BLDT test objectives, target parachute deployment altitudes were between 41 and 45 km (134 500 and 147 600 ft) for the supersonic and transonic flights, and near 26.5 km (87 000 ft) for the subsonic test.

TEST VEHICLE

The test vehicle was similar to the Viking '75 entry capsule in size and shape except for the protruding boost rocket motor nozzles and spin motors on the powered vehicles. Figure 1 shows a sketch of the overall parachute test-vehicle arrangement after parachute deployment. Additional details of the test vehicle are shown in figure 2.

The test vehicle had the same masses and centers of gravity as the Viking capsule, including the lateral center-of-gravity displacement, but the moments of inertia differed. Mass characteristics of the four test vehicles are listed in table III. The transonic test vehicle (AV-2) was similar to the supersonic test vehicles (AV-1 and AV-4) except that two rather than four boost motors were required. The subsonic test vehicle (AV-3) had no rocket motors. To simulate the Viking sequence, the forward part (aeroshell) of the test vehicle was separated about 9 seconds after mortar fire. Figure 7 is a photograph of the descending parachute and test vehicle after aeroshell separation.

DATA ACQUISITION SYSTEM

Telemetered data pertinent to parachute performance were from accelerometers measuring linear accelerations along the three test-vehicle axes; rate gyros measuring pitch, yaw, and roll of the test vehicle; and tensiometers measuring axial loads at each of the three bridle attachment points. (See fig. 2.) Onboard cameras, time correlated with the telemetry system and turned on by an onboard timer, were used to photograph the parachute deployment sequence and aeroshell separation. Trajectory information was obtained from WSMR ground-based radar and theodolites, and meteorological data were obtained from radiosondes and rocketsondes.

DATA REDUCTION AND ANALYSIS METHODS

Acceleration data as measured by accelerometers located onboard the test vehicle were converted to linear accelerations at the test-vehicle center of gravity by making

corrections for angular rates and angular accelerations. Since it was known that directly after release from the balloon the test vehicle was in a true "zero g" condition, all accelerometer data were adjusted to read zero at this time and this bias value was subtracted from all subsequent data. Similarly, biases were removed from angular rate data, since load bar cameras verified that a zero angular rate condition existed just prior to drop. These conditions were true in flight calibration points and improved the accuracy of the measurements of these quantities. (See ref. 1.)

Rocketsonde pressure measurements were adjusted to the level of the data point measured by the precision pressure gages carried on the balloon load bar. These precision gages not only were more accurate above 30 km (100 000 ft) but also were positioned much closer in time and location to the parachute test region than either rocketsonde or radiosonde. The test-vehicle velocity as measured from radar was converted to true airspeed by using the wind values measured at the proper altitude by rocketsonde or radiosonde.

VEHICLE DYNAMICS

Time histories of vehicle Euler angles (ψ, θ, and ϕ) were obtained from flight-test data by using the statistical trajectory estimation program (STEP, ref. 15). The data period evaluated extended continuously from the initiation of parachute deployment (mortar firing) to about 30 seconds thereafter. This covered the period of highly oscillatory parachute motions from opening until subsonic speeds were reached. Relatively stable parachute conditions and vehicle angular motions were reached by this time.

Briefly, STEP is a digital computer method that uniquely applies statistical estimation theory to fit equations of motion to atmospheric trajectory measurement data. The vehicle is treated as a rigid body responding to forces as characterized by onboard accelerometer, gyro, and radar tracking data. Vehicle Euler angle data are obtained from the STEP analysis and are combined with wind speed and direction data to obtain vehicle angle of attack α, angle of sideslip β, and total angle of attack η.

STEP integrates the accelerometer and gyro data to produce a minimum variance solution to radar position data and solve for a related set of (theoretical) initial conditions (such as vehicle attitude, position, flight-path angle, and velocity). These theoretical initial conditions may then be compared with the actual initial conditions that were input to the program. STEP permits estimates of biases and scale factors on the accelerometer and gyro data. For this application, discussed more in detail in reference 16, the biases and scale factors used were the ones which gave the best correlation between Euler angles from STEP and those from independent camera techniques (to be discussed). The actual initial conditions, biases, and scale factors used for each flight are shown in table IV. The initial conditions shown in the table were obtained from a similar STEP

8

analysis of the less dynamic part of the flight, just prior to mortar fire. (See ref. 1.) Verification of initial conditions was obtained from radar and camera data which were available during this part of the flight. The data, altered by the applied biases and scale factors, are within the accuracy limitations of the measured data.

To check the validity of the STEP results and to serve as a guide for the STEP analysis, test-vehicle Euler angles were also obtained for brief portions of the flight by means of two independent methods using camera film. In the first method, described in reference 17, data were obtained whenever the trajectory was such that identifiable Earth landmarks were in view of either the forward- or aft-facing cameras. Using this method requires a minimum of two landmarks, the Earth-related coordinates of the vehicle, the orientation of the camera with respect to the vehicle, and the focal length and distortion characteristics of the camera lens. For these flights, atmospheric refraction corrections were determined to be negligible and were, therefore, not included.

In the second method, independent of the first method and used only for the AV-4 flight, no landmarks were used and instead data were obtained by measuring the location of the separated aeroshell and the horizon with respect to the forward camera onboard the vehicle. Also required were the coordinates of the vehicle and aeroshell from radar and cinetheodolite tracking data. This second camera method was used to obtain data when no landmarks were visible.

The STEP Euler angles are assumed to be valid throughout the data period if the STEP produced histories of velocity, altitude, flight azimuth angle, and flight-path angle closely match radar data, and if the STEP Euler angles compare favorably with camera data.

PARACHUTE MOTIONS AND LOAD PULL-OFF ANGLES

The relative motions between the parachute and vehicle were obtained by measuring the position of the parachute vent in the photographs from the rearward-viewing cameras. Since the angles of the test vehicle to the relative wind had been determined as previously discussed, a time history of the angle between the parachute and relative wind was readily obtained.

The total parachute load pull-off angle and direction (to be discussed) were determined by using the tensiometer data and considering the elasticity of the bridle.

ACCURACY

The estimated accuracies of the data from the onboard instrumentation pertaining to test-vehicle performance and also from ground-based radar, optical, and meteorological equipment are discussed in reference 1. Total load data from flights AV-1 and

AV-4 are estimated to be accurate within ±2670 N (600 lb) when the load exceeds 16 010 N (3600 lb) and ±1110 N (250 lb) when the load is below 16 010 N (3600 lb). This load accuracy was determined from the longitudinal accelerometers and the load value of 16 010 N (3600 lb) represents the maximum value which could be determined by using the low-range longitudinal accelerometer. Loads in excess of this value had to be determined by using the high-range longitudinal accelerometer. Parachute load values as measured at the bridle attachment points were determined from tensiometers and are estimated to be within ±1600 N (360 lb) per bridle leg. Only one range tensiometer was used.

Corresponding accelerometer load accuracies for AV-2 and AV-3 are 1330 N (300 lb) above 16 010 N (3600 lb) and ±800 N (180 lb) below 16 010 N (3600 lb). Tensiometer loads are estimated to be within 1070 N (240 lb) per bridle leg.

Camera-produced Euler angles are estimated to be within ±2° for ψ and θ and within ±4° for ϕ. The accuracy of the Euler angle data obtained from the STEP analysis is discussed later in this report.

RESULTS AND DISCUSSION

The parachutes all successfully deployed and inflated in the wake of the simulated Viking forebody in the three Mach number regimes. The AV-2, AV-3, and AV-4 flights bracket the range currently postulated for the Viking '75 mission (ref. 1) and no significant parachute damage was sustained. During the AV-1 deployment process, two canopy gores were torn. These tears are attributed to initial damage possibly occurring during the bag stripping process being propagated by localized high pressure during an unsymmetrical canopy inflation. (See ref. 10.) The localized high pressure was augmented by a parachute deployment at a dynamic pressure approximately 20 percent above the maximum anticipated value which was already at 130 percent of design. The high dynamic pressure at deployment resulted from the test vehicle flying a lower than nominal trajectory which, in turn, was caused by damage to the test-vehicle support structure at balloon launch. Analyses show that the AV-1 parachute performance was not affected by the canopy damage and the parachute did produce sufficient drag and stability for a successful mission to Mars. (See refs. 6 and 10.) Detailed discussions of parachute postflight condition for the various flights are included in references 6 to 9.

During balloon ascent, AV-3 passed through a severe rainstorm which resulted in unknown quantities of water and/or ice remaining in the payload and aeroshell during the parachute test. Consequently, the mass properties of the test vehicle are not accurately known. Also it was not possible to determine landmarks to reduce any Euler angle data from the onboard cameras for AV-3. Data on the deployment characteristics of the

10

parachute in the subsonic speed range, which was the main objective of the AV-3 test, was not impaired by these anomalies. Parachute drag and stability characteristics in the subsonic region are available from the AV-2 and AV-4 flights after deployment.

Atmospheric pressure, density, temperature, and speed of sound obtained within about 1 hour after the test and time histories of the altitude, velocity (wind corrected), Mach number, and dynamic pressure for each of the flights are presented in reference 1 along with test-vehicle yaw, pitch, and roll rates and linear accelerations about the body axes. Table V lists Mach number, dynamic pressure, and time from drop for the events of mortar fire, line stretch, first peak load (to be discussed), and aeroshell separation.

Although the analysis was performed independently and, at times, using different data reduction techniques, the test data presented in this report compare closely with those presented earlier for the same flight tests reported in references 6 to 9. The choice and application of meteorological data, as discussed in reference 1, account for the differences between the two sets of data. The most significant differences are in dynamic pressures for the AV-1 and AV-4 flights. For example, at mortar fire, dynamic pressures listed in table V for these two flights are about 4 percent lower than in the reference reports.

<center>Parachute Temperatures</center>

Temperature measurements were made on the outside of the mortar canister on all flights and averaged as follows at the time of drop from the balloon:

Flight	Temperature	
	°C	°F
AV-1	9.4	49
AV-2	7.8	46
AV-3	-3.9	25
AV-4	7.8	46

That part of the parachute in contact with the mortar tube was probably close to these temperatures. Because of the relatively low thermal conductivity of the parachute pack, the center of the pack would be much closer to the ambient temperature before the flight. The center of the parachute pack was estimated to be about 17° C (64° F) for AV-1, AV-2, and AV-4 and 10° C (50° F) for AV-3.

<center>Parachute Loads</center>

The variation of total parachute load for each of the four tests up to 16 seconds after mortar fire is shown in figures 8 to 11. This total load is obtained by summing the

data from the three tensiometers located at the bridle attachment points. An analysis accounting for stretch of the bridle showed that it was so inelastic that the load time histories in figures 8 to 11 also represent the time histories of the total load vector at the bridle confluence point. Data from the individual tensiometers are presented in references 6 to 9 for each of the flights. The times of first peak load are listed in table V. The first peak load is not necessarily the maximum load. It was not the maximum for the AV-1 (fig. 8) and AV-4 (fig. 11) flights, but definitely was the maximum for the AV-2 flight (fig. 9). The dynamic forces of the canopy unfurling are of a very random nature and are influenced by many factors some of which are interrelated. Among these factors are parachute configuration, canopy folding and packing methods, suspension line elasticity and damping, the speed at which the bag is stripped off the canopy, the angle of the bag to the airstream as the canopy emerges, the position of the bag in the wake created by the payload, and waves induced in the suspension lines as they extend. Some of these factors are influenced by the angle-of-attack time history of the forebody just prior to and during the parachute deployment. Further analyses are presented in reference 10. A comparison of an advanced parachute deployment dynamics model with AV-4 results is made in reference 18.

Parachute Drag and Area Ratio

Axial-force coefficient data based on nominal parachute area were obtained from both longitudinal accelerometer and tensiometer data. As will be shown in later sections, the total angles of attack for $M = 1$ and above are generally under 10°; consequently, the difference between drag and axial force is less than 2 percent. At subsonic speeds total angles of attack reach 20° and result in differences between drag and axial force up to approximately 6 percent.

The axial-force coefficient data as obtained from raw accelerometer data for AV-1, AV-2, and AV-4 for the total system (parachute with test vehicle) are shown in figures 12 to 14. Also parachute-alone axial-force coefficient as derived from both accelerometer and tensiometer data are presented as a function of Mach number in figures 15 to 20 for the same flights. Both the amplitude and frequency of the data derived from accelerometers agree very well with the data obtained from tensiometers for each flight considered individually. In addition, after a short period of initial inflation oscillations, the average value of axial-force coefficient shows good agreement among flights throughout the Mach number range.

Comparison of figure 16 with figure 19 shows that the tears in the canopy of AV-1 caused little change in drag coefficient. The $C_{D,p}$ in all cases is based on the nominal surface area of the parachute S_o. The actual loss of cloth for the AV-1 parachute was

slightly over 1 percent. The primary effect of the tears was to increase the geometric porosity of the parachute and make it unsymmetrical.

The axial-force coefficient data for AV-2 and AV-4 show the characteristic dip in the transonic region which is also shown in wind-tunnel test data (ref. 3) and is attributed to an interaction between the large forebody wake and the parachute canopy in the transonic region. It is not, however, noticeable in the data from AV-1. No similar axial-force coefficient dip was determined from flight tests at similar conditions of similar parachutes trailing behind relatively small slender forebodies. (See ref. 19.) No adjustment was made to axial-force-coefficient reference area for any of the flights because of canopy oscillations or for AV-1 because of canopy damage. The AV-3 data are not included because of the uncertainty of vehicle weight due to the previously mentioned unknown amounts of ice present during the tests.

Large oscillatory variations occurred in all the axial-force coefficient data until the time that steady parachute inflation was reached. During this interval motion pictures from the onboard cameras show breathing and/or flapping motions of various parts of the parachute, as well as a displacement of the complete parachute canopy about the suspension-line confluence point. For several seconds after parachute opening, the flapping motion of the outer edge of the canopy was sufficiently severe that many suspension lines became intermittently slack. The frontal area of the parachute canopy, as observed in onboard motion-picture film, was measured and correlated with flight time from telemetered data. A time history of the parachute area ratio based on the frontal area at the time of first full inflation is presented for each of the four tests in figures 21 to 24. In the determination of values for area ratio, all the area inside the external boundary of the parachute frontal area is included. For AV-1 the area of the large holes in the parachute canopy was not subtracted. This additional area explains the much higher level of the area ratio (about 1.05) for AV-1 than for AV-4 (about 0.8) after the large initial amplitude oscillations had damped.

In many cases the correspondence between changes in area ratio and in parachute load or axial-force coefficient is readily apparent. For example, partial collapse of the AV-4 parachute (fig. 24) near 3.6 seconds after mortar fire is accompanied by a significant decrease in parachute load (fig. 11) and hence in parachute axial-force coefficient at $M = 1.62$ as indicated in figure 19. This reduction in area ratio resulted from a folding under of a large section of the canopy causing the frontal area to be distorted from its normal circular shape. The variations in area ratio are much less than the corresponding variation in load. For AV-4, a 40-percent reduction in area ratio occurred about the same time (3.6 seconds after mortar fire) as an 87-percent reduction in load. These reductions result, to some extent, from a change in the drag coefficient of the distorted canopy but are also influenced by the elasticity of the system.

Rapidly oscillating force coefficient data as presented in figures 12 to 20 are typical of parachute tests of this nature. (See, for example, ref. 19.) However, not only are they extremely cumbersome to use for future studies or applications involving parachute performance, but these large force variations would not necessarily occur at the same time and/or Mach number for similar tests. Instead, a fairing representing the average force during these oscillatory periods is much more useful for assessing parachute performance. The variation of C_D as a function of Mach number for the parachute, presented in figure 25, was obtained by averaging the axial accelerometer data for AV-2 and AV-4 over velocity intervals of 30.5 m/sec (100 ft/sec) or less, and also from reconstructing the trajectory as determined from radar data over similar intervals. The average C_D variation is assumed to be equal to the average C_A variation. The heavy solid line is an average fairing of these smoothed data. Although no reason is known for the rise in the level of drag coefficients below $M = 0.1$, the increased level is in agreement with the C_D values determined from the low-speed drop tests presented in reference 4.

As shown in figure 26, between $0.1 \leq M \leq 0.7$, these data compare very well (within 3 percent) with the wind-tunnel results of reference 2. From $0.7 < M \leq 1.0$, the wind-tunnel data decrease rapidly to about 65 percent of the low-speed value and is as much as 35 percent lower than the BLDT results. Above Mach 1, the wind-tunnel data remain 20 to 25 percent lower than the BLDT results. The C_D data from BLDT are measured in free flight for the actual Viking parachute in the wake of a geometrically simulated Viking entry capsule and at the expected range of Mach number and dynamic pressure. The time history of axial accelerations following inflation should be similar to Viking because of the similar masses and test environments. Because of the excellent agreement between the accelerometer, tensiometer, and trajectory reconstruction methods of deriving drag, it is believed that the accuracy for the BLDT C_D values, shown in figures 25 and 26, are within ± 0.03. The C_D values match or exceed the nominal parachute C_D required for the Viking '75 mission as identified in reference 10.

Load Vector Angles

It would be most desirable if the parachute load applied to the test vehicle was steady and applied entirely in the direction of the relative wind. The load would then be confined to slowing down the system without creating any side motion or inducing oscillations. The test vehicle, however, was a large blunt body creating considerable wake which impinged upon the opened parachute. The canopy was very pliant and the suspension lines were elastic; therefore, the parachute load, particularly at supersonic speeds, varied considerably in magnitude and direction.

14

Separate tensiometers were installed at each of the three bridle attachment points and were designed so that each tensiometer read only the axial load component. Since the bridle arrangement was symmetrical, if the readings of all three tensiometers were equal, the parachute load vector was parallel to the vehicle X-axis. If the readings were not equal, it was possible to compute the angle of the load vector to the X-axis. This load vector angle is important from the standpoint of bridle design. The angle is broken down into two components which are called pull-off angle and pull-off direction as shown in figure 27. As noted in figure 2, the test-vehicle center of gravity is displaced 3.58 cm (1.41 in.) above the center line so that the bridle confluence point (fig. 3) does not lie on an extension of the vehicle X-axis. If it were assumed that the center of gravity must have been directly below the center of drag force of the parachute in steady-state vertical descent, then the axis of the vehicle was tipped about 0.07^O off the vertical and the bridle loadings were, therefore, not exactly equal. The bridle was made of material which was capable of stretching. If the pull-off angle was other than zero, the loads in the bridle legs were unequal and each leg stretched a different amount. This amount of unequal stretch further affected the load-vector orientation. A computer program was devised by using an iteration procedure to calculate a time history of the pull-off load, pull-off angle, and pull-off direction which must have existed to produce the measured tensiometer readings. The computer program allowed for the bridles to be elastic (the actual case) or inelastic. Bridle elongation as a function of load per bridle leg is shown in figure 28. No significant difference in the magnitude of parachute load or pull-off direction was noted whether or not the elasticity was considered. Likewise, variation of total load pull-off angle with time from mortar fire is shown in figures 29 to 32. Differences of 0.5^O in pull-off angle between the elastic and nonelastic bridle cases occurred at times for AV-1 and AV-4, as shown in figures 29 and 32, respectively. For the smaller loads experienced by flights AV-2 and AV-3, the differences in pull-off angle were less significant, as shown in figures 30 and 31, respectively. The results show that for the very stiff bridle used in these tests, the bridle elasticity had a small effect on the parachute pull-off angle, for high load conditions only, and no noticeable effect on parachute load or pull-off direction regardless of load.

Parachute Motion

The inflated parachute was observed by time-correlated onboard motion-picture cameras. From the film, the angular displacement between the parachute axis and the test-vehicle longitudinal axis was determined in both the vehicle X,Y plane ϵ_p and X,Z plane δ_p. These angles are defined in figure 33. The parachute axis was considered to be a line connecting the center of the vent with the confluence point of the suspension lines. Inspection of onboard camera film revealed essentially no motion of the

bridle confluence point after the parachute had extended. Histories of ϵ_p and δ_p as well as ϵ_t and δ_t are plotted in figures 34 and 35, respectively, for AV-2 and in figures 36 and 37, respectively, for AV-4. Because of the canopy damage sustained during deployment, no values were determined for flight AV-1. Because of poor film quality, no values were determined for flight AV-3.

The load vector pull-off angles were similarly projected onto the test vehicle X,Y plane ϵ_t and X,Z plane δ_t and are also plotted in figures 34 to 37. In a steady-state condition, the load vector should essentially coincide with the parachute axis. Comparison between the position of the load vector and the parachute axis in these figures shows the oscillations to be in phase, but with the load angle plots to be much more ragged. This raggedness is undoubtedly caused by the breathing and flapping motions of the parachute canopy superimposed upon the motions of the entire parachute and test vehicle.

Vehicle Dynamics

The most severe load variations on each test vehicle occurred during the period from the beginning of the parachute inflation process until stable inflation. These loads are direct functions of the parachute system loads and the transmittability of the loads to the vehicle. The reaction of the vehicle to the parachute system loads can partially be assessed by analyzing the vehicle angular rates and rate variations as discussed in references 6 to 11. However, of additional interest to the parachute deployment and inflation modeler or the vehicle dynamicist are the actual variations in vehicle attitudes and angles of attack associated with a defined set of parachute system loads. Integration of the attitude rates and accelerations will theoretically produce attitude angles if initial conditions are known. Historically, however, initial condition inaccuracies and inaccuracies due to integrating over long data periods have often resulted in questionable output data. As previously discussed, STEP utilizes gyro and accelerometer integration but minimizes inaccuracies by the utilization of biases and scale factors and by employing statistical theory to produce a minimum variance solution.

The STEP derived vehicle Euler angles (ψ, θ, and ϕ) and flight-path angles (γ_y and γ_p) from mortar fire through stable parachute inflation are shown for flights AV-1, AV-2, and AV-4 in figures 38 to 46. Included for comparison are flight-path angles from radar data and Euler angles determined independently from the previously discussed vehicle camera and Earth landmark technique. The camera Euler angles cover only those time periods where identifiable Earth landmarks were in view of the camera. For the AV-4 flight, Euler angles from the other camera technique (vehicle camera and separating aeroshell) are also included in figures 44 to 46 for the short period of time ($51 \leq t \leq 57$ seconds) in which the separating aeroshell was in view of the forward-facing vehicle camera. As previously mentioned, the camera Euler angle data were used essen-

tially as targets for STEP. The assumption was that STEP results were valid if STEP could be manipulated to produce Euler angles comparable with the limited camera data without compromising either the input values or other trajectory parameters. The AV-3 flight trajectory was such that no landmarks were identified from onboard camera era data and, in addition, the separating aeroshell was not tracked. Consequently, no Euler angle data are included for AV-3.

The increasing variation with time between flight-path azimuth angle γ_y and the mean value of test-vehicle yaw angle ψ evident for AV-1 (fig. 38) and AV-4 (fig. 44) is attributed to relative wind direction and magnitude.

The STEP flight-path azimuth and flight-path pitch angles are in good agreement with radar results as can be seen in the figures. For any flight, the maximum variation in both flight-path azimuth and flight-path pitch angles is 1° which is within the accuracy of the input data. The STEP trajectory differed from the radar trajectory by the mean deviations ($\overline{\Delta R}$, $\overline{\Delta AZ}$, and $\overline{\Delta EL}$) and standard deviations from the mean deviations (σ_R, σ_{AZ}, and σ_{EL}) shown in the following table:

Flight	Range, m		Azimuth, deg		Elevation, deg	
	$\overline{\Delta R}$	σ_R	$\overline{\Delta AZ}$	σ_{AZ}	$\overline{\Delta EL}$	σ_{EL}
AV-1	5.70	7.38	0.006	0.005	0.013	0.008
AV-2	6.41	7.00	.026	.028	.007	.010
AV-4	3.10	2.76	.021	.015	.007	.005

These differences are within the accuracies of the radar data. However, they might have been smaller if STEP inputs had been biased with the sole intent of minimizing the differences between the STEP and radar trajectories without regard to Euler angle matchup.

Euler angle comparison between STEP and camera data is also very good. The data trends and oscillation frequencies shown by each method are in excellent agreement when the system dynamics involved are considered. Although disagreement is small, Euler angle amplitude agreement tended to decrease with flight time. This decrease in agreement may be attributed to inherent inaccuracy build-up with time (although minimized by STEP) due to accelerometer and rate gyro integration. The mean deviation between STEP and camera data ($\overline{\Delta\psi}$, $\overline{\Delta\theta}$, and $\overline{\Delta\phi}$) along with the standard deviation from the mean deviation (σ_ψ, σ_θ, and σ_ϕ) are shown in the following table for each parameter:

Flight	$\overline{\Delta\psi}$, deg	σ_ψ, deg	$\overline{\Delta\theta}$, deg	σ_θ, deg	$\overline{\Delta\phi}$, deg	σ_ϕ, deg
AV-1	2.12	1.77	1.60	1.56	4.92	2.6
AV-2	2.29	1.75	.93	.67	3.74	4.71
[1]AV-4	2.17	1.47	1.66	1.06	5.56	2.37
[2]AV-4	2.36	1.15	1.67	.98	4.68	1.10
[3]AV-4	2.02	1.75	2.47	.87	7.61	3.15

[1]Includes data from both camera methods.

[2]Camera data from separating aeroshell method only ($51.0 \leq t \leq 57.5$).

[3]Camera data from Earth landmark only ($68.5 \leq t \leq 75.0$).

As previously discussed, camera data inaccuracy is estimated to be within $\pm 2^\circ$ for ψ and θ and within $\pm 4^\circ$ for ϕ.

The STEP Euler angle data and wind-corrected velocity vector data were used to obtain time histories of β, α, and η for AV-1, AV-2, and AV-4 in figures 47 to 55. The total vehicle angle-of-attack data, shown in figures 49, 52, and 55, exhibited a similar trend for all three flights in that the average value remained within a span of 5° to 8° for the time period near mortar fire and increased to a range of 16° to 20° near the end of the data period. This effect is generally attributed to the rapidly decreasing flight-path angles after mortar fire (figs. 39, 42, and 45), which occurred in all flights, coupled with the slow response of the parachute and test-vehicle system to the relative airstream.

Test-vehicle total angle of attack η at the events of mortar fire, line stretch, and first peak load are listed in the following table:

Event	Value for η, deg, for flight		
	AV-1	AV-2	AV-4
Mortar fire	12.6	8.1	2.1
Line stretch	2.4	3.6	9.5
First peak load	10.8	6.6	1.9

Parachute Angle of Attack

In any analysis of the dynamics of the parachute-vehicle system, the parachute angle of attack is of interest because the parachute is by far the greatest contributor to both total load and moments. Since the history of test-vehicle angle of attack and sideslip was available as a result of the STEP data and the angle between the test vehicle and

the parachute had been obtained from the camera data, the angle between the parachute and the free airstream could be determined. For AV-2, the test-vehicle β and α data (figs. 50 and 51, respectively) were combined with the parachute δ_p and ϵ_p data (figs. 34 and 35, respectively) to give the parachute angles of sideslip and angles of attack shown in figures 56 and 57, with any parachute roll relative to the test vehicle being ignored. In a similar manner these angles were determined for AV-4 and are presented in figures 58 and 59.

From the components, the parachute total angle of attack was determined for AV-2 and AV-4 as shown in figures 60 and 61, respectively. For AV-2, some small oscillation in parachute total angle of attack occurred about a trim value near 5° down to a Mach number near 0.9 followed by an increase in both the amplitude and trim value. The parachute collapse (fig. 22) observed 3 seconds after mortar fire near $M = 1.0$ could have caused the abrupt reduction in total angle of attack between $M = 1.0$ and $M = 0.85$ and induced the high-amplitude oscillation which followed. However, during the large-amplitude parachute oscillations observed in figure 60 after 43 seconds, the area ratio (fig. 22) is relatively constant. The parachute total angle of attack for AV-4 (fig. 61) shows much less motion than that for AV-2. However, all the AV-4 parachute angle-of-attack data are above $M = 1$ and have about the same average as the AV-2 data above $M = 0.9$. The AV-4 area ratio variation shown in figure 24 shows a fair amount of canopy distortion throughout this entire data period.

Canopy Stability During Inflation

In viewing the motion pictures of the AV-2 vehicle during flight, it was noted that 3 seconds after mortar fire, there was a large collapse and reinflation of the parachute which occurred after the parachute had steadied down following its opening shock load. This collapse is also very noticeable in the area ratio (fig. 22) and the total load plot of figure 9. The pictures show that this reduction of parachute area occurred with practically no canopy distortion, but instead the circular shape was maintained. This parachute collapse is also reflected in the plot of axial-force coefficient (fig. 13 for $M = 1$ to $M = 0.94$) and probably is a contributing cause of the dip in the C_D curve around $M = 1$ observed in figure 25. It should be noted, however, that this is the same Mach number range where a large dip occurred in the C_D data from wind-tunnel tests. (See fig. 26.) The total angle of attack of the test vehicle at this time is oscillating between 2^O and 10° and the total angle of the parachute to the relative wind averages about 5°. Throughout this time period, motion pictures show considerable bowing of many of the suspension lines which indicated that the load distribution throughout the parachute canopy is very nonuniform.

The total load plot for AV-4 (fig. 11) also reflects a large collapse and reinflation of the canopy at about 3.5 seconds after mortar fire by indicating a rapid change in loads. It is likewise very noticeable in the plot of area ratio. (See fig. 24.) Unlike the AV-2 canopy, however, motion pictures show that the AV-4 canopy was considerably distorted. The band and edge of the canopy are folded under on opposing sides and, as in AV-2, many of the suspension lines were bowed or even slack. The test-vehicle total angle of attack at this time was oscillating between about 10° and 2° with the parachute total angle of attack oscillating between approximately 6° and 3°. The corresponding Mach number is near $M = 1.6$. In this case, $M = 1$ does not occur until well after aeroshell separation.

The AV-1 canopy does not exhibit a large collapse of this nature as may be observed in the AV-1 total load plot (fig. 8) and area ratio plot (fig. 21), although it does show several smaller variations in the area ratio plot. Whether this effect can be attributed to the additional geometric porosity resulting from the tears in the canopy or whether the dynamics of the various factors were such that they did not happen to reinforce each other at any time to cause a collapse cannot be ascertained with a single test.

For AV-3 after the few opening oscillations, no large area ratio or load oscillations occur as shown in figures 23 and 10, respectively.

In previous tests of disk-gap-band parachutes at high Mach numbers (refs. 20 and 21), the canopy oscillations were considerably larger above a Mach number of 1.5 than below $M = 1.5$. These tests were all behind a small slender body with different parachute elastic characteristics. In the BLDT tests, which took place behind a large blunt body, the AV-1 and AV-4 area ratio plots (figs. 21 and 24, respectively) show a similar change in canopy stability, which is also reflected in the load plots (figs. 8 and 11) for the same two flights. For AV-1, the increased stability appears near $M = 1.7$. For AV-4, a decrease in canopy oscillation magnitude occurred near $M = 1.8$ followed by a parachute collapse and increased oscillation amplitude which did not damp before $M = 1.5$.

Aeroshell Separation

As previously discussed, the aeroshell, or forward portion of the test vehicle, was separated from the BLDT system to simulate the event for the Viking mission. Conditions at aeroshell separation from each of the BLDT tests are listed in table V. Aeroshell separation constraints for the Viking mission and the applicability of the BLDT results to these constraints are discussed in reference 10 with the conclusion that within BLDT data limits, aeroshell separation poses no significant problems to the Viking mission.

There had been some concern as to whether the wake from the separating aeroshell would significantly degrade parachute performance. The event of aeroshell separation is indicated in the plots of axial force against Mach number. (See figs. 12 to 20.) For AV-2 and AV-4, a definite decrease in axial-force coefficient occurs immediately after aeroshell separation but lasts through a Mach number change equivalent to only 1 second of flight time and has no significant effect on parachute drag performance for the Viking mission. During this time period, the separating aeroshell was within 3 aeroshell diameters or approximately 9 m (30 ft) from the remaining section of the test vehicle. No definite decrease in axial-force coefficient which can be attributed to aeroshell separation was indicated by the AV-1 results (figs. 15 and 16), possibly because of the relative orientation and/or position histories of the aeroshell and parachute.

Aeroshell separation also has little significant effect on the vehicle total-angle-of-attack histories for the flights of the vehicles AV-1, AV-2, and AV-4 shown in figures 49, 52, and 55, respectively. For the AV-1 and AV-4 transonic separations, a 3° decrease in the average value of the oscillation beginning about 1 second after aeroshell separation is evident. No similar change is noted for the AV-2 subsonic separation.

CONCLUSIONS

Four flight qualification tests of the Viking 16.15-meter (53-ft) nominal-diameter disk-gap-band parachute were conducted at Mach number and dynamic pressure conditions which bracketed the range postulated for the Viking '75 mission to Mars. Parachutes were deployed at supersonic, transonic, and subsonic speeds behind a simulated Viking entry capsule. From these tests, the following conclusions may be made:

1. The Viking 16.15-meter (53-ft) nominal-diameter disk-gap-band (DGB) parachute was successfully deployed and inflated in the wake of a large-scale forebody in three Mach number regimes and met all the criteria for flight qualification for the Viking mission.

2. Parachute drag and stability are in good agreement for all tests after initial deployment and inflation oscillations.

3. Parachute drag performance or stability was not degraded during the AV-1 test despite two gores being torn during deployment.

4. Parachute axial-force coefficients exhibit a dip (except for the AV-1 torn canopy test) near Mach 1 as indicated in wind-tunnel tests and are attributed to wake effects from the large forebody.

5. Parachute drag from the BLDT flight results compares well with subsonic wind-tunnel data and exceeds the transonic and supersonic wind-tunnel data.

6. Fluctuations in parachute loads were much larger than corresponding fluctuations in projected parachute area ratio.

7. Consideration of bridle elasticity in the reduction of parachute load vector data showed a difference near $1/2^\circ$ in pull-off angle, but had no effect on parachute load or pull-off direction.

8. The aeroshell separation sequence occurred successfully during all tests and the wake had no significant effect on parachute performance or stability.

9. Trajectory reconstruction and onboard camera methods were combined to yield continuous histories of both parachute and test vehicle angular motions relative to the Earth, free airstream, and each other for the time period from mortar fire through steady parachute inflation. These angular motions along with the parachute load histories, trajectory, and system characteristics combine to give a complete picture of parachute system response and a better understanding of deployment dynamics.

Langley Research Center,
National Aeronautics and Space Administration,
Hampton, Va., July 30, 1974.

REFERENCES

1. Lundstrom, Reginald R.; Raper, James L.; Bendura, Richard J.; and Shields, E. William: Flight Tests of Viking Parachute System in Three Mach Number Regimes. I – Vehicle Description, Test Operations, and Performance. NASA TN D-7692, 1974.

2. Campbell, James F.; and Brown, Clarence A., Jr.: Evaluation of Experimental Flow Properties in the Wake of a Viking '75 Entry Vehicle. AIAA Paper No. 73-475, May 1973.

3. Steinberg, Sy; Siemers, Paul M., III; and Slayman, Robert G.: Development of the Viking Parachute Configuration by Wind Tunnel Investigation. AIAA Paper No. 73-454, May 1973.

4. Murrow, H. N.; Henke, D. W.; and Eckstrom, C. V.: Development Flight Tests of the Viking Decelerator System. AIAA Paper No. 73-455, May 1973.

5. Brecht, John P.; Pleasants, James E.; and Mehring, Richard D.: The Viking Mortar: Design, Development, and Flight Qualification. AIAA Paper No. 73-458, May 1973.

6. Dickinson, D.; Schlemmer, J.; Hicks, F.; Michel, F.; and Moog, R. D.: Balloon Launched Decelerator Test Program – Post-Flight Test Report – BLDT Vehicle AV-1. TR 3720289 (Contract NAS 1-9000), Martin-Marietta Corp., Sept. 1972. (Available as NASA CR-112176.)

7. Dickinson, D.; Schlemmer, J.; Hicks, F.; Michel, F.; and Moog, R. D.: Balloon Launched Decelerator Test Program – Post-Flight Test Report – BLDT Vehicle AV-2. TR-3720291 (Contract NAS 1-9000), Martin-Marietta Corp., Dec. 1972. (Available as NASA CR-112177.)

8. Dickinson, D.; Schlemmer, J.; Hicks, F.; Michel, F.; and Moog, R. D.: Balloon Launched Decelerator Test Program – Post-Flight Test Report – BLDT Vehicle AV-3. TR-3720293 (Contract NAS 1-9000), Martin-Marietta Corp., Jan. 1973. (Available as NASA CR-112178.)

9. Dickinson, D.; Schlemmer, J.; Hicks, F.; Michel, F.; and Moog, R. D.: Balloon Launched Decelerator Test Program – Post-Flight Test Report – BLDT Vehicle AV-4. TR-3720295 (Contract NAS 1-9000), Martin Marietta Corp., Oct. 20, 1972. (Available as NASA CR-112179.)

10. Moog, R. D.; and Michel, F. C.: Balloon Launched Viking Decelerator Test Program Summary Report. TR-3720359, Martin Marietta Corp., Mar. 1973. (Available as NASA CR-112288.)

11. Moog, R. D.; Bendura, R. J.; Timmons, J. D.; and Lau, R. A.: Qualification Flight Tests of the Viking Decelerator System. AIAA Paper No. 73-457, May 1973.

12. Raper, James L.; Michel, Frederick C.; and Lundstrom, Reginald R.: The Viking Parachute Qualification Test Technique. AIAA Paper No. 73-456, May 1973.

13. Talay, Theodore A.: Parachute-Deployment-Parameter Identification Based on an Analytical Simulation of Viking BLDT AV-4. NASA TN D-7678, 1974.

14. Gillis, Clarence L.; and Bendura, Richard J.: Full-Scale Simulation of Parachute Deployment Environment in the Atmosphere of Mars. 14th Annual Technical Meeting Proceedings, Inst. Environ. Sci., 1968, pp. 469-475.

15. Wagner, William E.; and Serold, Arno C.: Formulation on Statistical Trajectory Estimation Programs. NASA CR-1482, 1970.

16. Shields, E. William: Statistical Trajectory Estimation (STEP) Implementation for BLDT Post Flight Trajectory Simulation. NASA CR-132427, 1974.

17. Bendura, Richard J.; and Renfroe, Philip G.: A Data Reduction Technique and Associated Computer Program for Obtaining Vehicle Attitudes With a Single Onboard Camera. NASA TM X-3050, 1974.

18. Whitlock, Charles H.; Poole, Lamont R.; and Talay, Theodore A.: Postflight Simulation of Parachute Deployment Dynamics of Viking Qualification Flight Test. NASA TN D-7415, 1973.

19. Whitlock, Charles H.; and Bendura, Richard J.: Inflation and Performance of Three Parachute Configurations From Supersonic Flight Tests in a Low-Density Environment. NASA TN D-5296, 1969.

20. Preisser, John S.; and Eckstrom, Clinton V.: Flight Test of a 40-Foot-Nominal-Diameter Disk-Gap-Band Parachute Deployed at a Mach Number of 1.91 and a Dynamic Pressure of 11.6 Pounds Per Square Foot. NASA TM X-1575, 1968.

21. Eckstrom, Clinton V.; and Preisser, John S.: Flight Test of a 40-Foot-Nominal-Diameter Disk-Gap-Band Parachute Deployed at a Mach Number of 2.72 and a Dynamic Pressure of 9.7 Pounds Per Square Foot. NASA TM X-1623, 1968.

TABLE I.- PARACHUTE GEOMETRIC PROPERTIES (PREFLIGHT)

Item	Relative value	Value
Nominal diameter	D_O	16.15 m (53 ft)
Geometric porosity[1]	$0.125S_O$	25.62 m^2 (275.8 ft^2)
Total area (disk + gap + band), S_O .	$(\pi/4)D_O^2$	204.96 m^2 (2206.2 ft^2)
Disk area (includes vent)	$0.530S_O$	108.63 m^2 (1169.3 ft^2)
Disk diameter	$0.726D_O$	11.73 m (38.5 ft)
Disk circumference	$2.283D_O$	36.88 m (121.0 ft)
Gap area	$0.120S_O$	24.59 m^2 (264.7 ft^2)
Gap width	$0.042D_O$	0.67 m (2.2 ft)
Band area.	$0.350S_O$	71.74 m^2 (772.2 ft^2)
Band width	$0.121D_O$	1.95 m (6.4 ft)
Vent area	$0.005S_O$	1.02 m^2 (11.0 ft^2)
Vent diameter	$0.070D_O$	1.13 m (3.7 ft)
Length of suspension lines	$1.700D_O$	27.43 m (90 ft)

[1]Vent plus gap provide 12.5-percent geometric porosity.

TABLE II.- NOMINAL PARACHUTE MASSES

	kg	lb
Mortar cover	0.36	0.80
Deployment bag	0.27	0.60
Vent tapes	0.36	0.80
Disk (including tapes)	15.79	34.80
Gap tapes	2.05	4.51
Band (including tapes)	6.56	14.47
Suspension lines	12.85	28.33
Swivel	2.45	5.40

	kg	lb	kg	lb
Sabot assembly	2.36	5.2		
Less retention straps	-0.45	-1.0	1.91	4.20
Bridle legs	1.63	3.6		
Less unpacked portion	-0.22	-0.5	1.41	3.10
Total ejected mass			44.01	97.01

TABLE III.- MASS PROPERTIES

(a) AV-1

Condition	Mass, kg (lbm)	Center of gravity, cm (in.)			Moment and product of inertia, kg-m² (slug-ft²)					
		x'^*	y'	z'	I_{XX}	I_{YY}	I_{ZZ}	P_{XY}	P_{XZ}	P_{YZ}
At mortar fire	860.0 (1896)	86.31 (33.98)	0	-3.58 (-1.41)	595 (439)	473 (349)	456 (336)	0.58 (0.43)	2.35 (1.73)	0.22 (0.16)
With decelerator deployed	816.9 (1801)	83.41 (32.84)	0	-3.58 (-1.41)	592 (437)	454 (335)	437 (322)	.62 (.46)	2.35 (1.73)	.22 (.16)
With decelerator deployed and aeroshell dropped	655.9 (1446)	92.61 (36.46)	0	-4.47 (-1.76)	355 (262)	308 (227)	290 (214)	.58 (.43)	5.23 (3.86)	-.23 (-.17)

*Measured from test-vehicle theoretical apex.

(b) AV-2

Condition	Mass, kg (lbm)	Center of gravity, cm (in.)			Moment and product of inertia, kg-m² (slug-ft²)					
		x'^*	y'	z'	I_{XX}	I_{YY}	I_{ZZ}	P_{XY}	P_{XZ}	P_{YZ}
At mortar fire	860.5 (1897)	85.22 (33.55)	0	-3.58 (-1.41)	590 (435)	462 (341)	449 (331)	0.49 (0.36)	1.48 (1.09)	-0.24 (-0.18)
With decelerator deployed	817.4 (1802)	82.25 (32.38)	0	-3.58 (-1.41)	588 (434)	446 (329)	433 (319)	.56 (.41)	1.48 (1.09)	-.24 (-.18)
With decelerator deployed and aeroshell dropped	655.5 (1445)	91.29 (35.92)	0	-4.47 (-1.76)	347 (256)	297 (219)	283 (209)	.76 (.56)	4.23 (3.12)	-.43 (-.52)

*Measured from test-vehicle theoretical apex.

TABLE III.- MASS PROPERTIES — Concluded

(c) AV-3[†]

Condition	Mass, kg (lbm)	Center of gravity, cm (in.)			Moment and product of inertia, kg-m^2 (slug-ft^2)					
		x'*	y'	z'	I_{XX}	I_{YY}	I_{ZZ}	P_{XY}	P_{XZ}	P_{YZ}
At mortar fire	862.3 (1901)	84.68 (33.34)	0.15 (0.06)	-3.43 (-1.35)	555 (409)	460 (339)	401 (296)	-0.07 (-0.05)	1.33 (0.98)	1.45 (1.07)
With decelerator deployed	819.2 (1806)	81.69 (32.16)	.15 (.06)	-3.43 (-1.35)	553 (408)	443 (327)	385 (284)	0	1.33 (0.98)	1.45 (1.07)
With decelerator deployed and aeroshell dropped	659.5 (1454)	90.35 (34.57)	.13 (.05)	-4.29 (-1.69)	273 (201)	297 (219)	237 (175)	-.12 (-.09)	3.89 (2.87)	1.49 (1.10)

[†]Values do not include ice which accumulated on and in this vehicle passing through rainstorms during ascent. This mass is estimated to be 12 kg ± 5 kg.

*Measured from test-vehicle theoretical apex.

(d) AV-4

Condition	Mass, kg (lbm)	Center of gravity, cm (in.)			Moment and product of inertia, kg-m^2 (slug-ft^2)					
		x'*	y'	z'	I_{XX}	I_{YY}	I_{ZZ}	P_{XY}	P_{XZ}	P_{YZ}
At mortar fire	860.5 (1897)	86.31 (33.98)	0	-3.58 (-1.41)	595 (439)	473 (349)	456 (336)	0.58 (0.43)	2.35 (1.73)	0.22 (0.16)
With decelerator deployed	817.4 (1802)	83.39 (32.83)	0	-3.58 (-1.41)	592 (437)	454 (335)	437 (322)	.62 (.46)	2.35 (1.73)	.22 (.16)
With decelerator deployed and aeroshell dropped	655.9 (1446)	92.63 (36.47)	0	-4.47 (-1.76)	355 (262)	308 (227)	290 (214)	.58 (.43)	5.23 (3.86)	-.23 (-.17)

*Measured from test-vehicle theoretical apex.

TABLE IV.- STEP INITIAL CONDITIONS, BIASES, AND SCALE FACTORS

Item	AV-1	AV-2	AV-4
Initial conditions:			
Latitude, deg	33.4007	33.3794	33.15
Longitude, deg	-106.3312	-106.2590	-106.3512
Altitude, m (ft)	43 311.0 (142 096.0)	41 264.0 (135 380.0)	44 472.0 (145 907.0)
Velocity, m/sec (ft/sec)	724.0 (2375.0)	377.0 (1236.0)	752.7 (2469.4)
γ_p, deg	10.48	12.56	13.43
γ_y, deg	-27.94	-167.74	-142.53
ψ, deg	-17.86	-173.28	-154.59
θ, deg	11.63	7.36	13.97
ϕ, deg	-87.24	106.89	114.5
Time from drop, sec	33.4	33.0	38.0
Biases:			
p, radians/sec	0.0032	0	-0.0154
q, radians/sec	0	0	-0.0106
r, radians/sec	0	0	0
a_x	0	0	0
a_y	0	0	0
a_z	0	0	0
Scale factors:			
p	1.00	0.98	0.95
q	1.00	1.00	1.00
r	1.00	1.00	1.00
a_x	1.00	1.00	1.00
a_y	1.00	1.00	1.00
a_z	1.00	1.00	1.00

TABLE V.- PARACHUTE EVENT TIMES

Event	t from drop, sec	M	q, N/m^2 (lb/ft^2)
AV-1			
Mortar fire	38.310	2.19	675 (14.10)
Line stretch	39.368	2.13	620 (12.95)
First peak load	39.970	2.03	567 (11.85)
Aeroshell separation	47.986	.91	110 (2.30)
AV-2			
Mortar fire	38.216	1.14	240 (5.01)
Line stretch	39.201	1.11	226 (4.72)
First peak load	39.840	1.08	212 (4.43)
Aeroshell separation	47.300	.64	72 (1.50)
AV-3			
Mortar fire	16.472	0.465	340 (7.10)
Line stretch	17.422	.477	365 (7.62)
First peak load	18.247	.445	320 (6.68)
Aeroshell separation	30.239	.185	62 (1.30)
AV-4			
Mortar fire	40.423	2.08	500 (10.44)
Line stretch	41.429	2.03	460 (9.61)
First peak load	41.995	1.96	430 (8.98)
Aeroshell separation	48.073	1.15	140 (2.92)
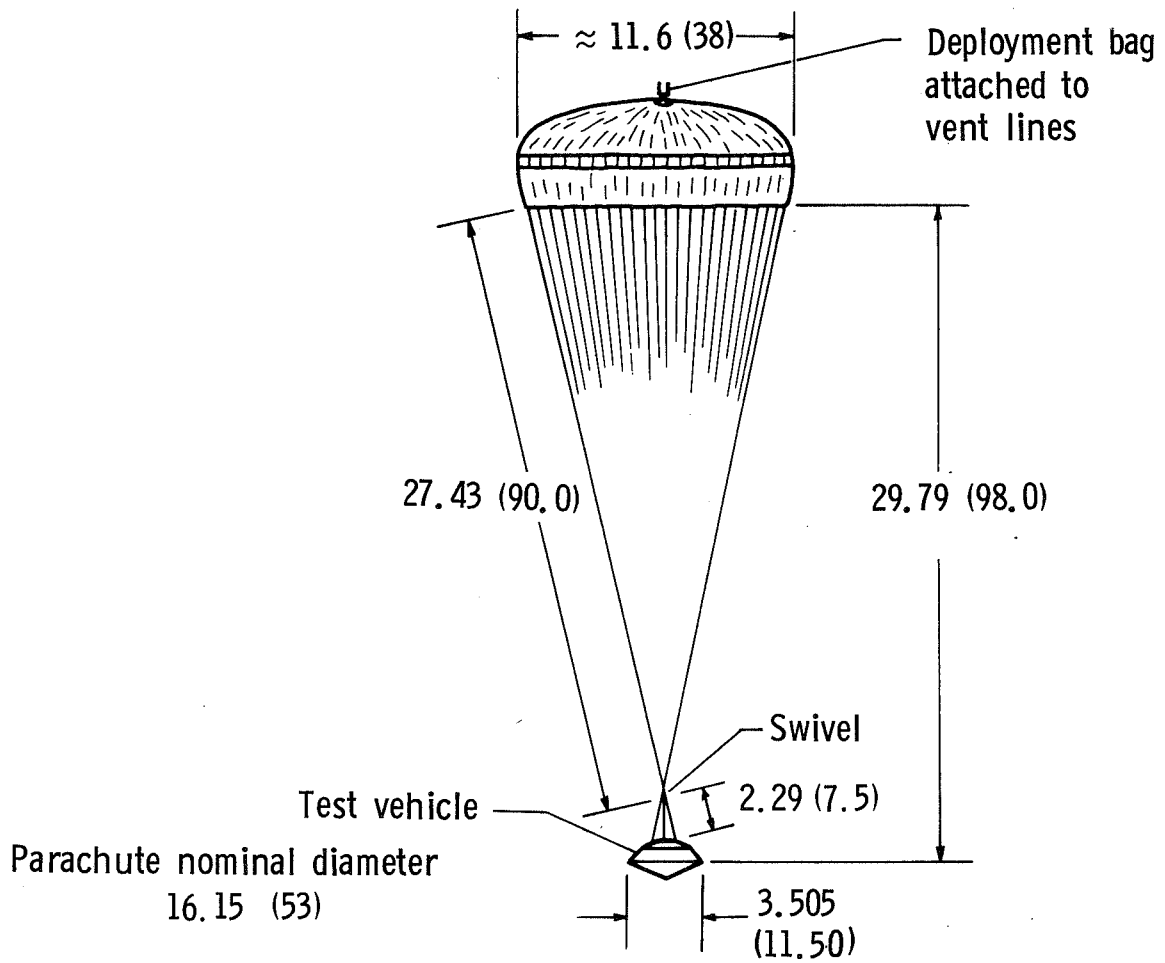
Figure 1.- Disk-gap-band parachute system. Dimensions are in meters (ft).
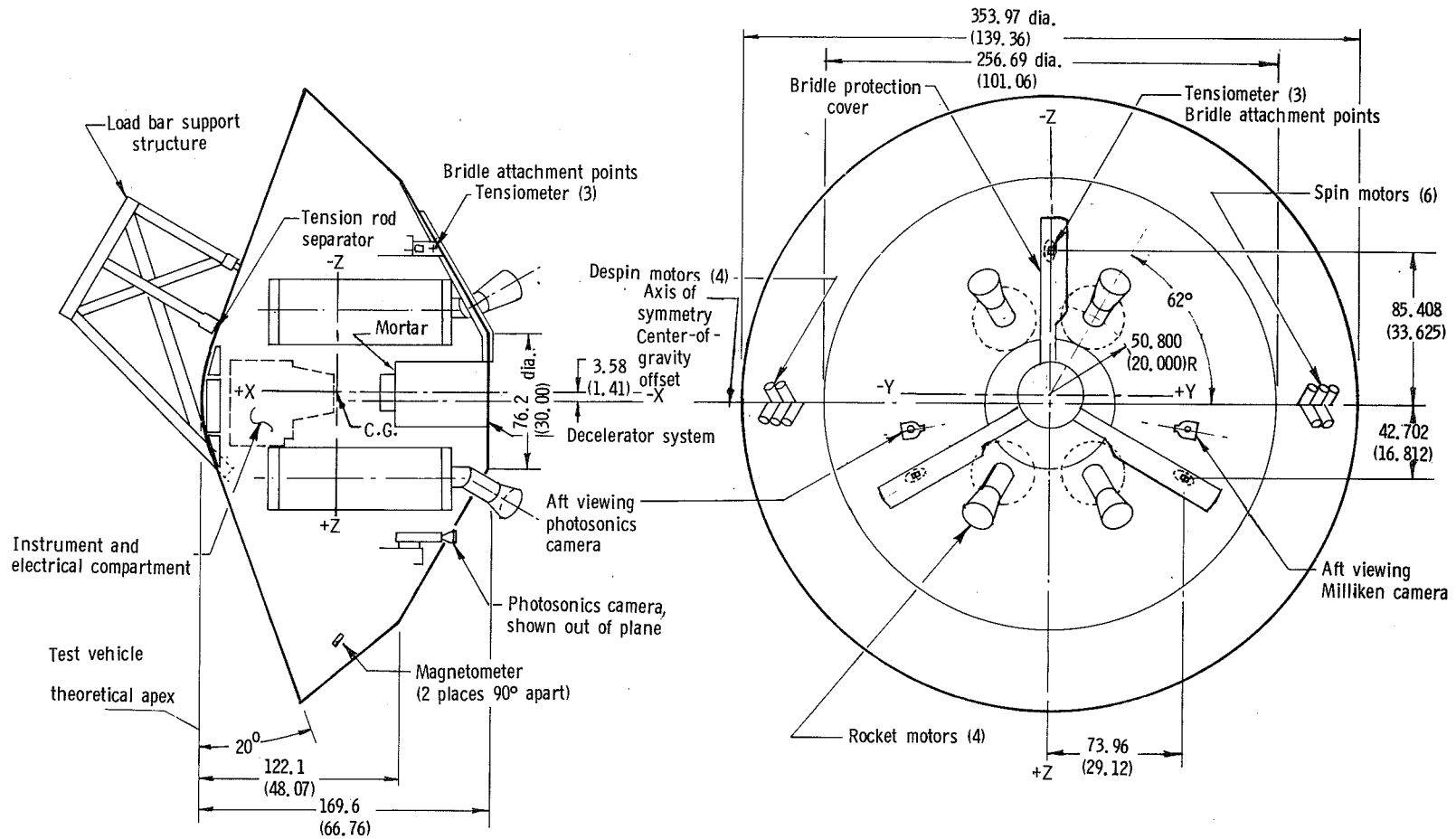
Figure 2.- Test vehicle, general arrangement (supersonic test). Dimensions are in cm (in).
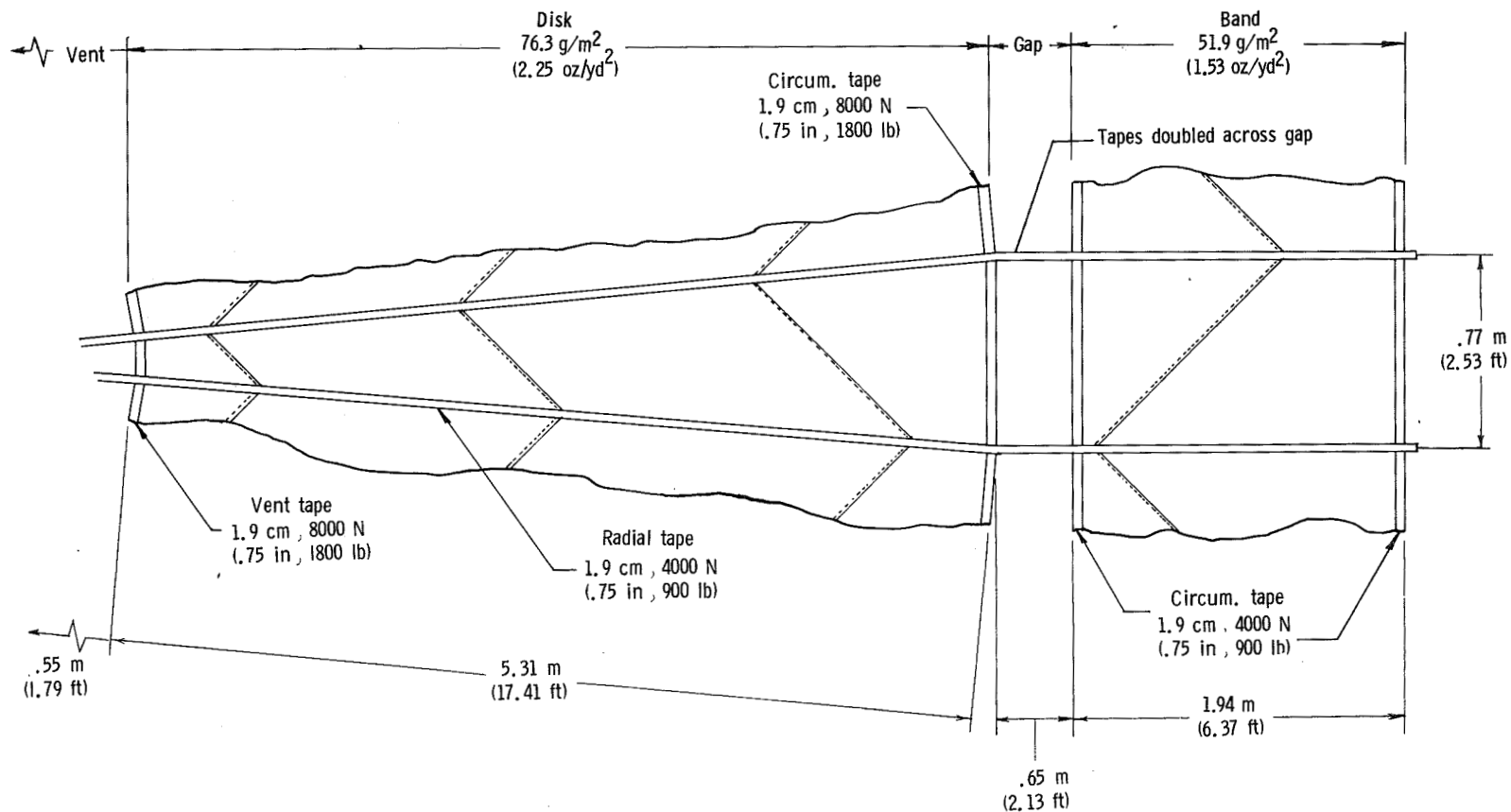
Figure 3.- Parachute gore construction, including tape widths and nominal strengths.
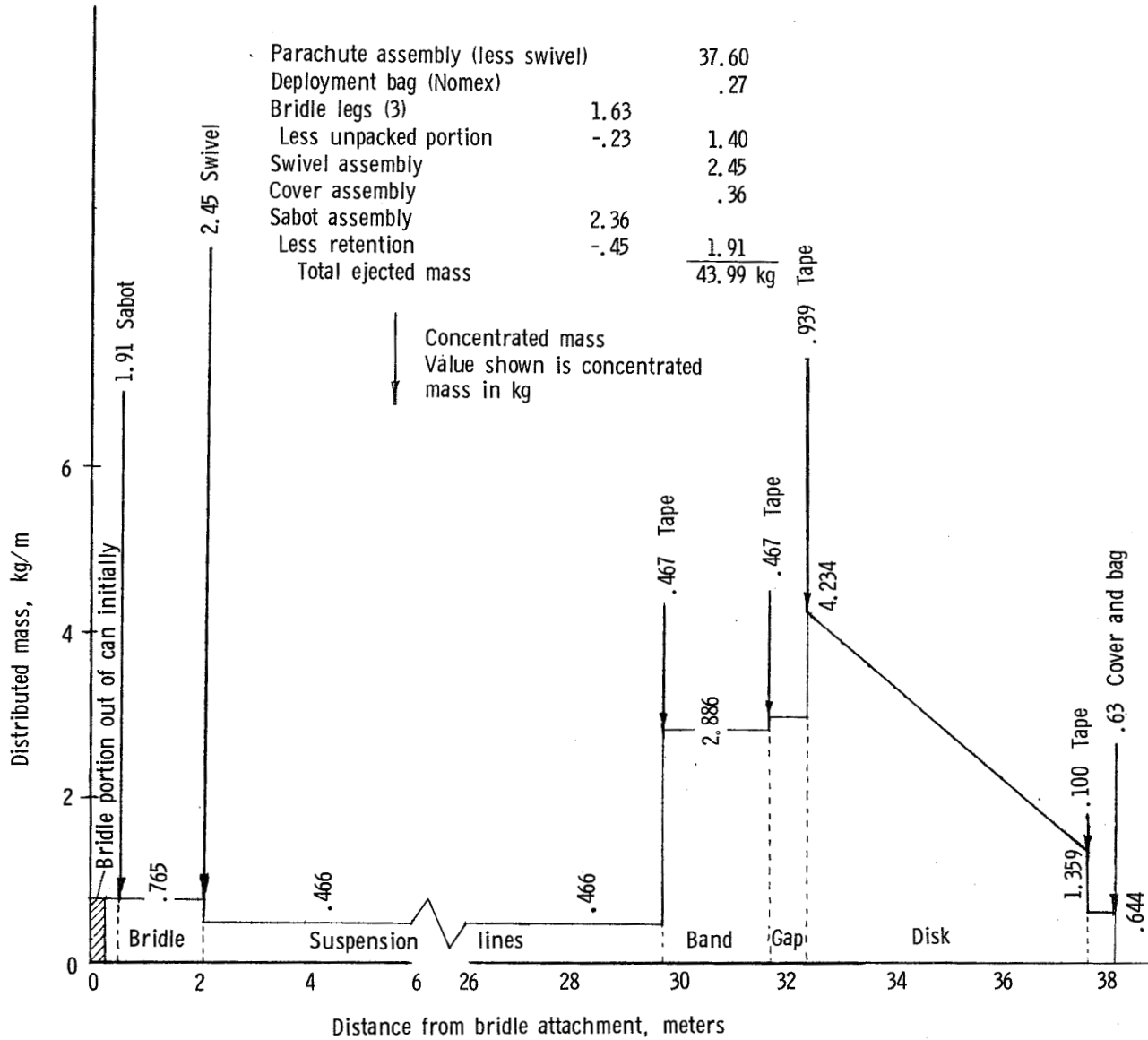
Figure 4.- Mass distribution of extending parachute. Heavy arrows show concentrated masses in kg.
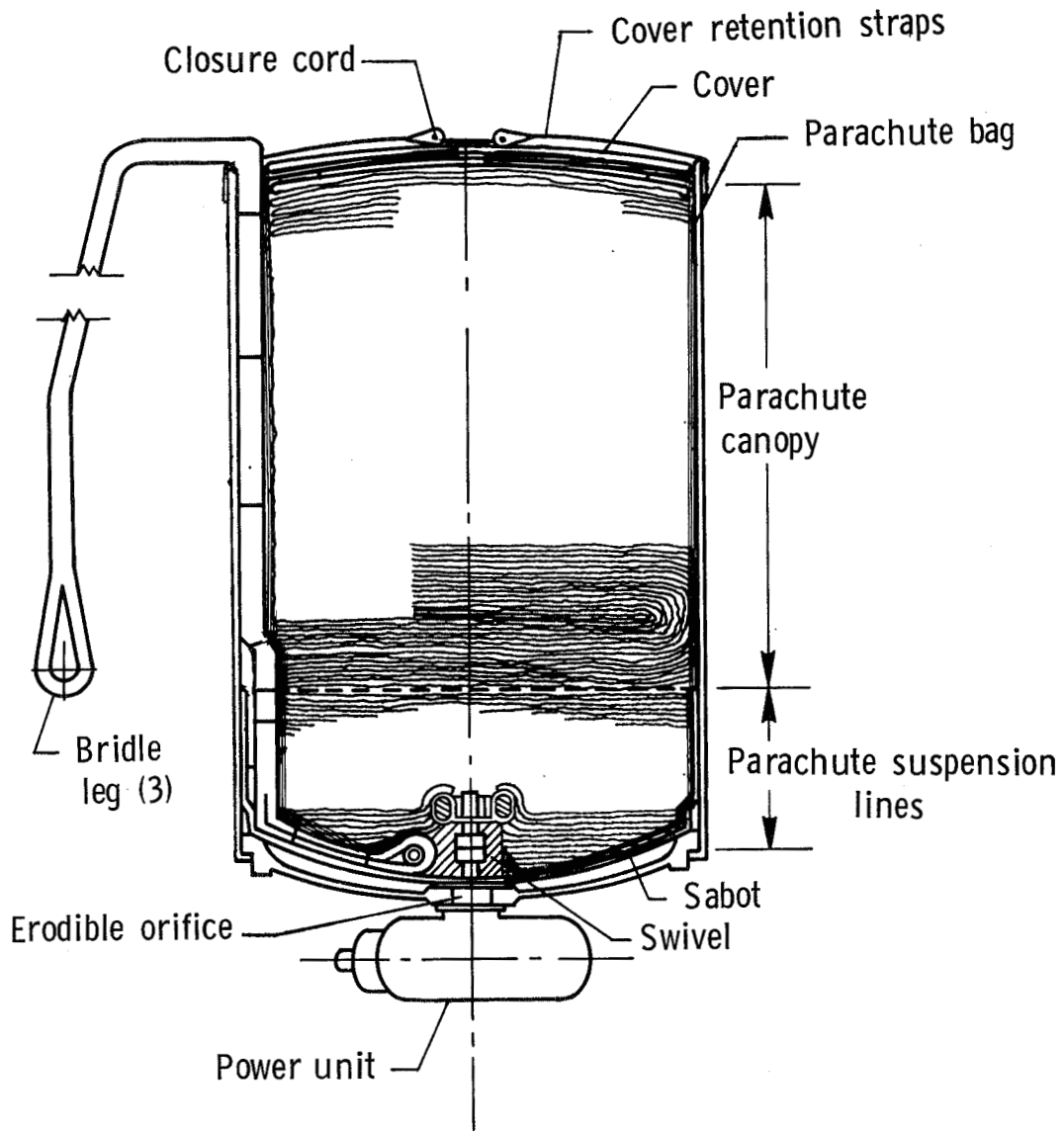
Figure 5.- Sketch of mortar with parachute pack.

The labels in the figure read:
- Closure cord
- Cover retention straps
- Cover
- Parachute bag
- Parachute canopy
- Parachute suspension lines
- Bridle leg (3)
- Sabot
- Swivel
- Erodible orifice
- Power unit

Mortar fire
t ≈ 38 sec

Full open

Float to WSMR

Despin
t = 33 sec

Aeroshell
separation
t ≈ 48 sec

Test-vehicle release
t = 0

Spinup
t = 1 sec

Balloon launch
(Roswell) →

Main rocket ignition
t = 2 sec

Impact (WSMR)
t ≈ 25 min

Figure 6.- Typical sequence of events. Powered flight.

L-74-1148

Figure 7.- Photograph of descending parachute and payload after aeroshell separation.
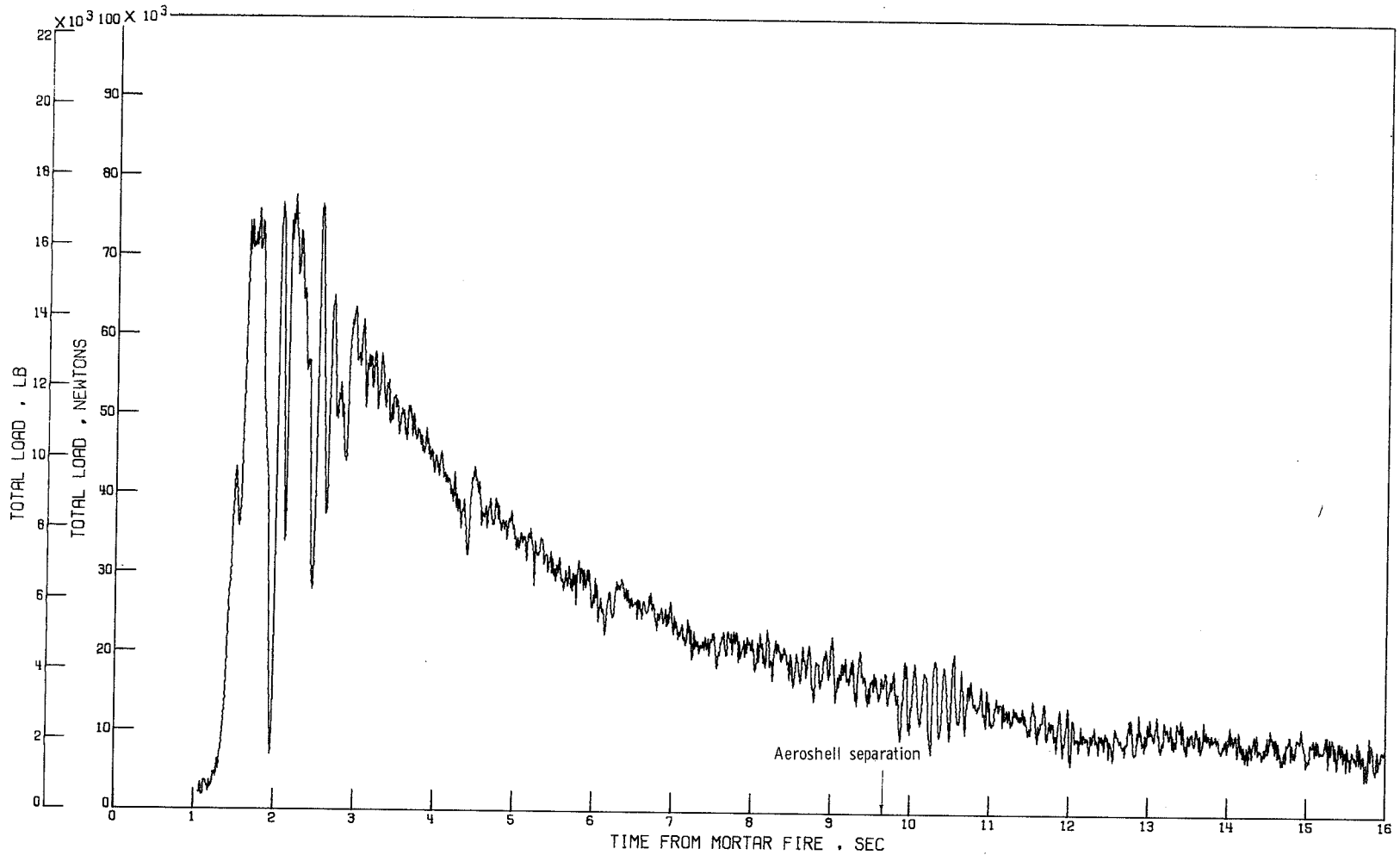
Figure 8.- Variation of total load from tensiometers with time from mortar fire (38.31 sec after drop). AV-1.
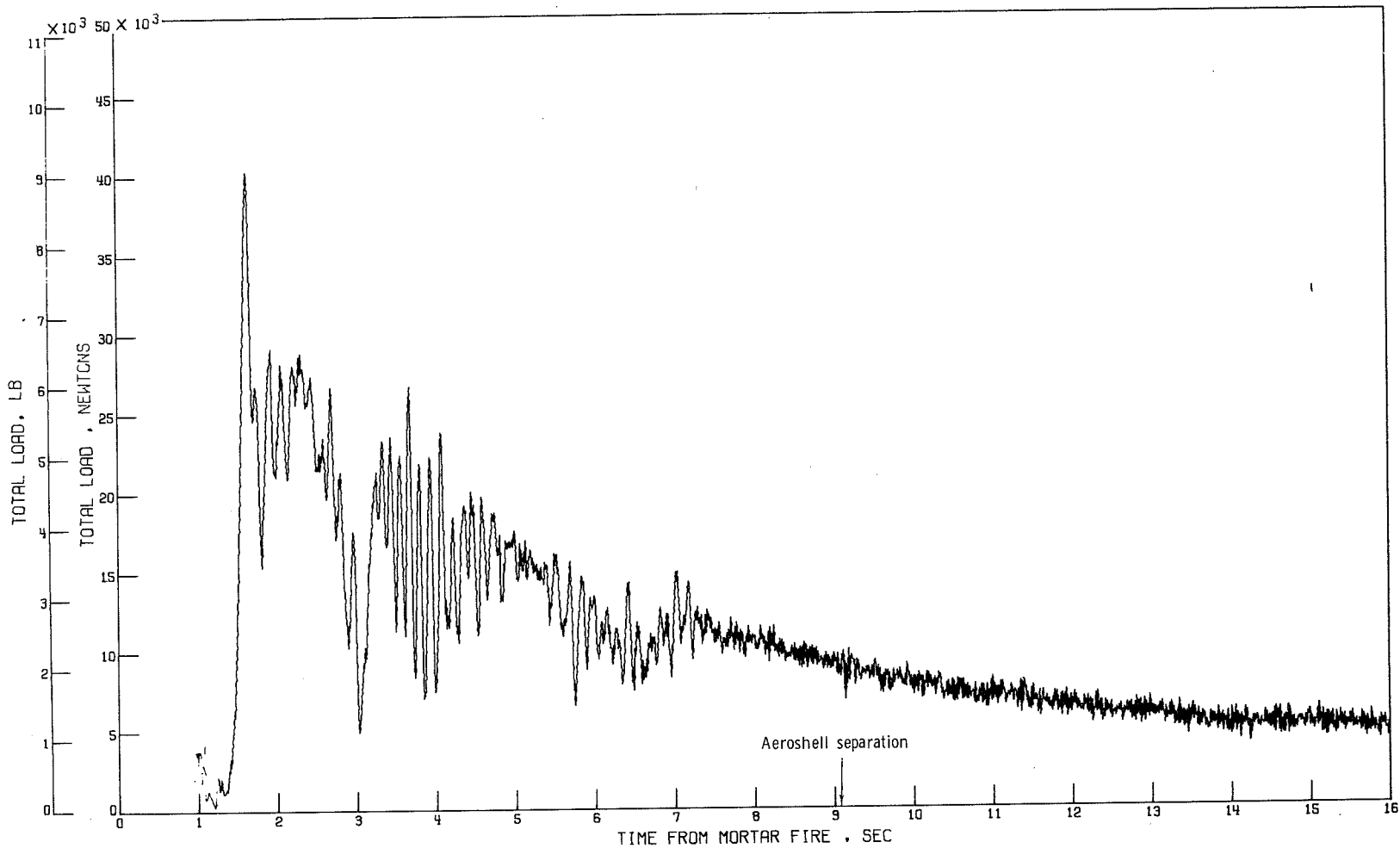
Figure 9.- Variation of total load from tensiometers with time from mortar fire (38.216 sec after drop).   AV-2.
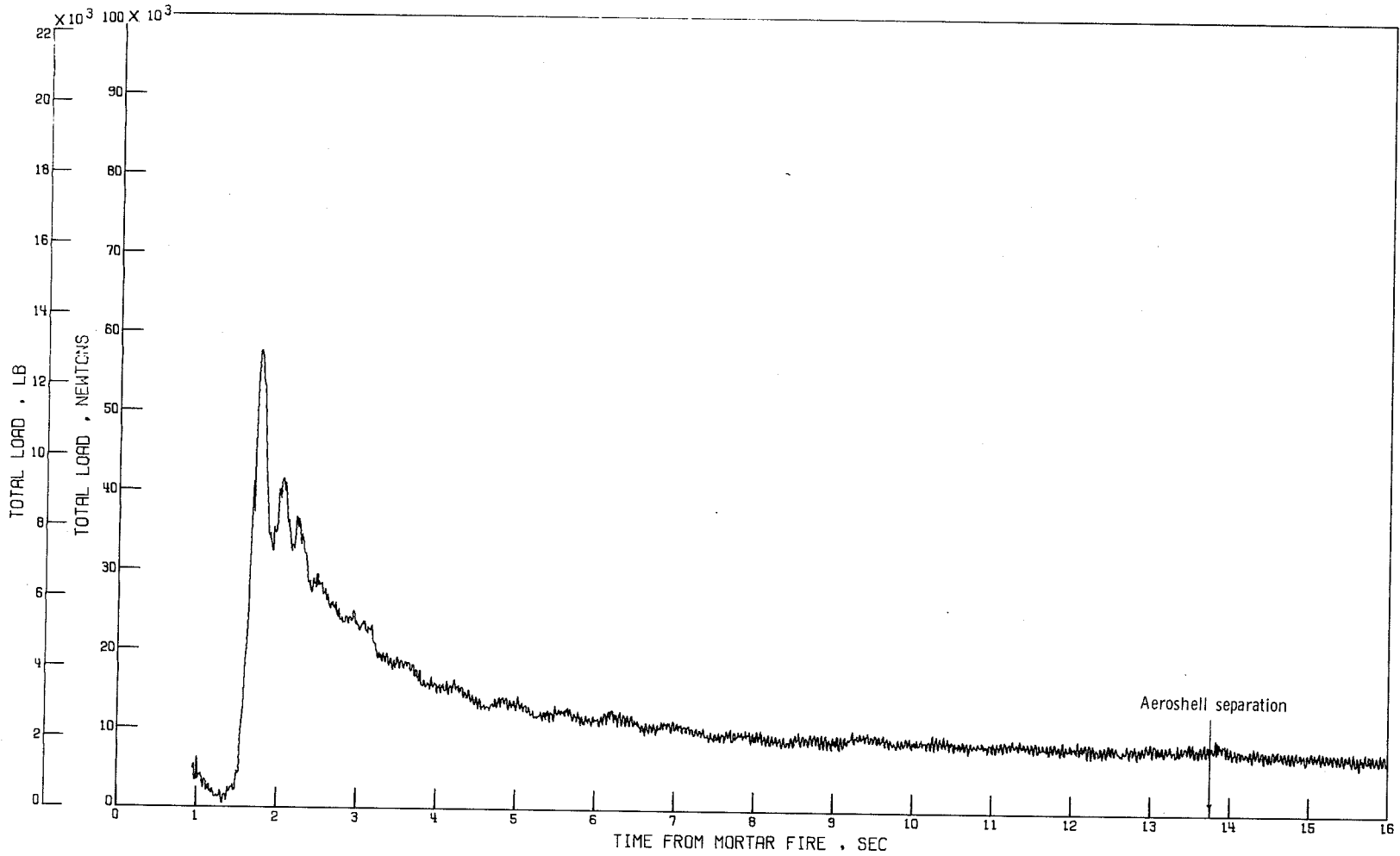
Figure 10.- Variation of total load from tensiometers with time from mortar fire (16.472 sec after drop).   AV-3.
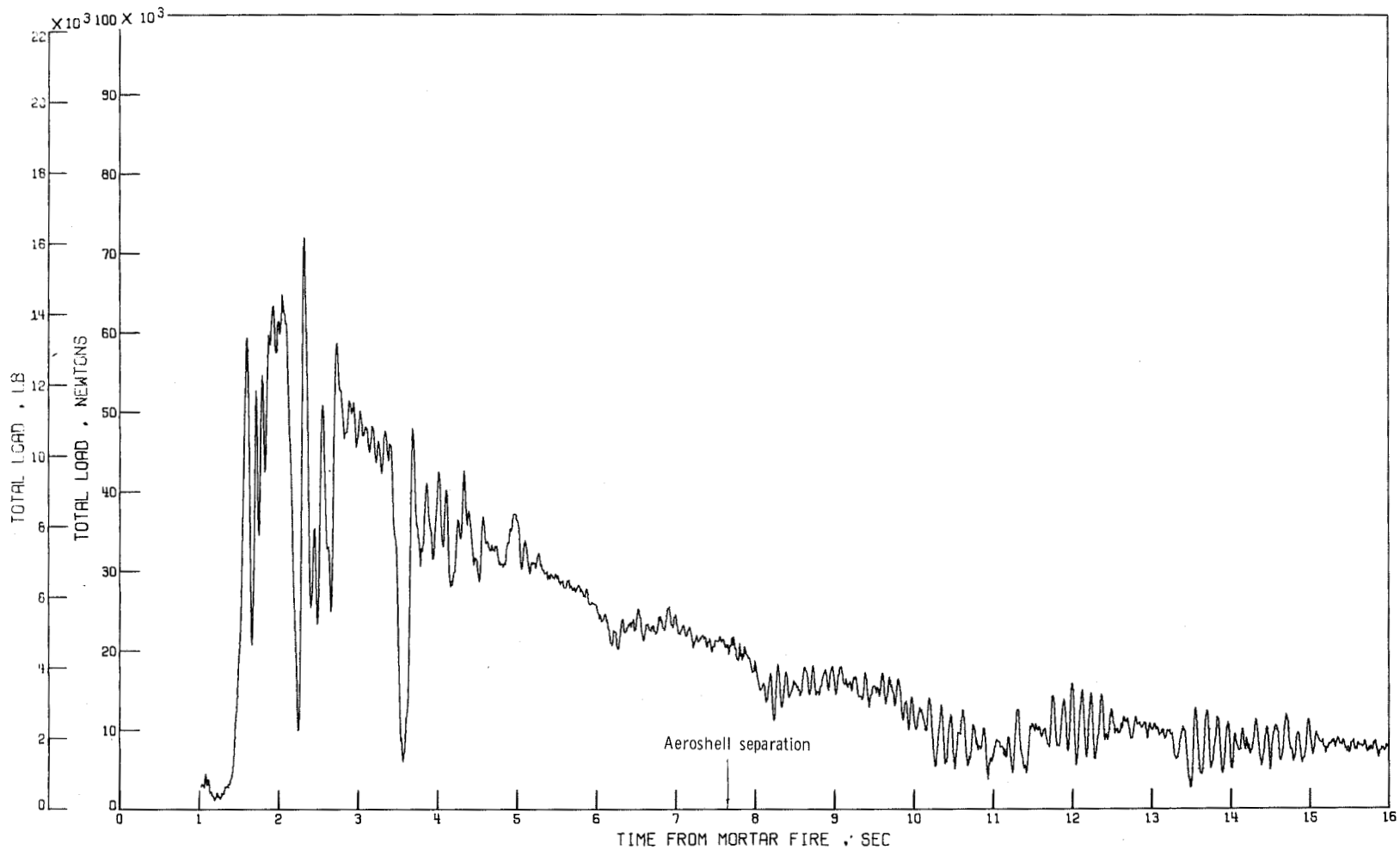
Figure 11.- Variation of total load from tensiometers with time from mortar fire (40.423 sec after drop). AV-4.
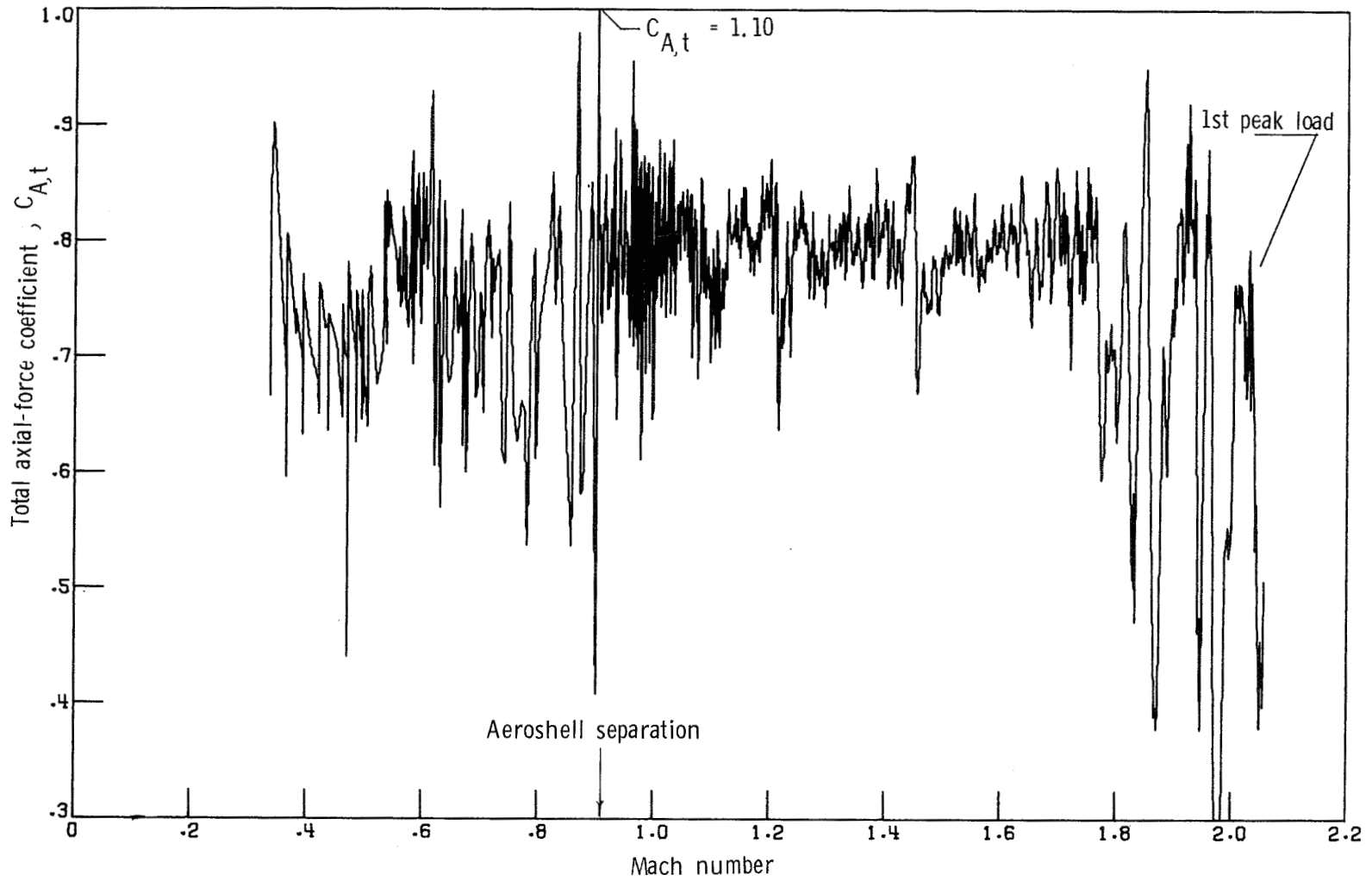
Figure 12.- Variation of AV-1 total axial-force coefficient with Mach number from accelerometer data.
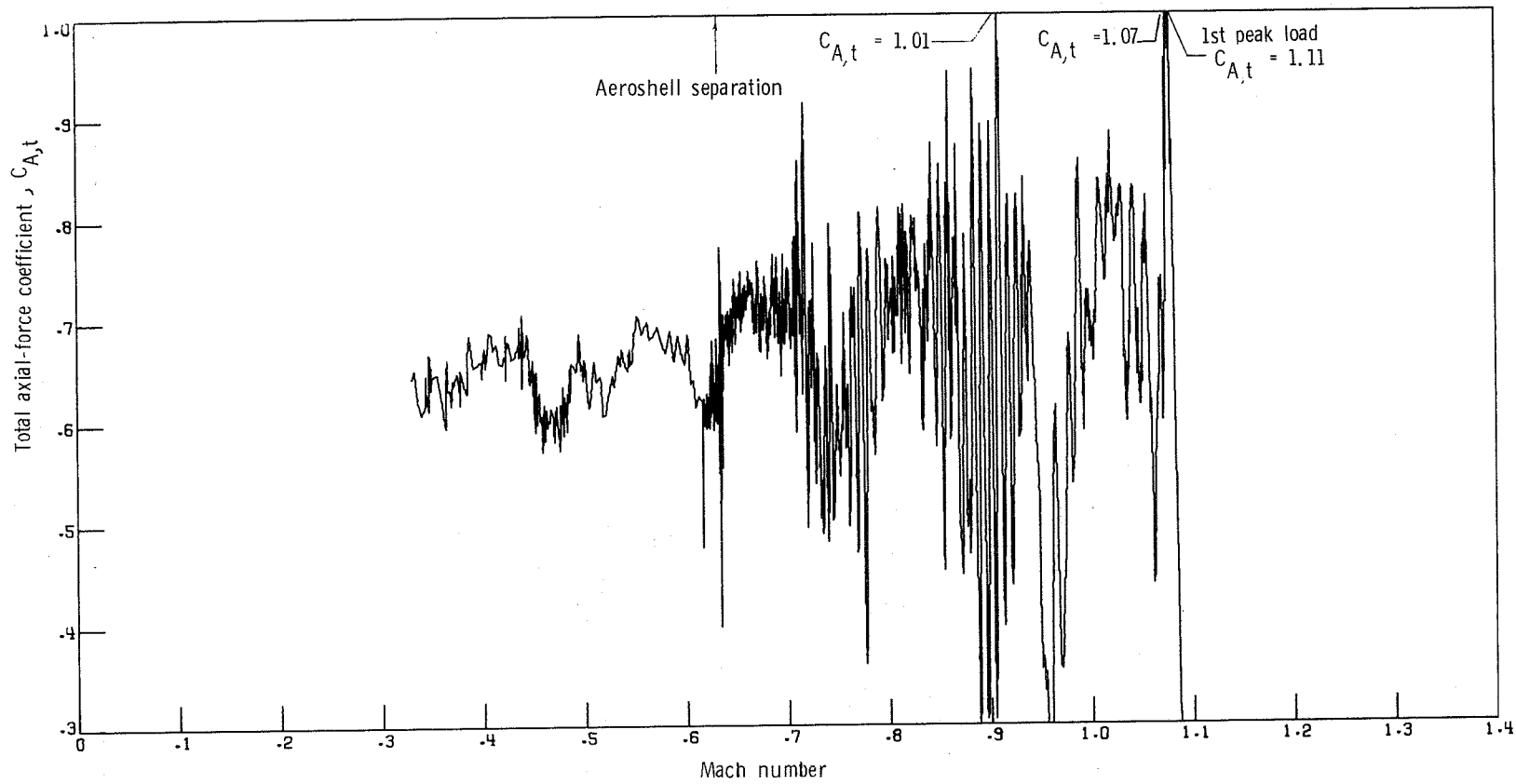
Figure 13.- Variation of AV-2 total axial-force coefficient with Mach number from accelerometer data.
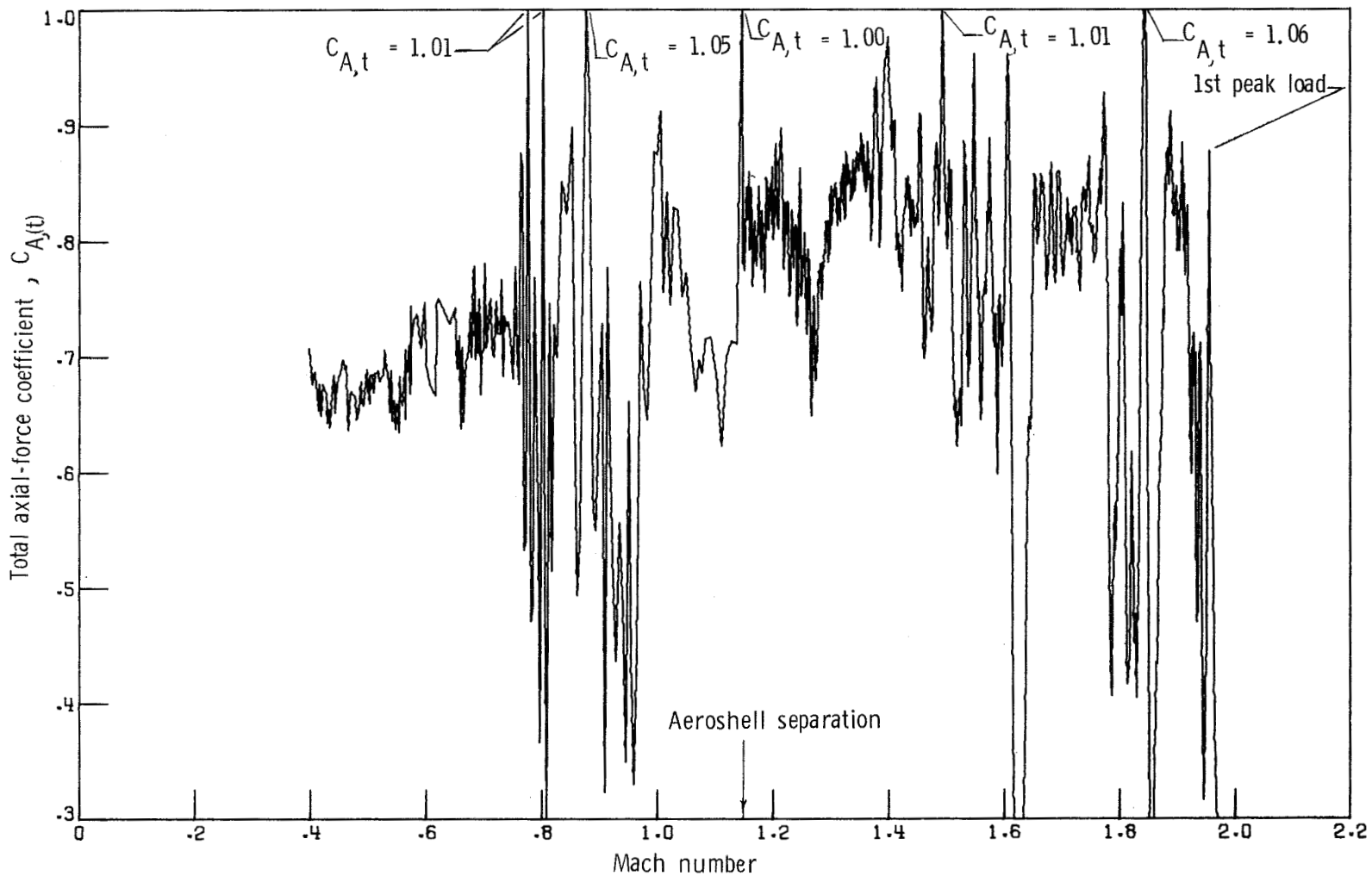
Figure 14.- Variation of AV-4 total axial-force coefficient with Mach number from accelerometer data.
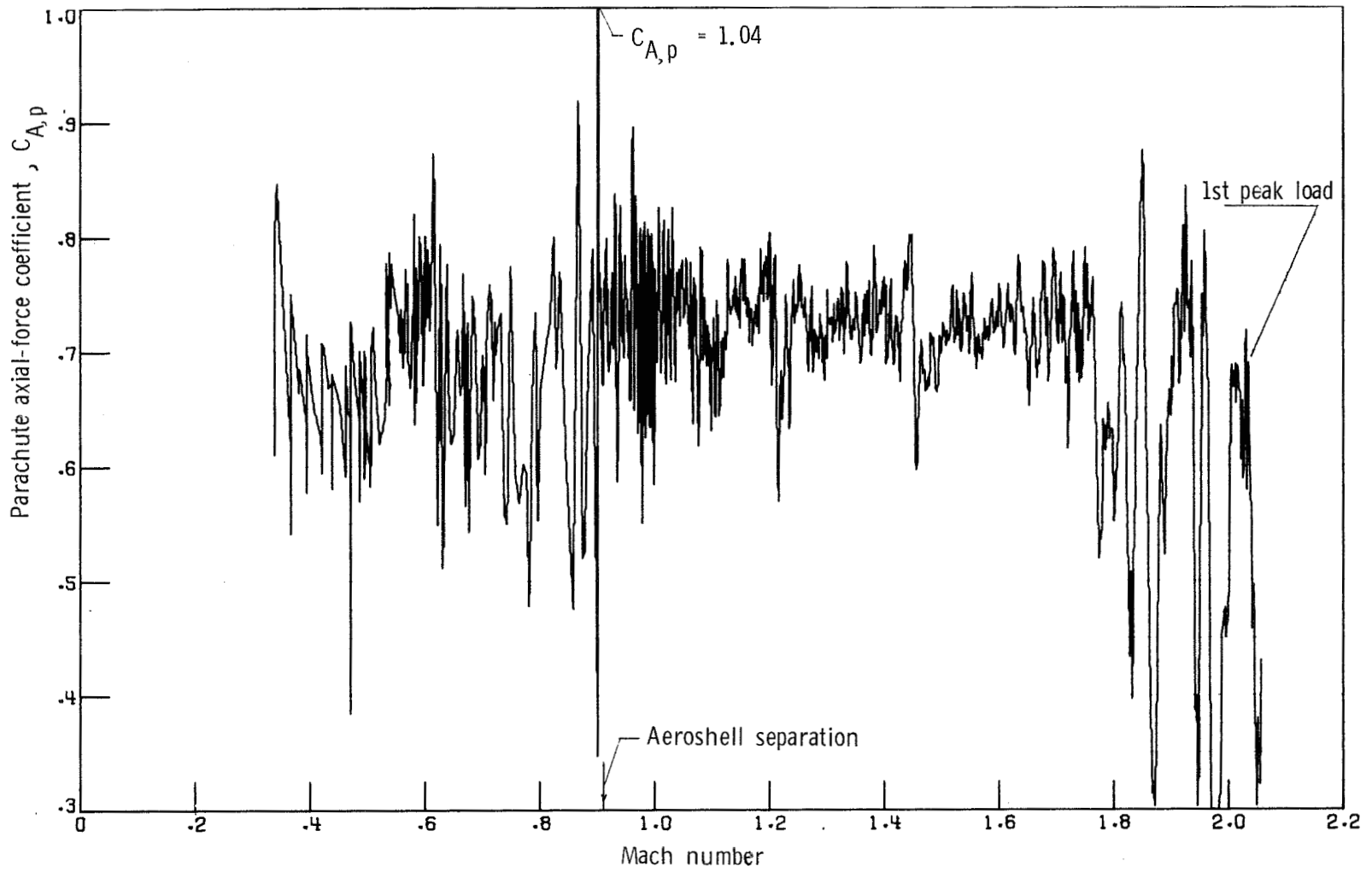
Figure 15.- Variation of AV-1 parachute axial-force coefficient with Mach number from accelerometer data.
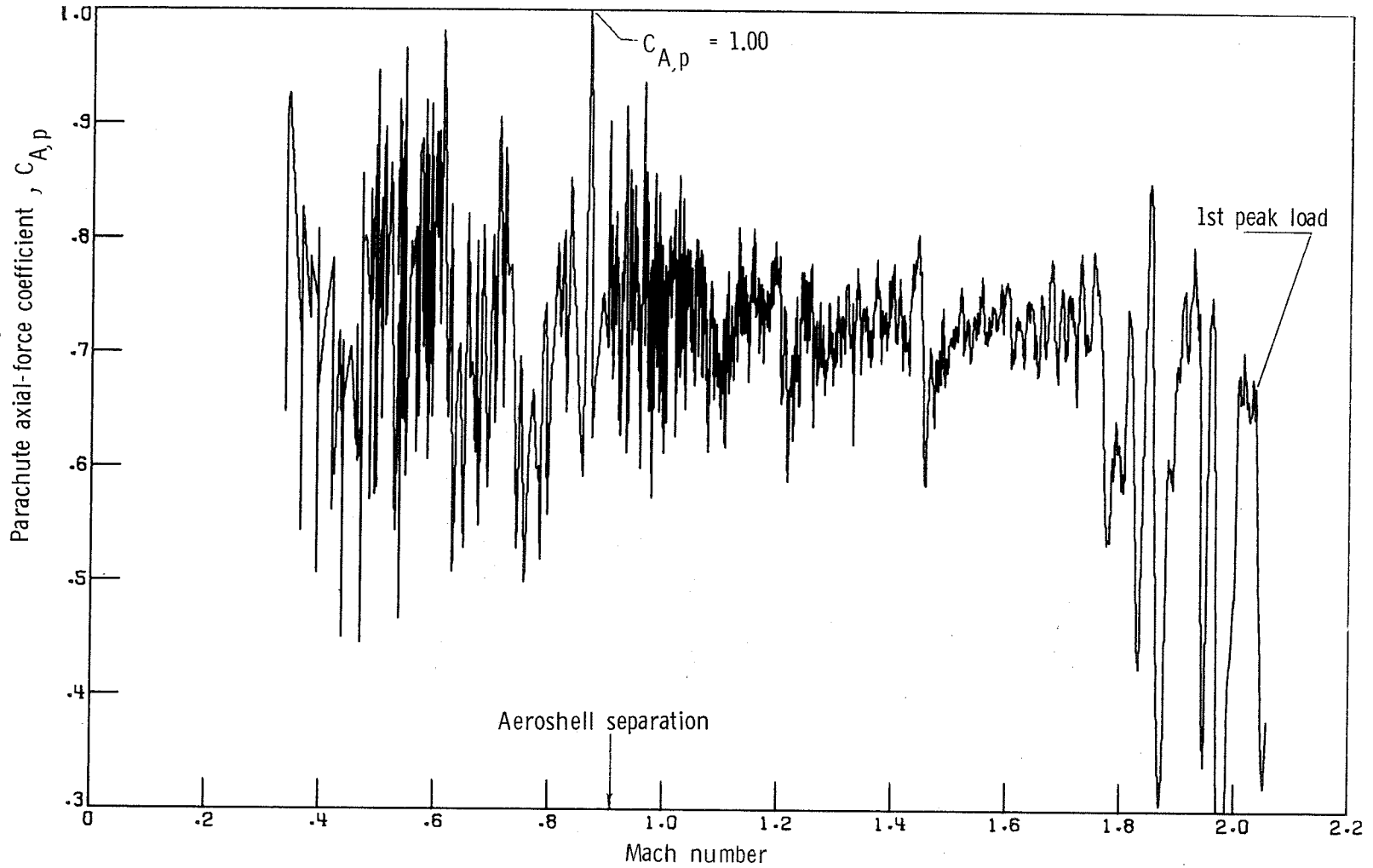
Figure 16.- Variation of AV-1 parachute axial-force coefficient with Mach number from tensiometer data.
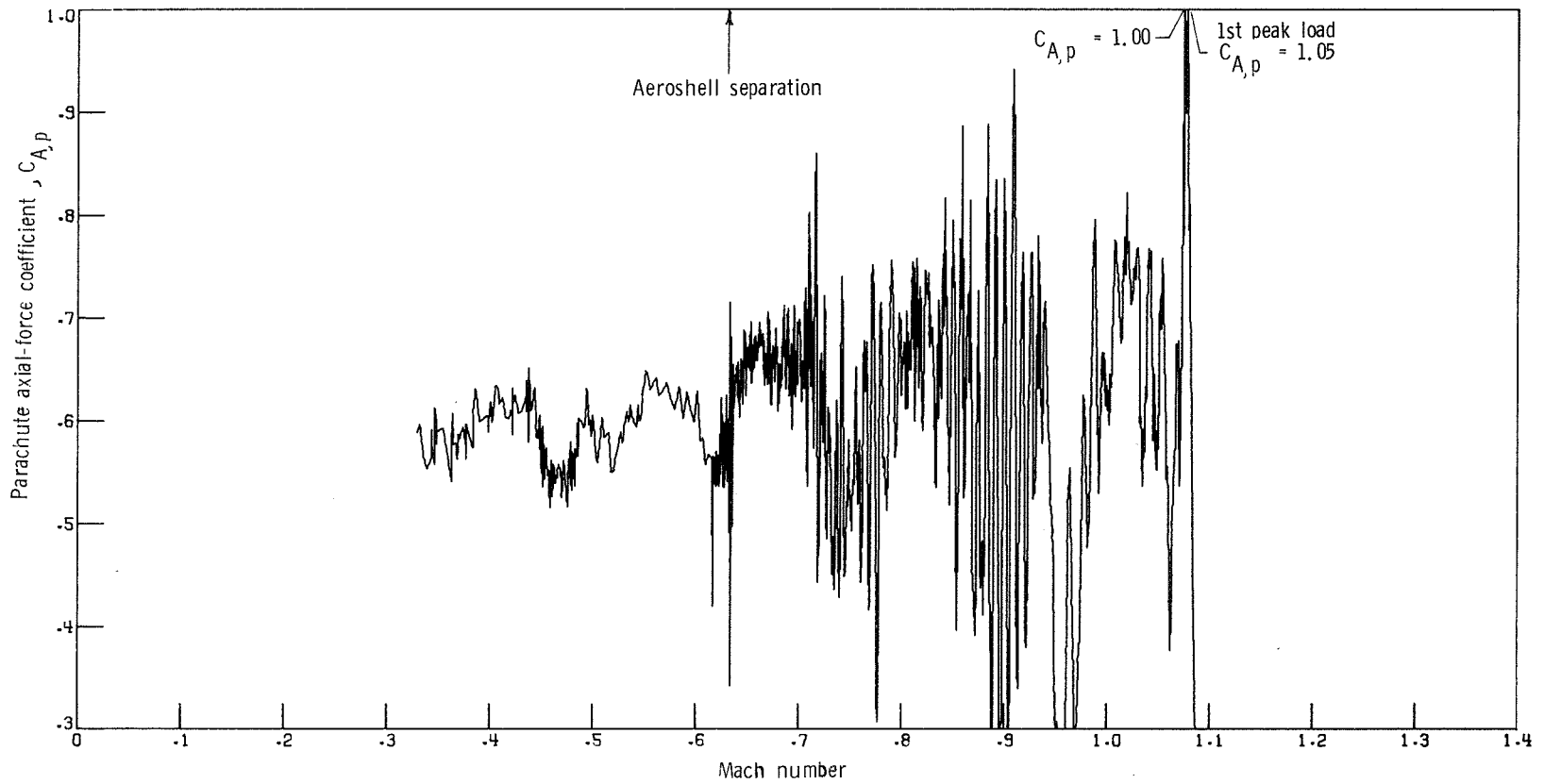
Figure 17.- Variation of AV-2 parachute axial-force coefficient with Mach number from accelerometer data.
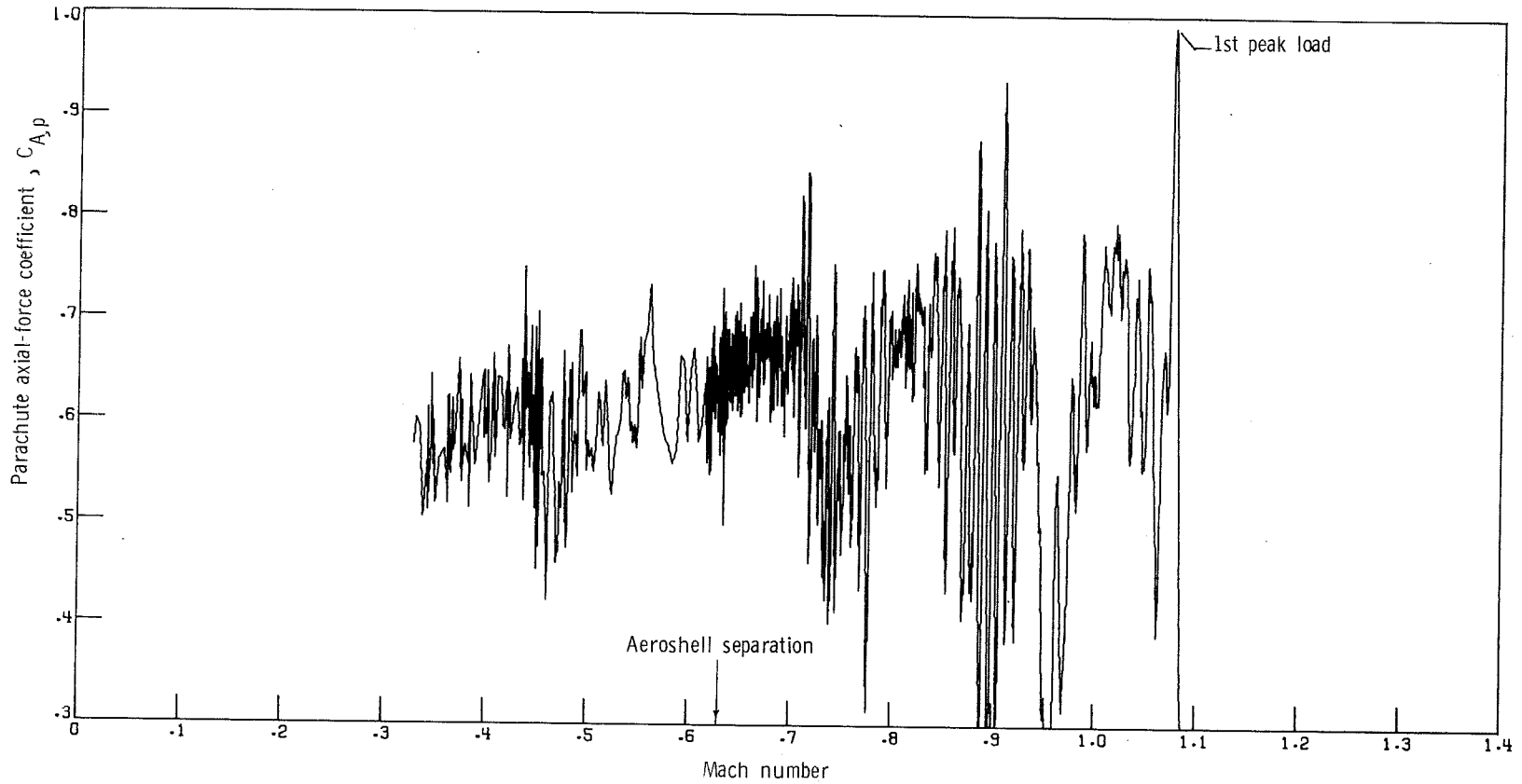
Figure 18.- Variation of AV-2 parachute axial-force coefficient with Mach number from tensiometer data.
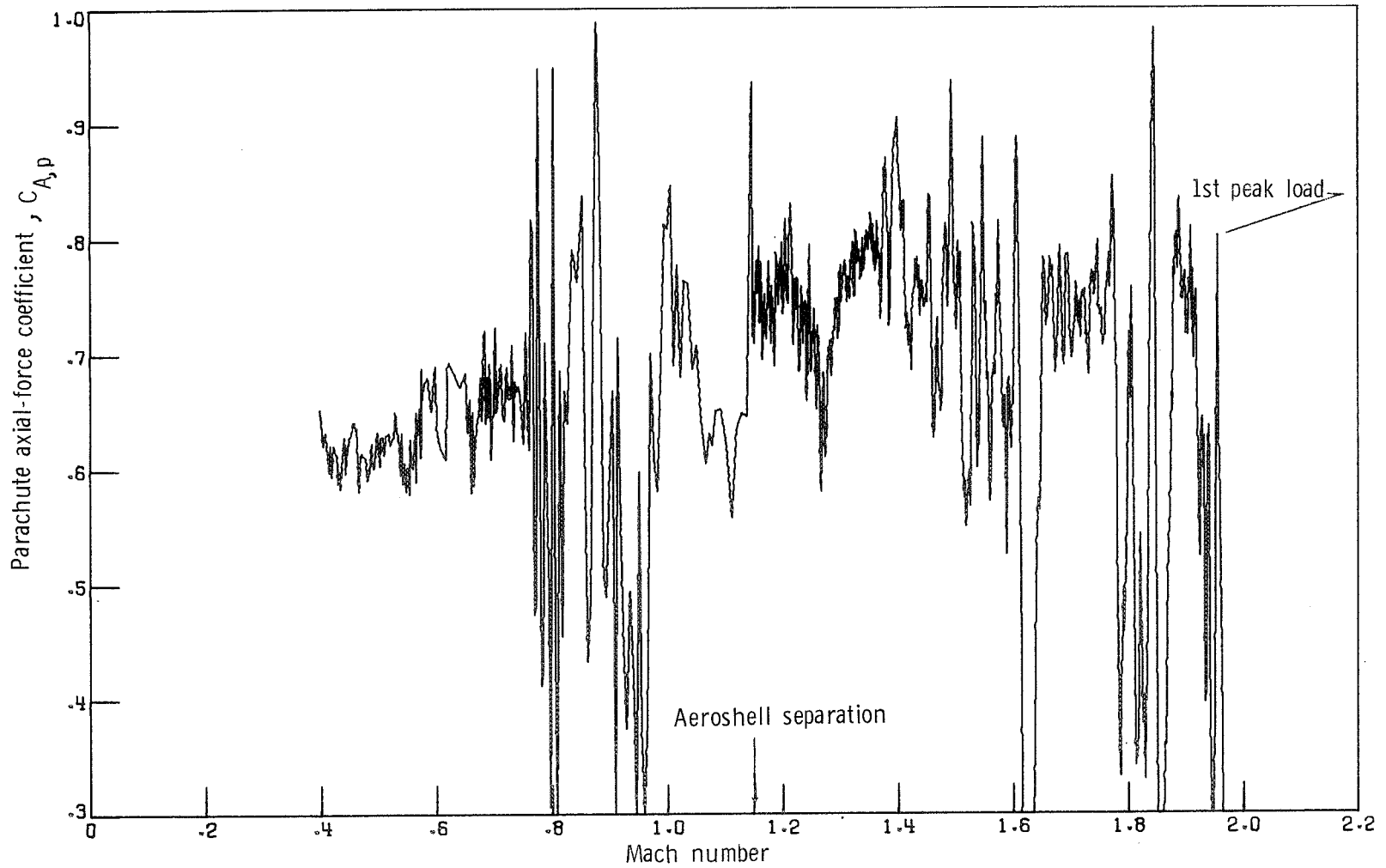
Figure 19.- Variation of AV-4 parachute axial-force coefficient with Mach number from accelerometer data.
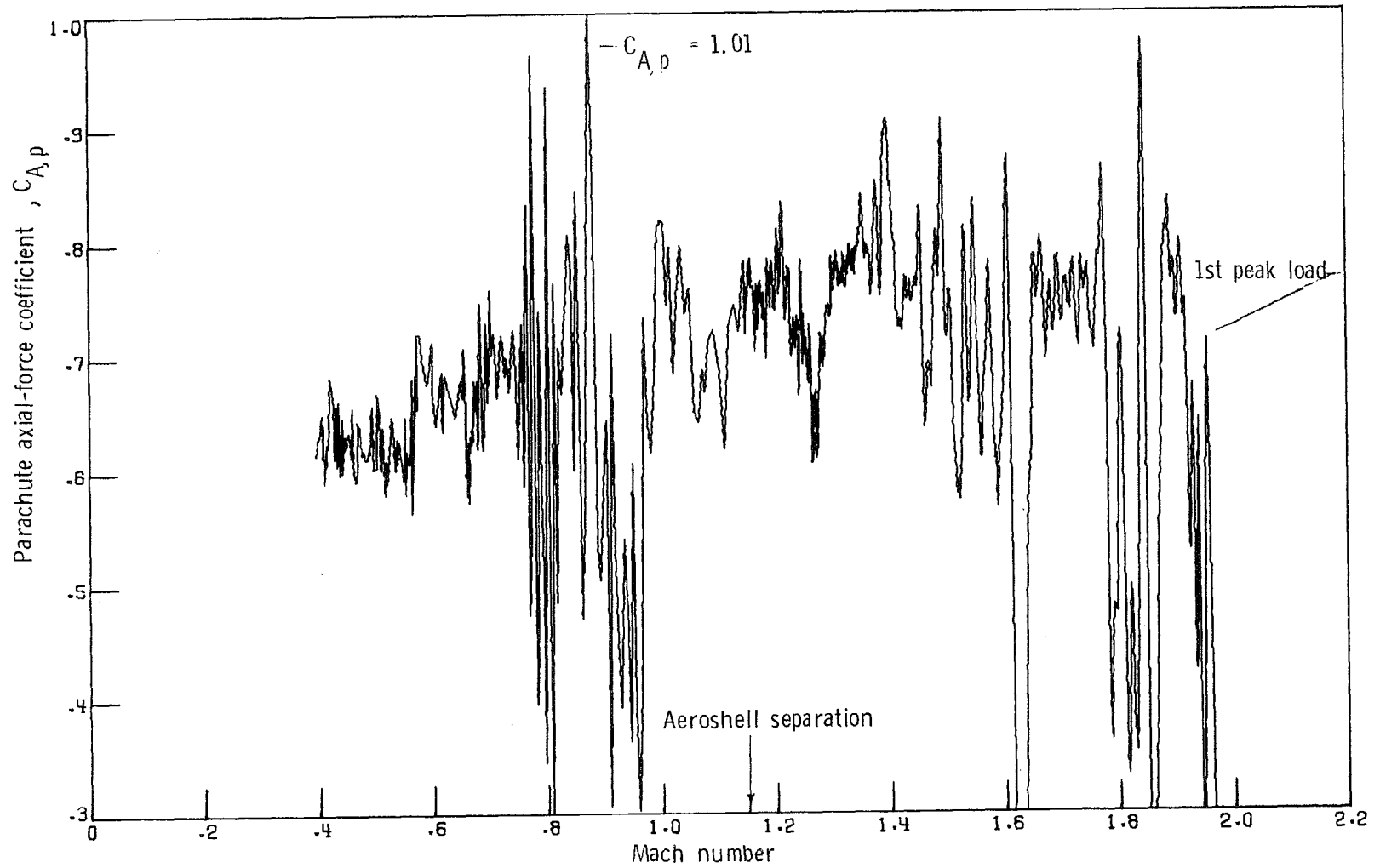
Figure 20.- Variation of AV-4 parachute axial-force coefficient with Mach number from tensiometer data.
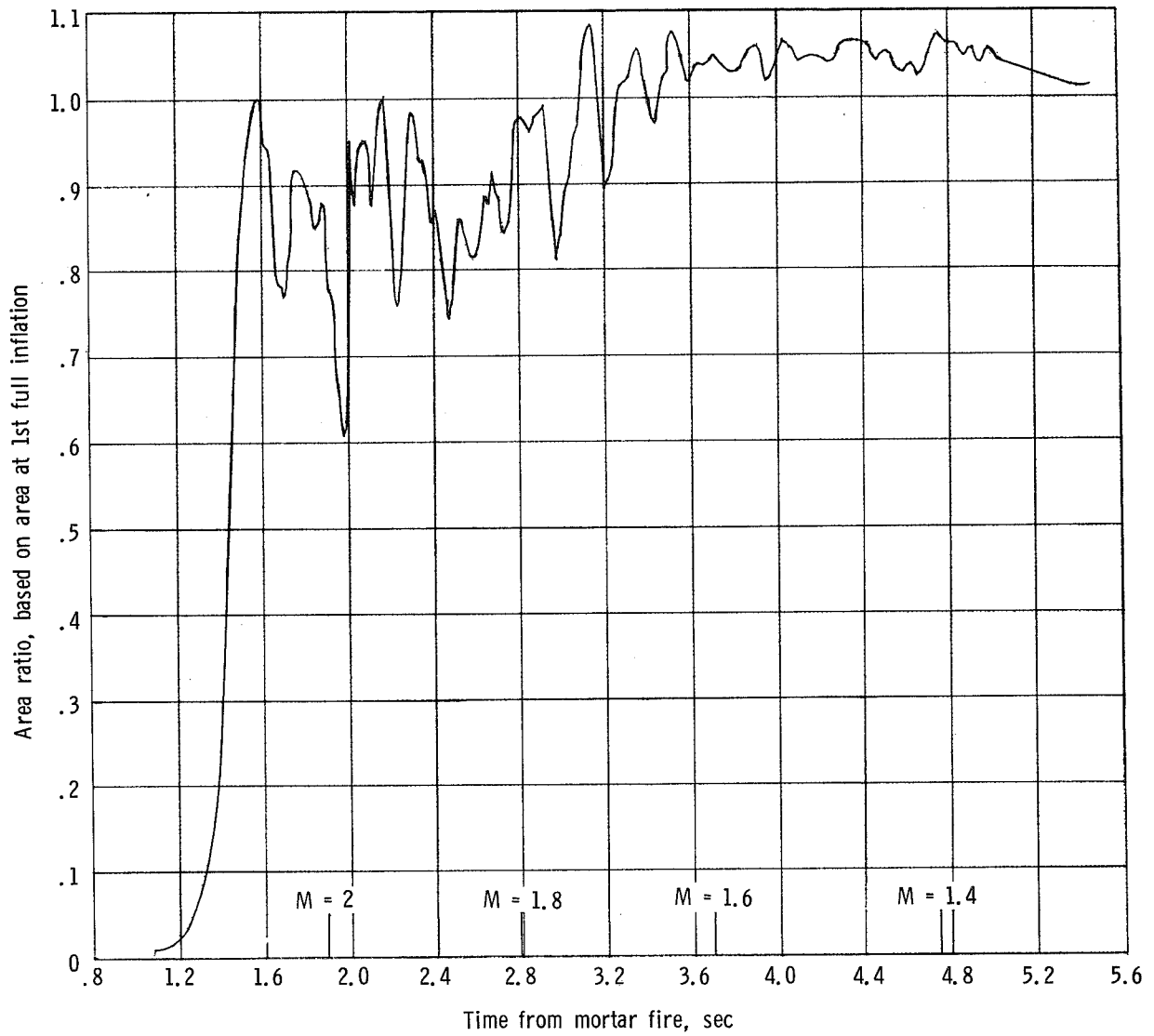
Figure 21.- Variation of parachute area ratio with time from mortar fire (38.310 sec from drop).   AV-1.
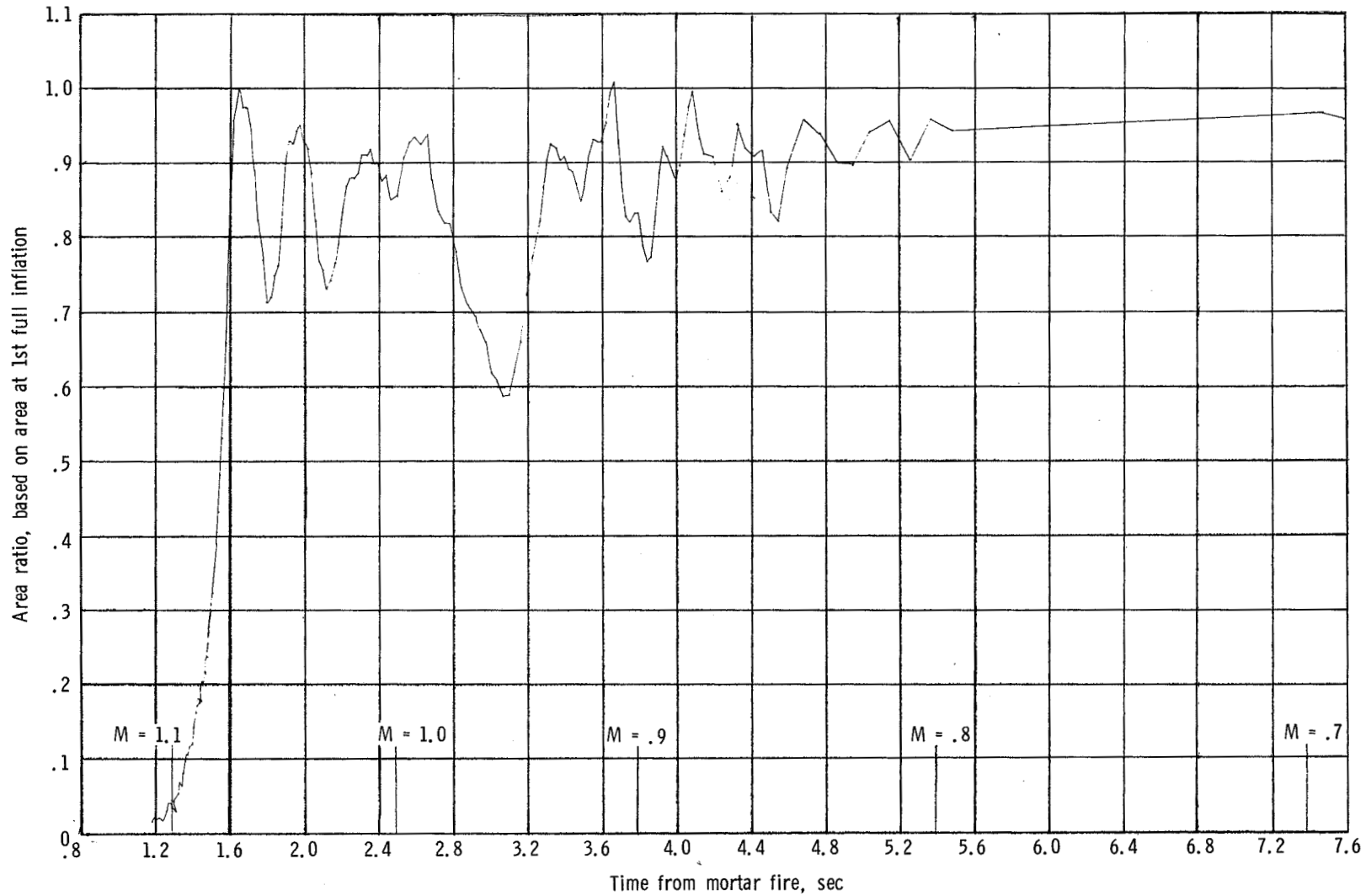
Figure 22.- Variation of parachute area ratio with time from mortar fire (38.216 sec from drop). AV-2.
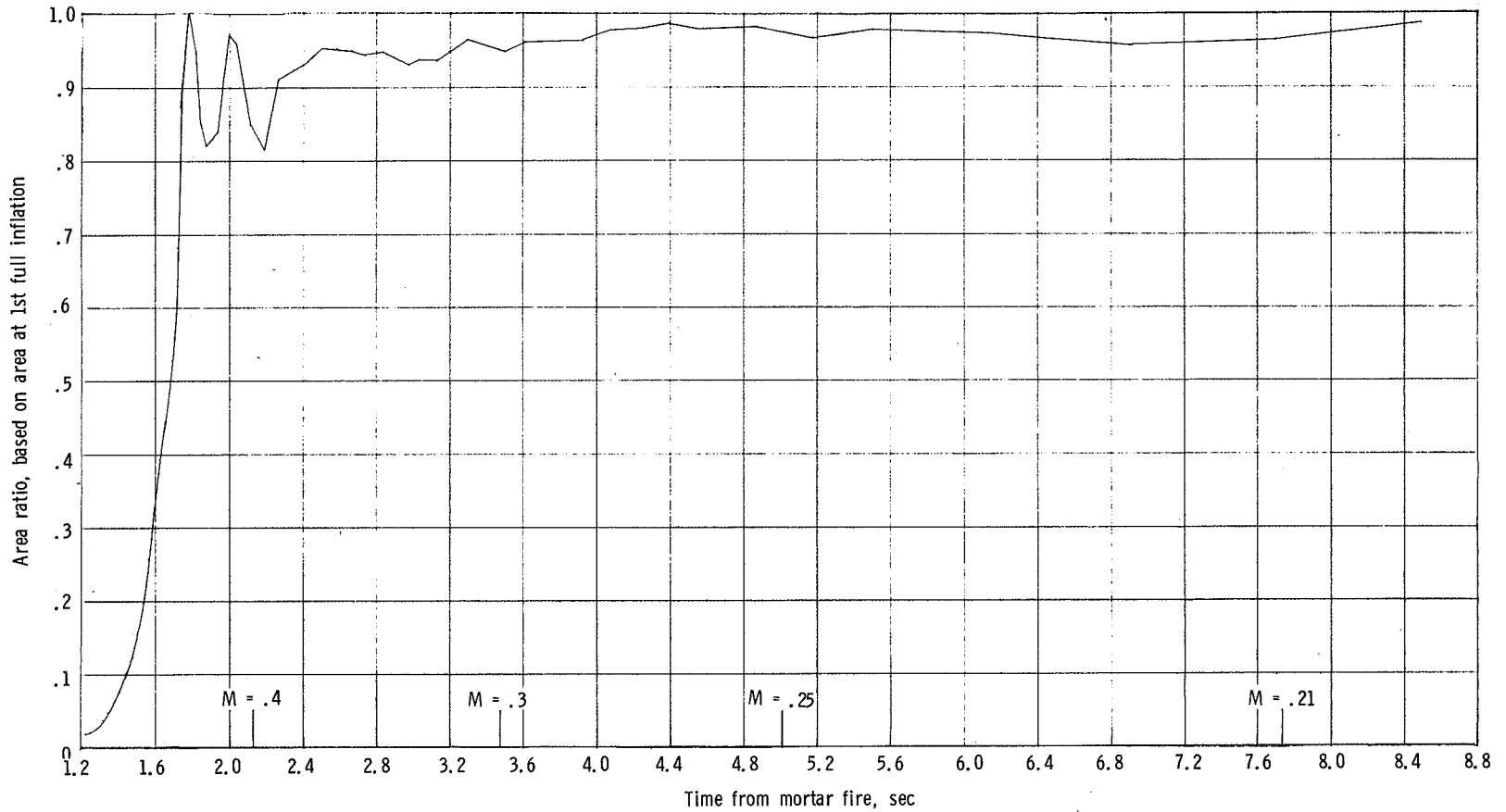
Figure 23.- Variation of parachute area ratio with time from mortar fire (16.472 sec from drop) and 1.2 to 8.8 seconds after mortar fire. AV-3.
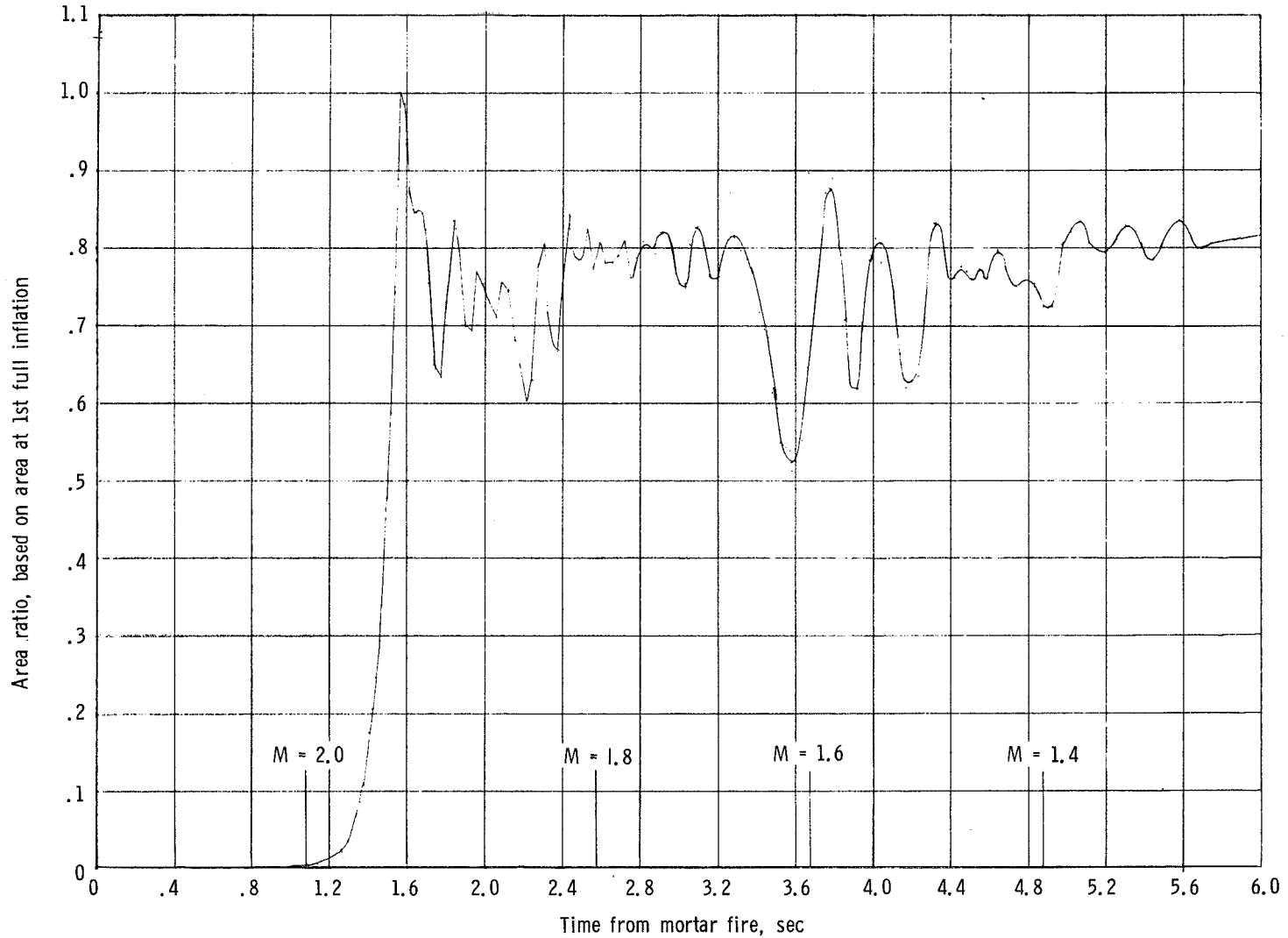
(a) 0 to 6 seconds after mortar fire.

Figure 24.- Variation of parachute area ratio with time from mortar fire (40.423 sec from drop).   AV-4.
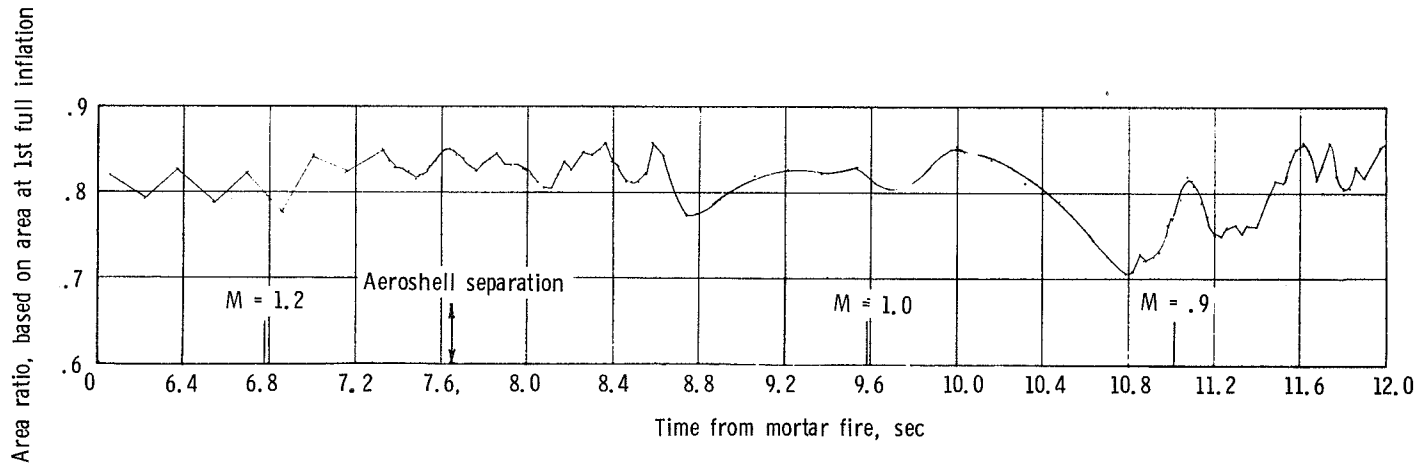
(b) 6 to 12 seconds after mortar fire.
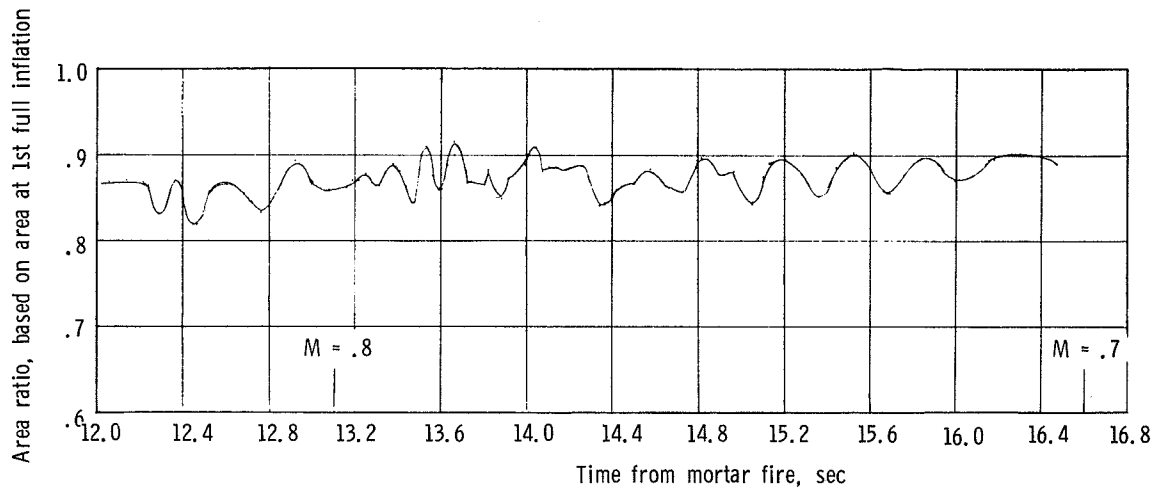
(c) 12 to 16.8 seconds after mortar fire.

Figure 24.- Concluded.
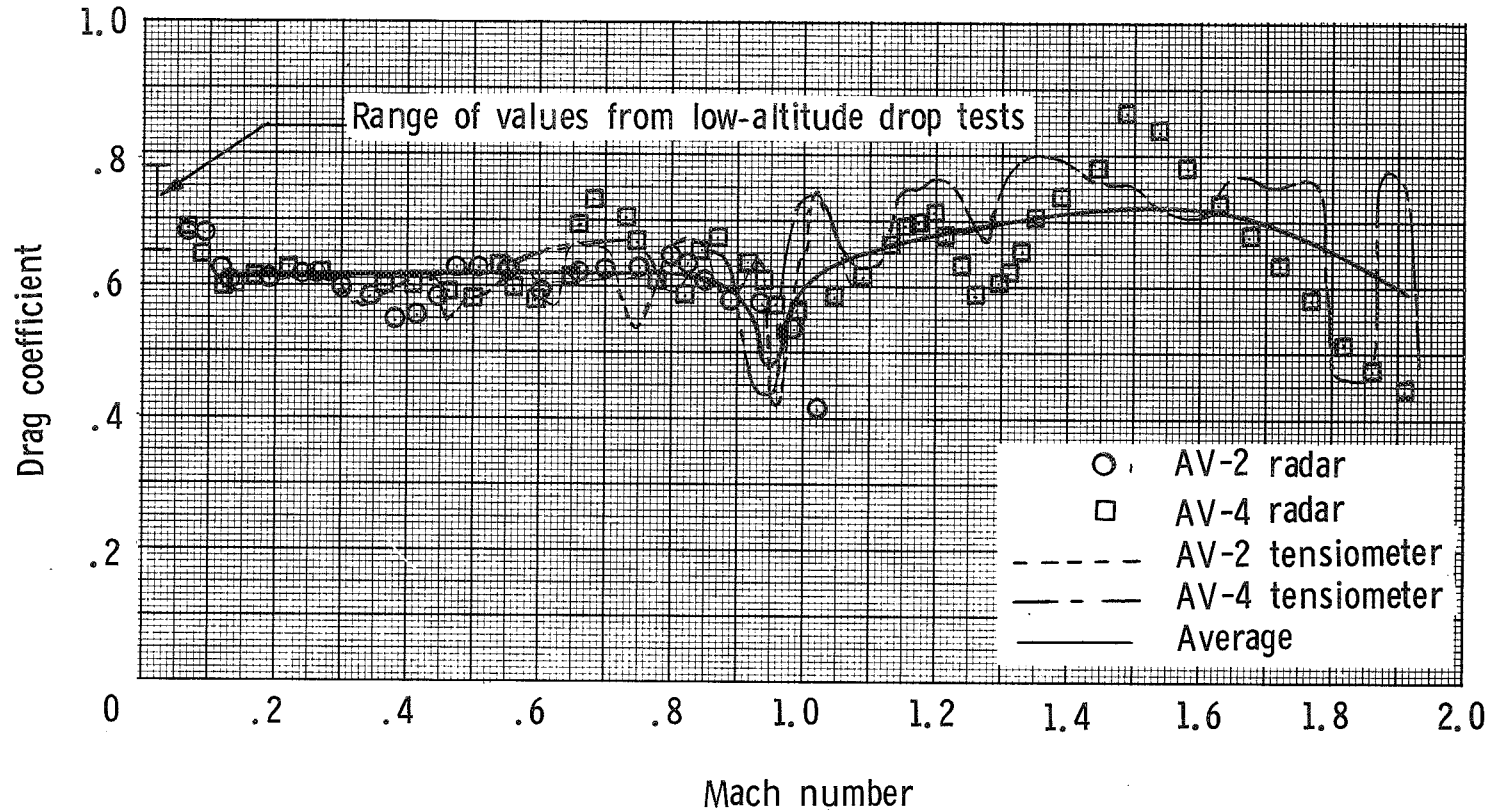
Figure 25.- Variation of parachute drag coefficient with Mach number.
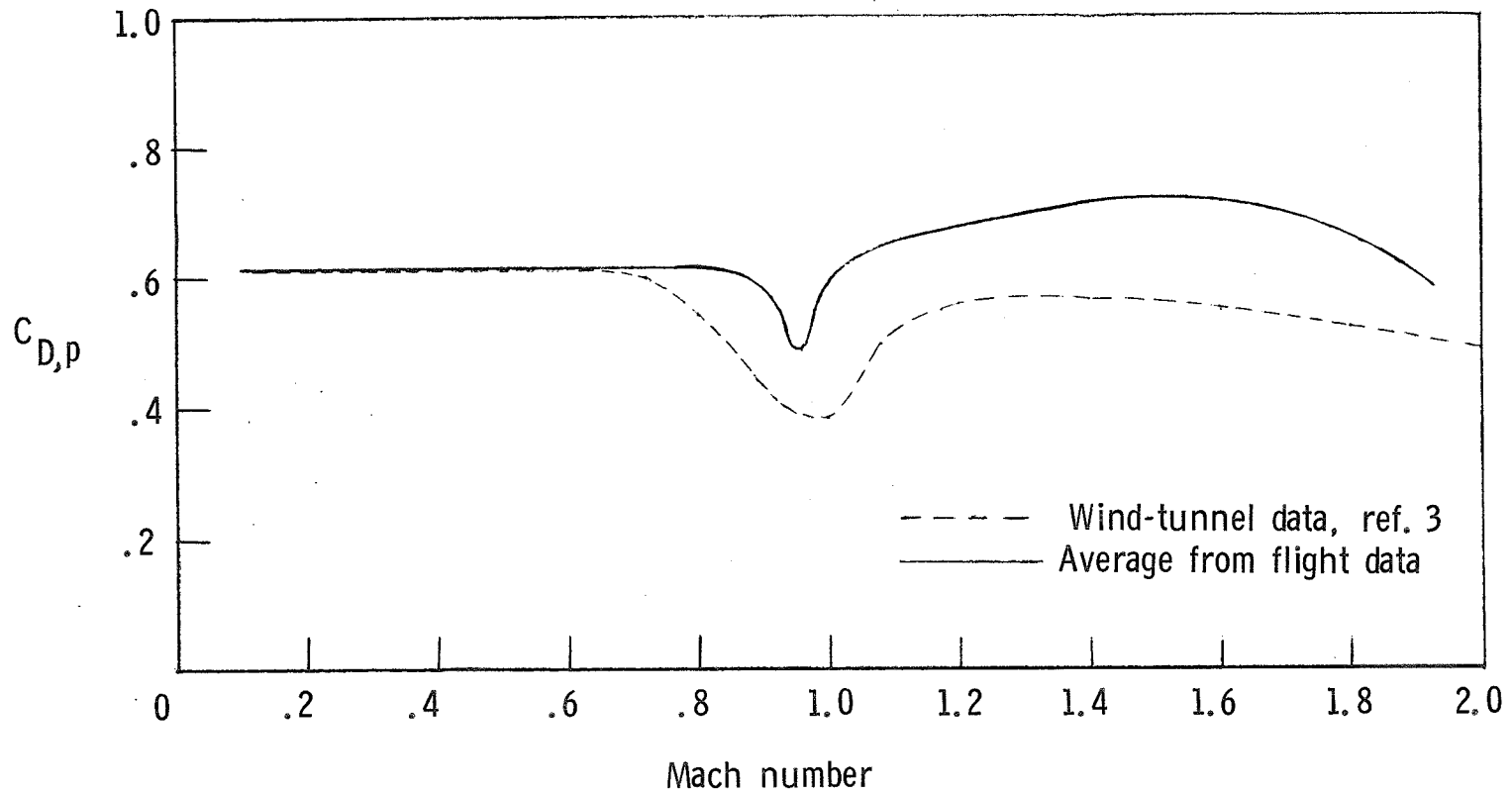
Figure 26.- Comparison between average parachute drag coefficient from flight data and wind-tunnel results.
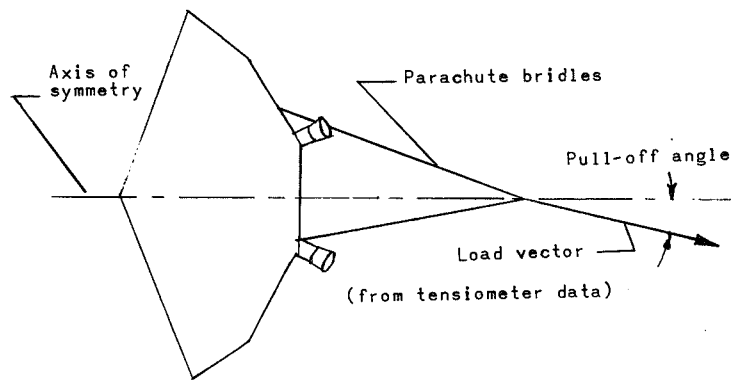
(a) View shown is plane defined by the total load vector
and the test-vehicle longitudinal axis of symmetry.
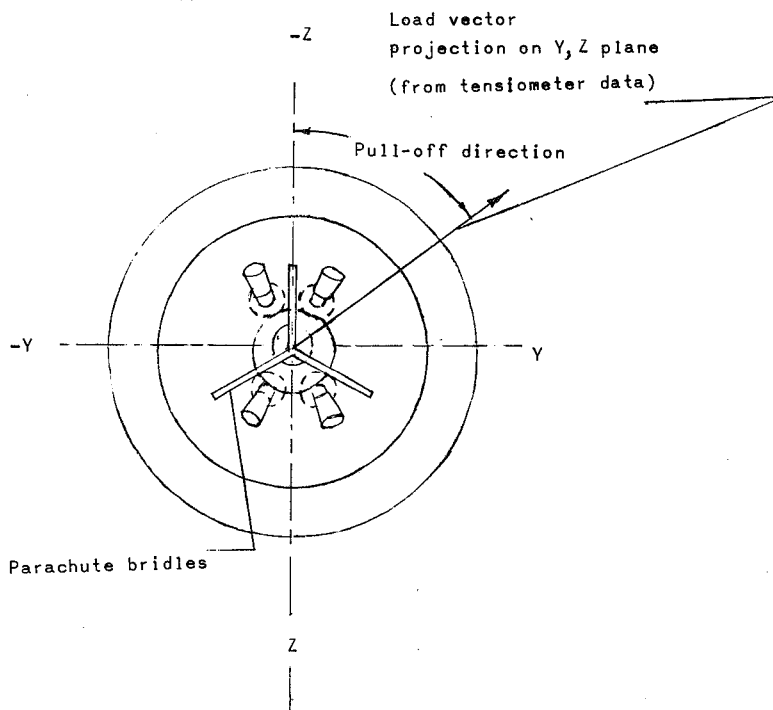
(b) Pull-off direction. View shown in Y,Z plane.

Figure 27.- Arrangement showing "pull-off angle" and "pull-off direction."
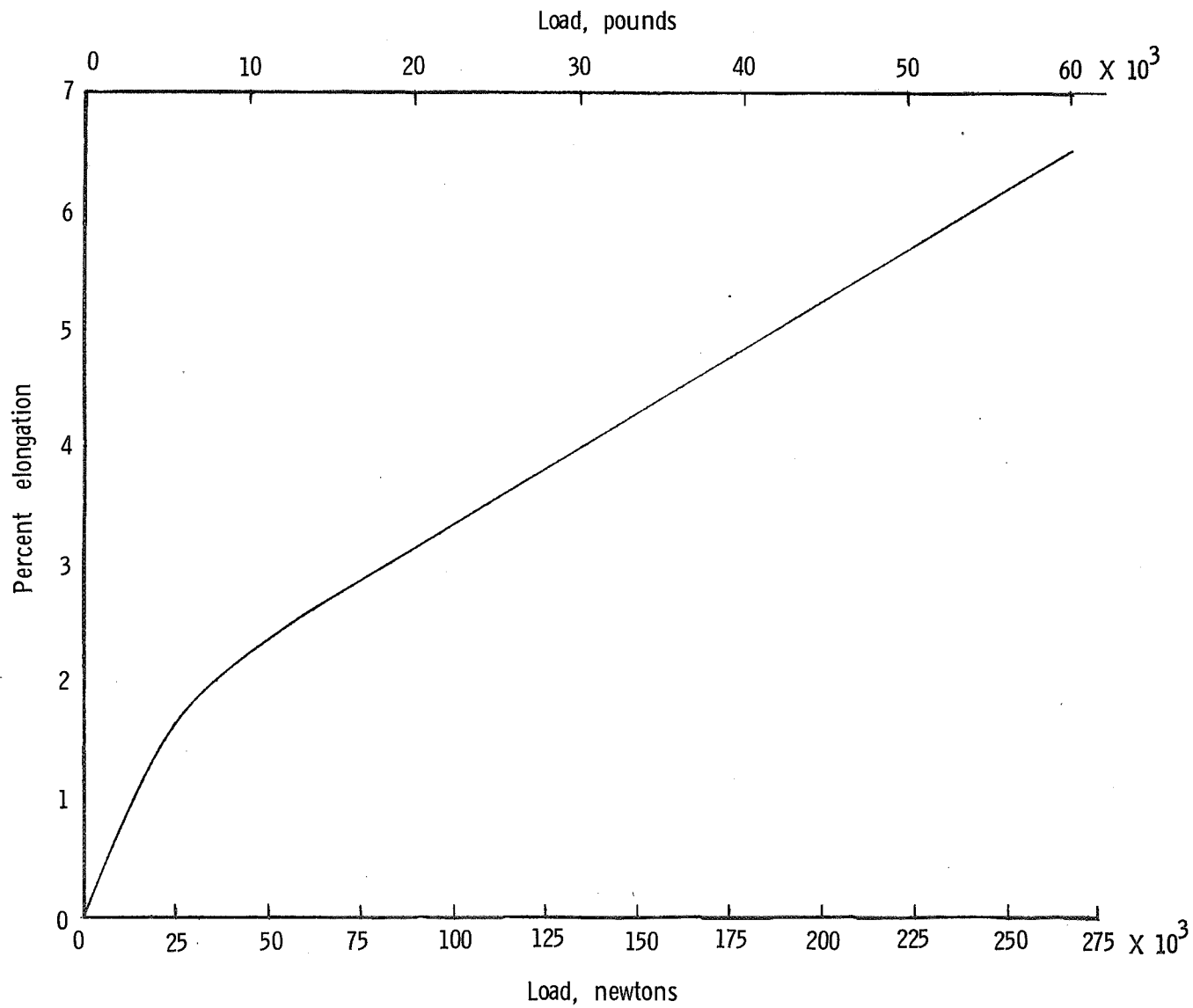
Figure 28.- Elastic properties of parachute bridle material.
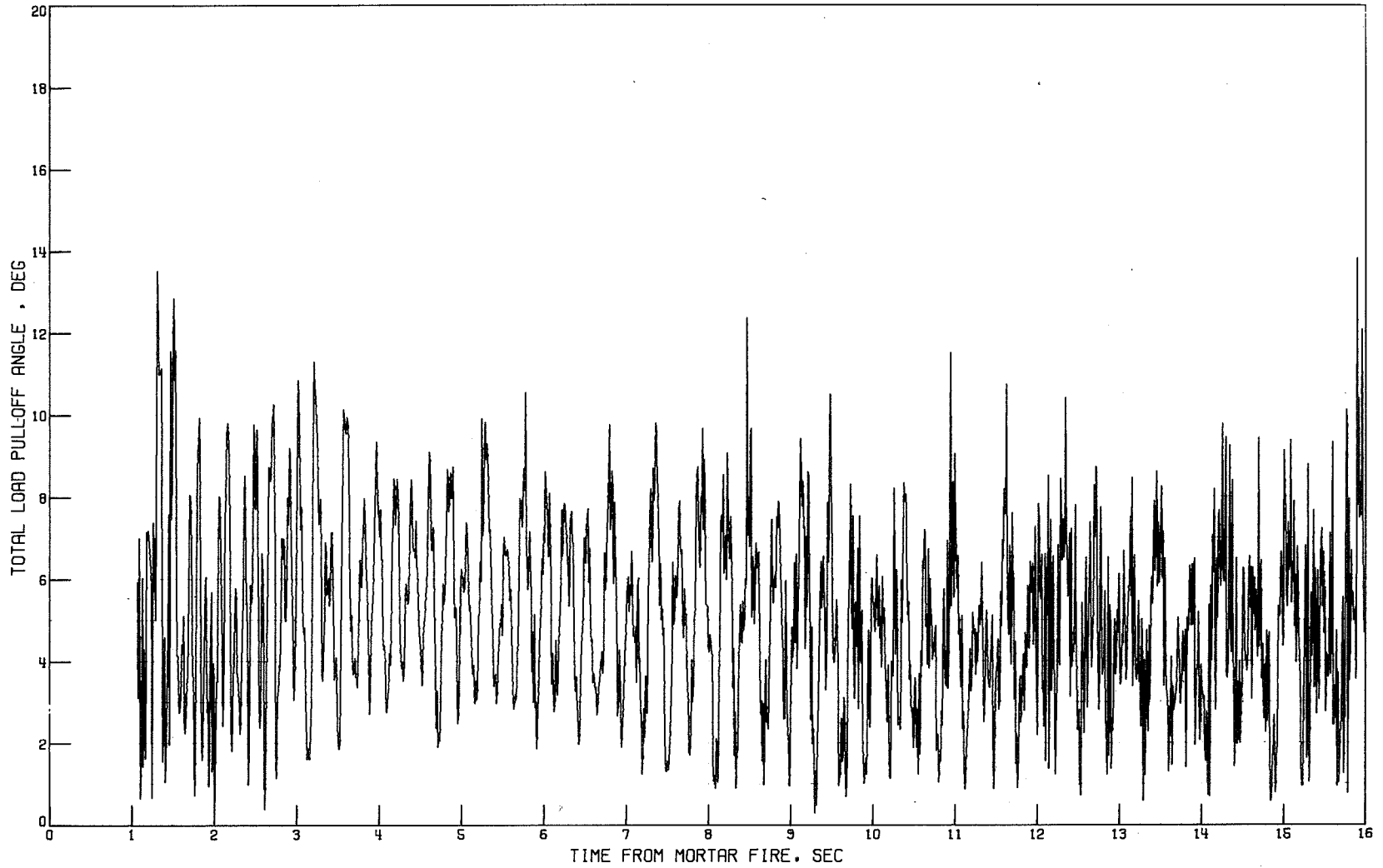
(a) Elastic bridles.

Figure 29.- Variation of total load pull-off angle with time from mortar fire (38.310 sec from drop). AV-1.
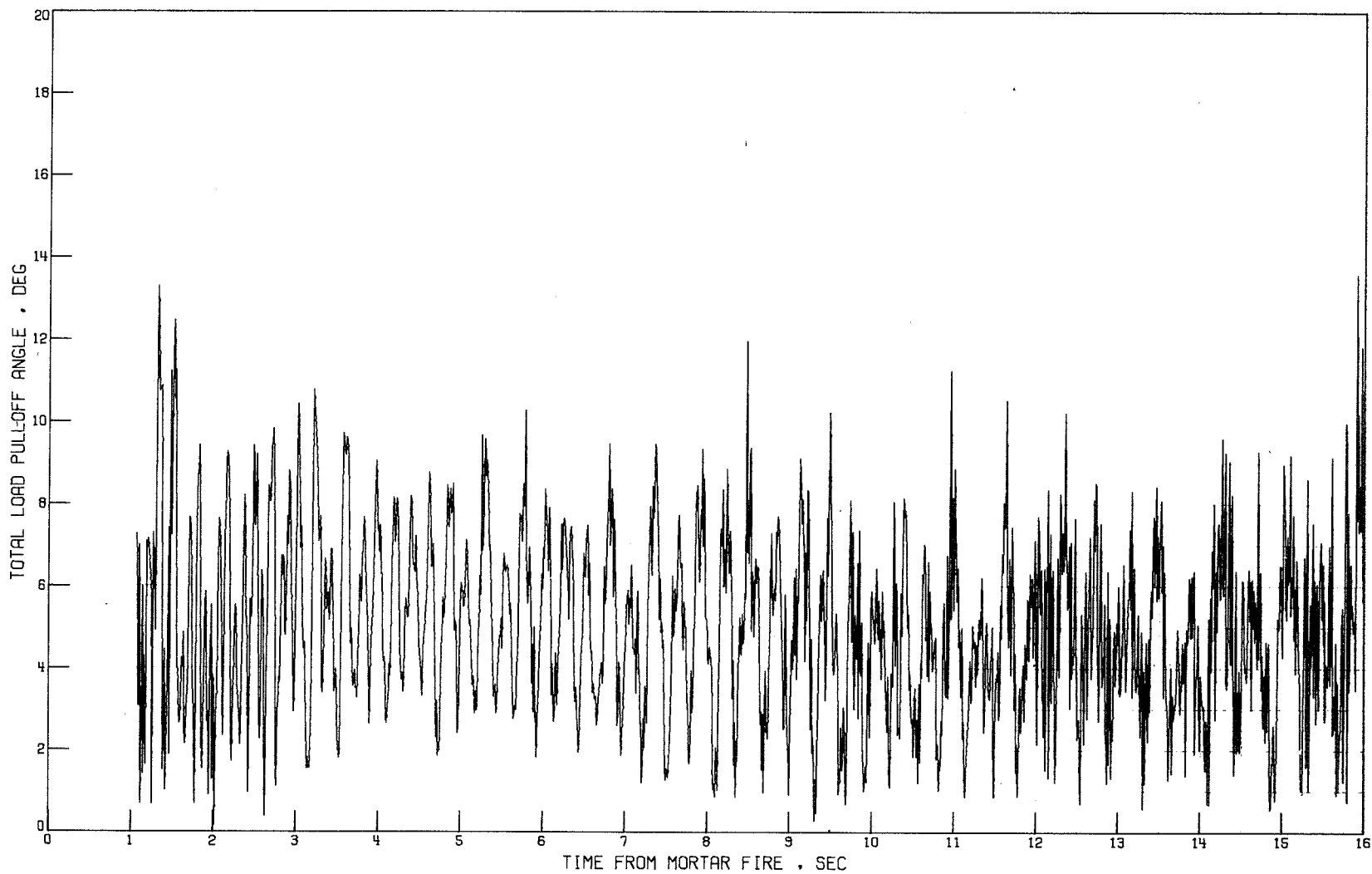
(b) Inelastic bridles.

Figure 29.- Concluded.
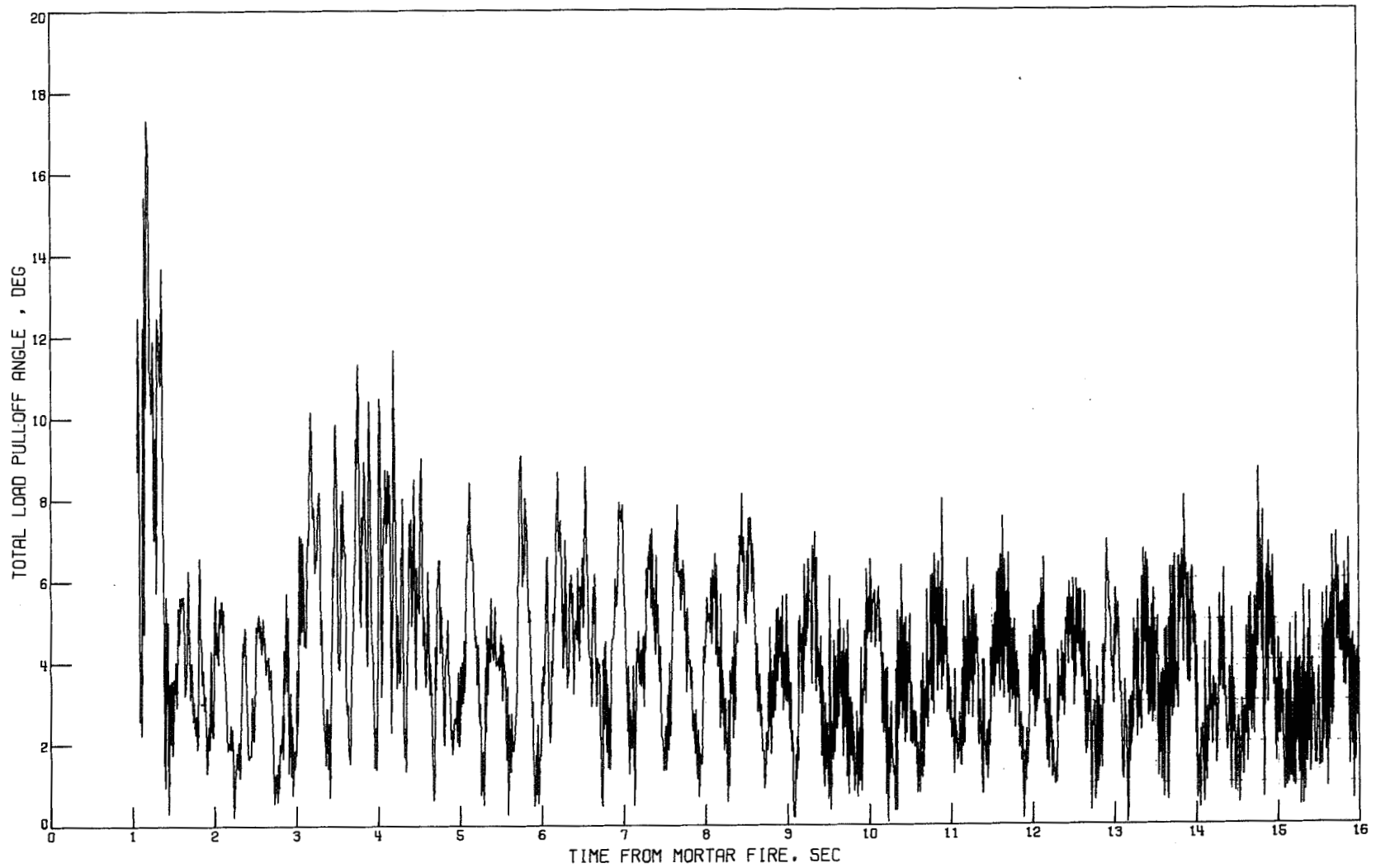
(a) Elastic bridles.

Figure 30.- Variation of total load pull-off angle with time for AV-2.   Flight time at mortar fire, 38.216 sec.
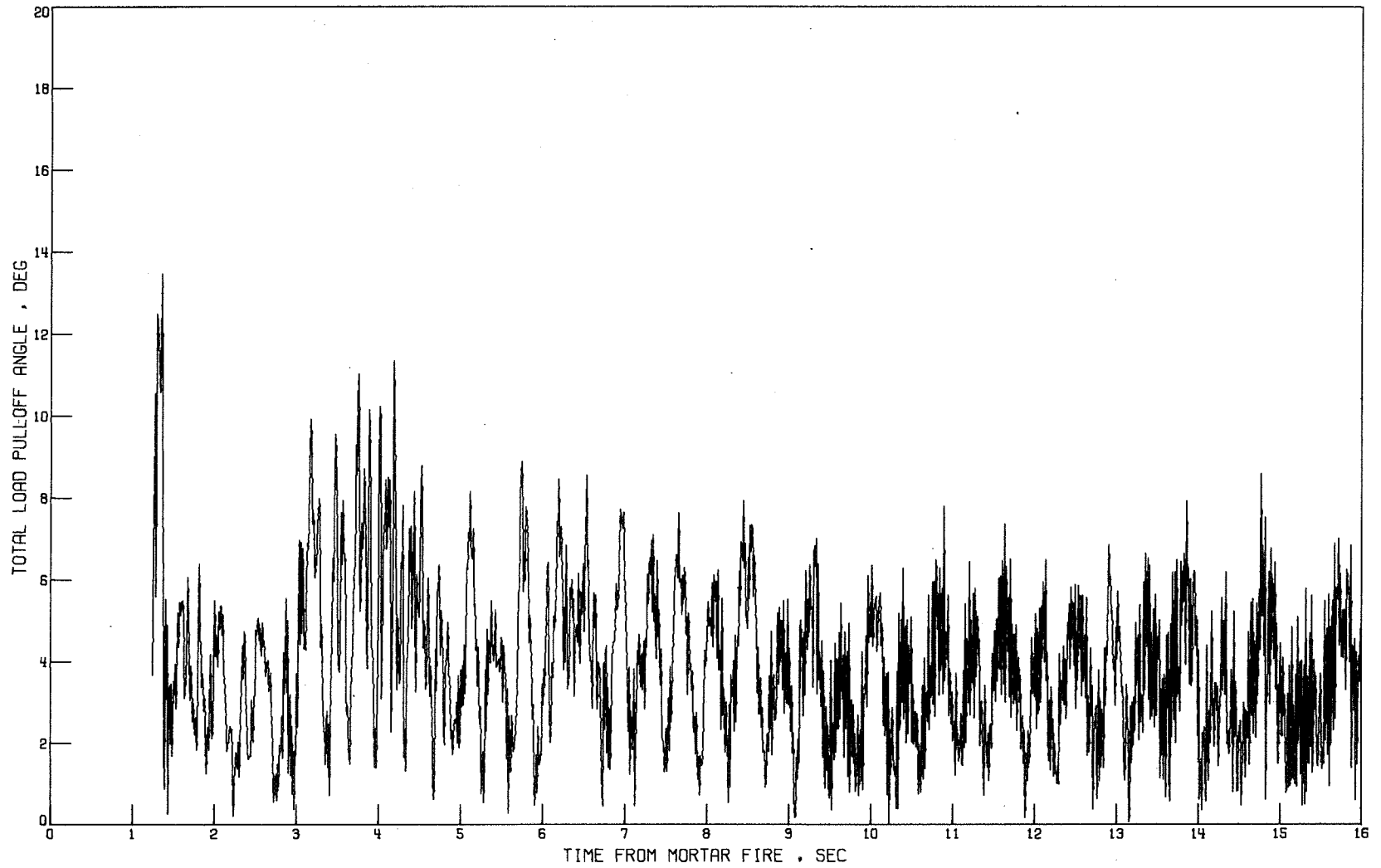
(b) Inelastic bridles.

Figure 30.- Concluded.
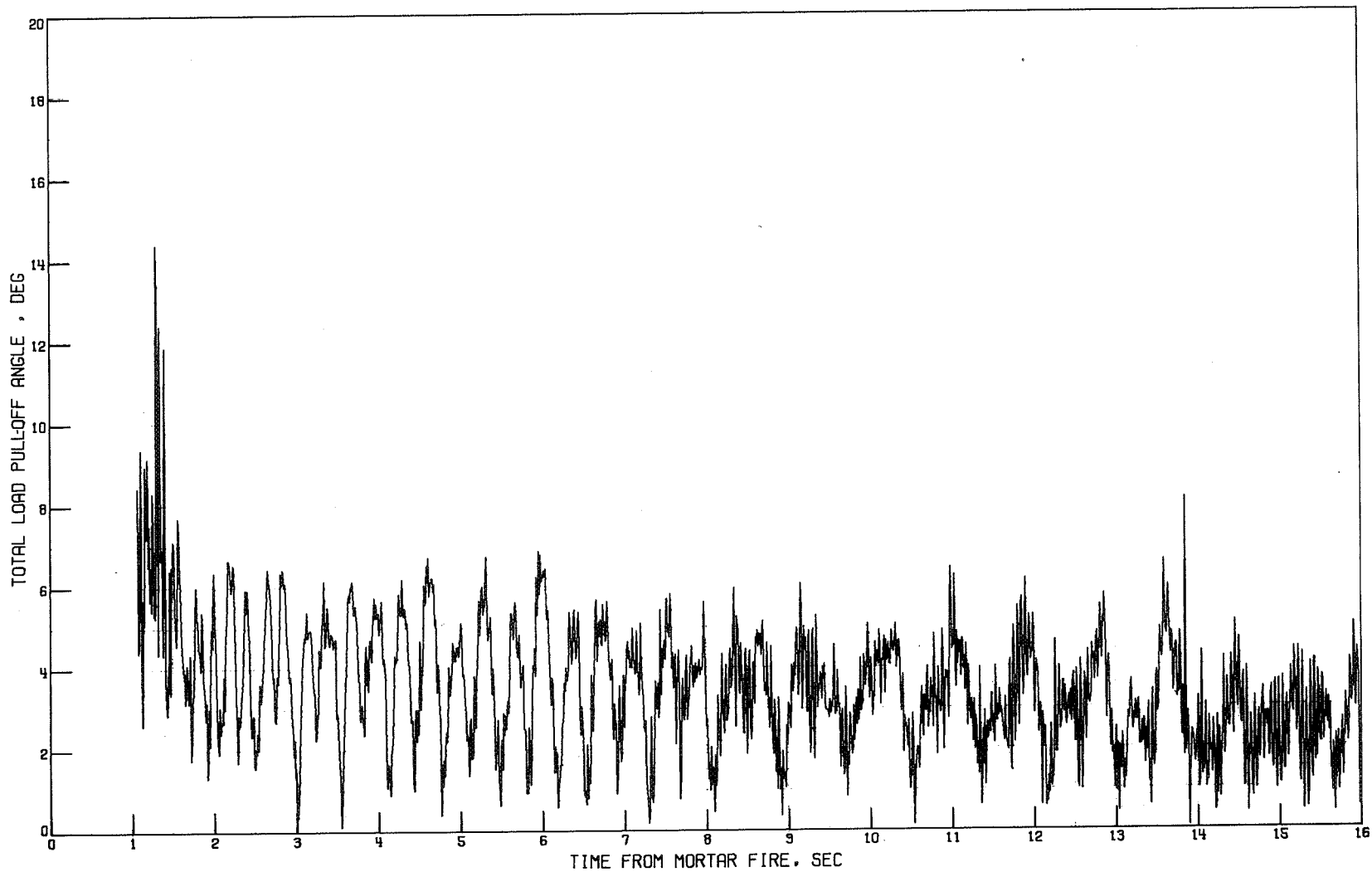
(a) Elastic bridles.

Figure 31.- Variation of total load pull-off angle with time for AV-3.　Flight time at mortar fire, 16.472 sec.
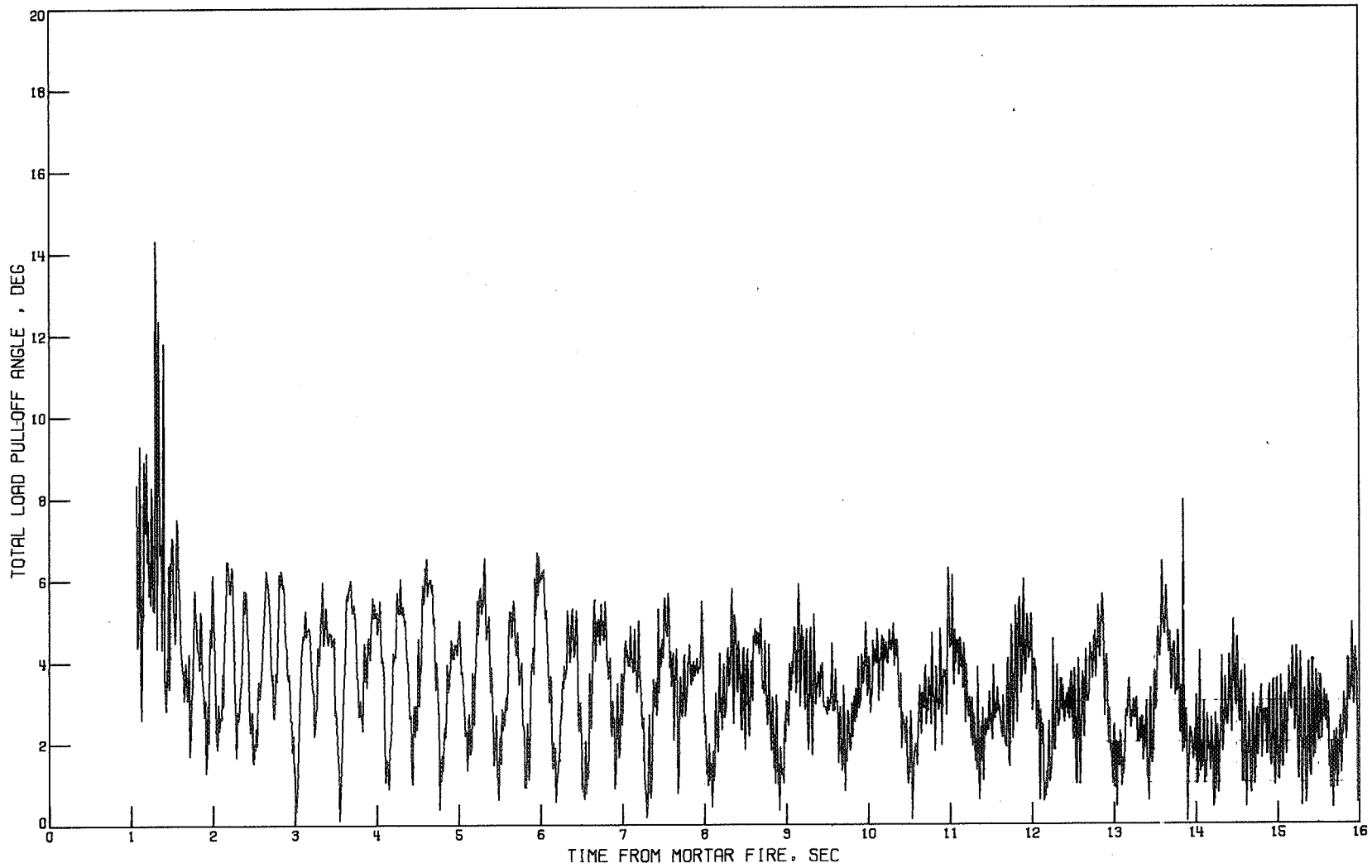
(b) Inelastic bridles.

Figure 31.- Concluded.
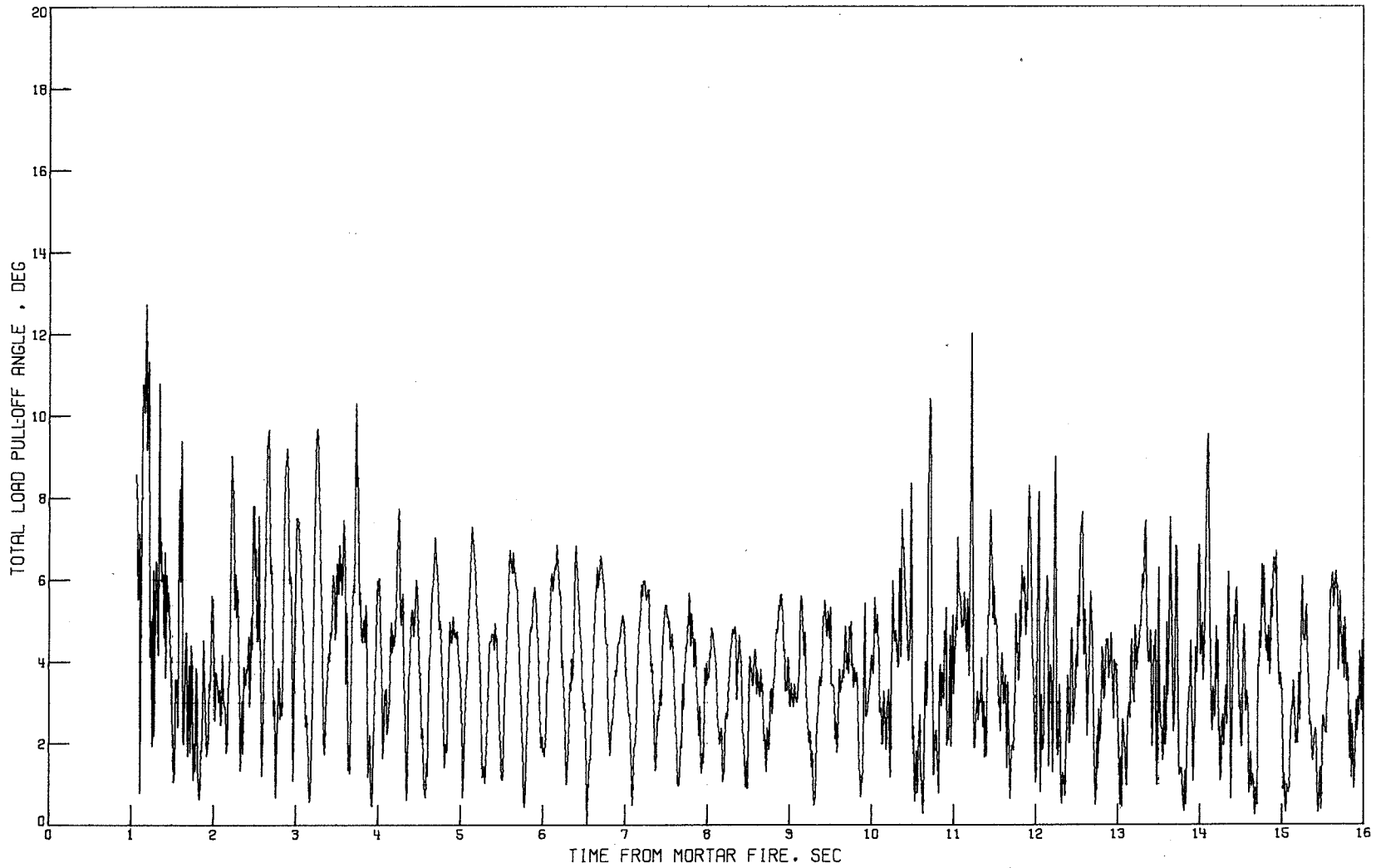
(a) Elastic bridles.

Figure 32.- Variation of total load pull-off angle with time for AV-4.   Flight time at mortar fire, 38.310 sec.
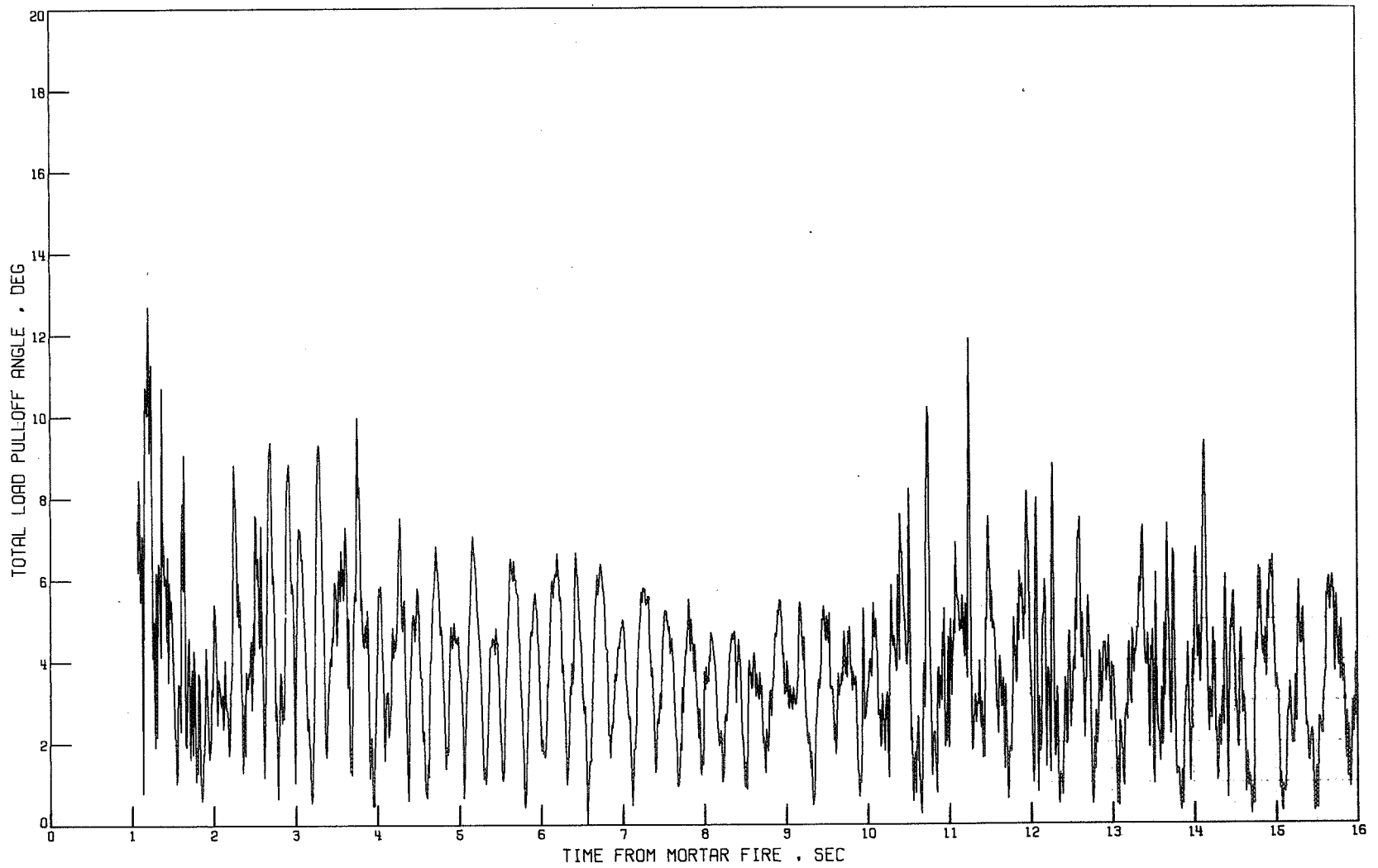
(b) Inelastic bridles.

Figure 32.- Concluded.
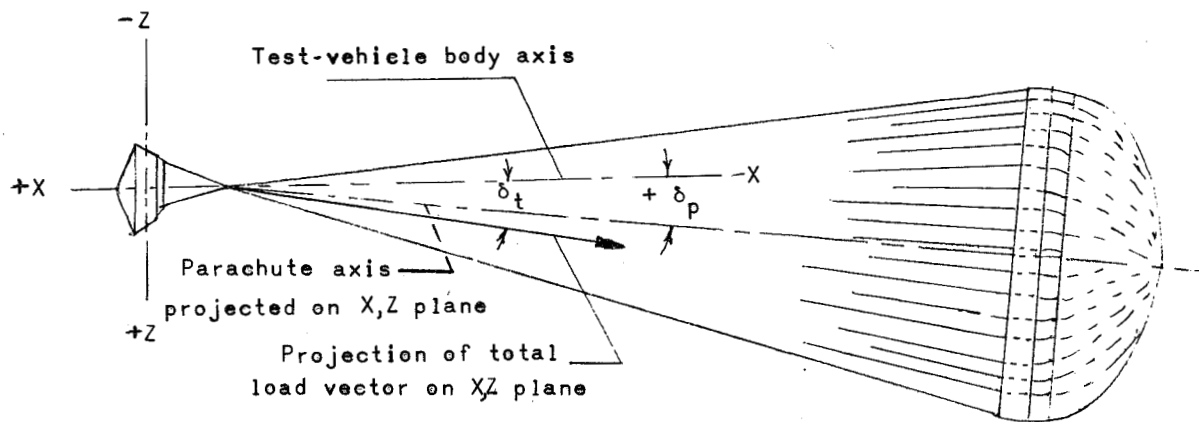
(a) Looking in from left side of parachute.
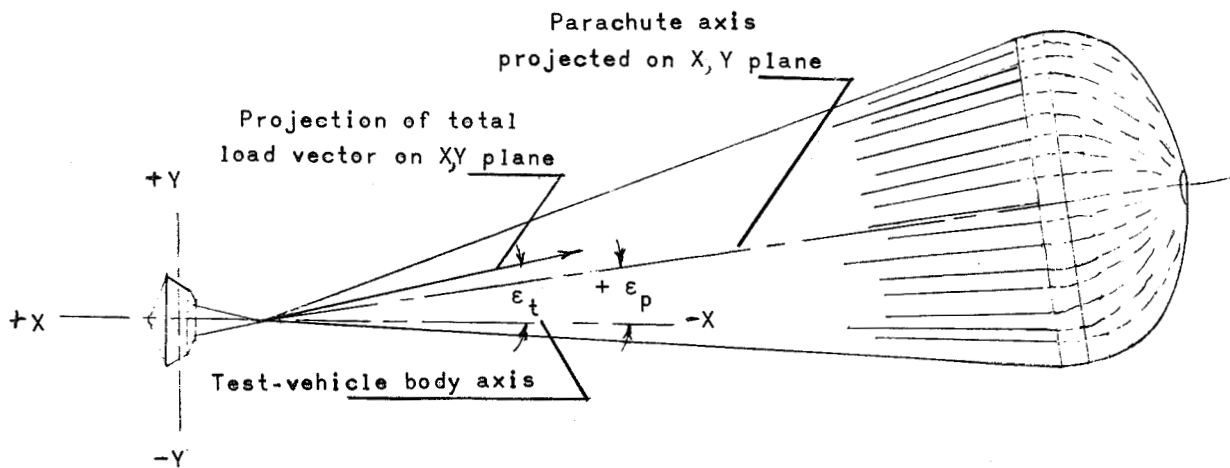
(b) Looking down from top of parachute.

Figure 33.- Sketch showing parachute angles.
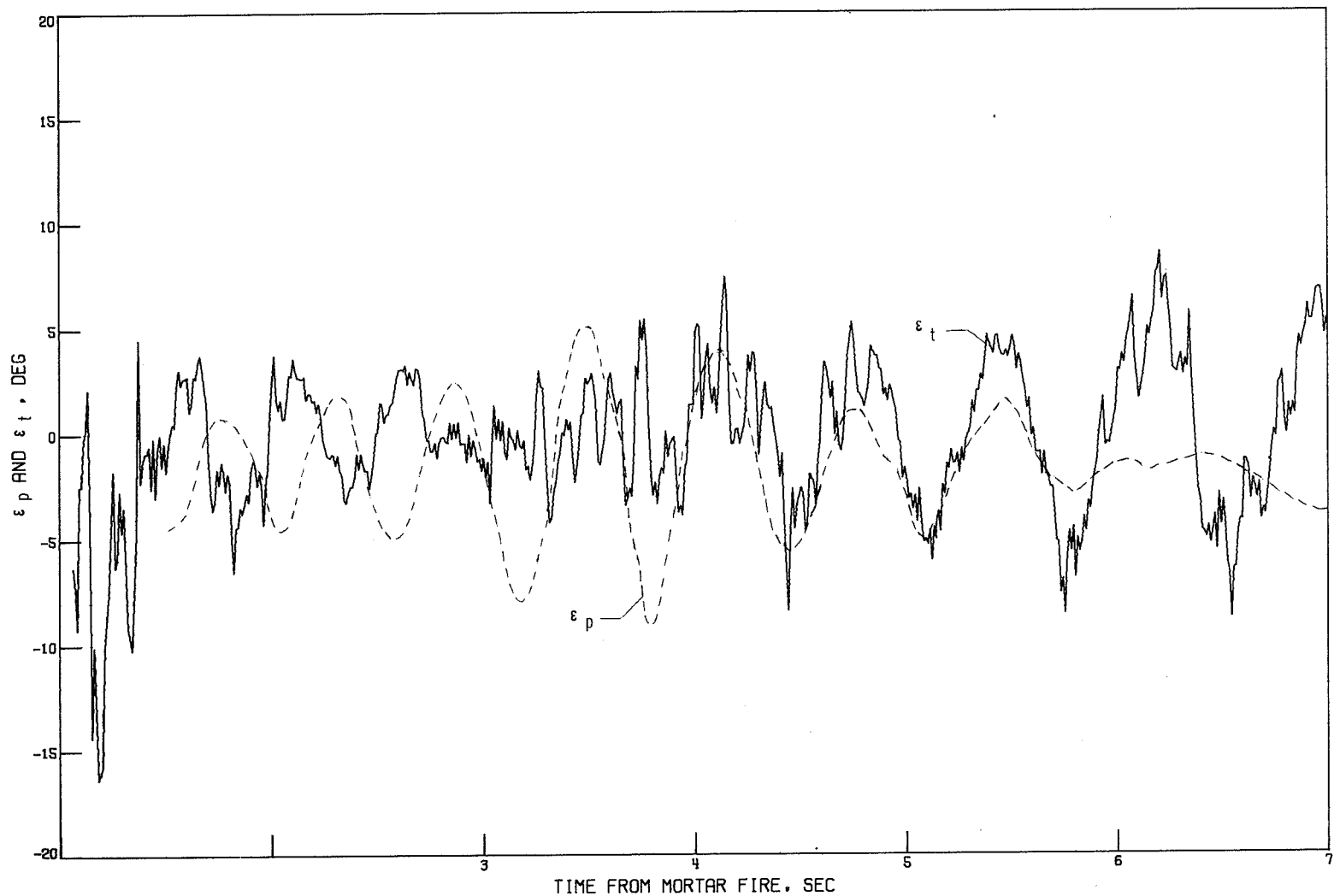
Figure 34.- History of the components in the spacecraft X,Y plane of the total load pull-off angle and the angle between parachute and spacecraft. AV-2; mortar fire, 38.216 sec after drop.
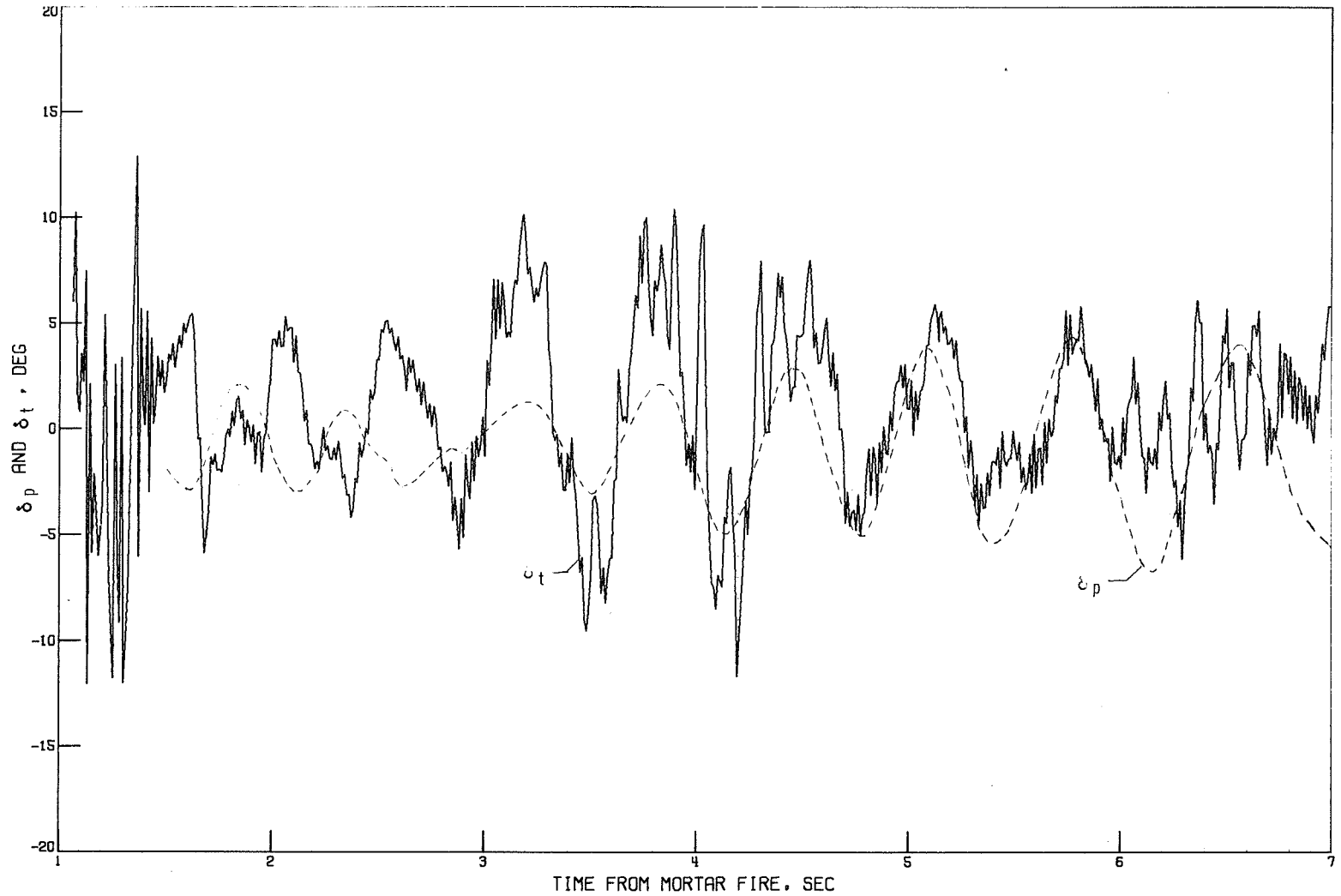
Figure 35.- History of the components in the spacecraft X,Z plane of the total load pull-off angle and the angle between parachute and spacecraft.   AV-2; mortar fire, 38.216 sec after drop.
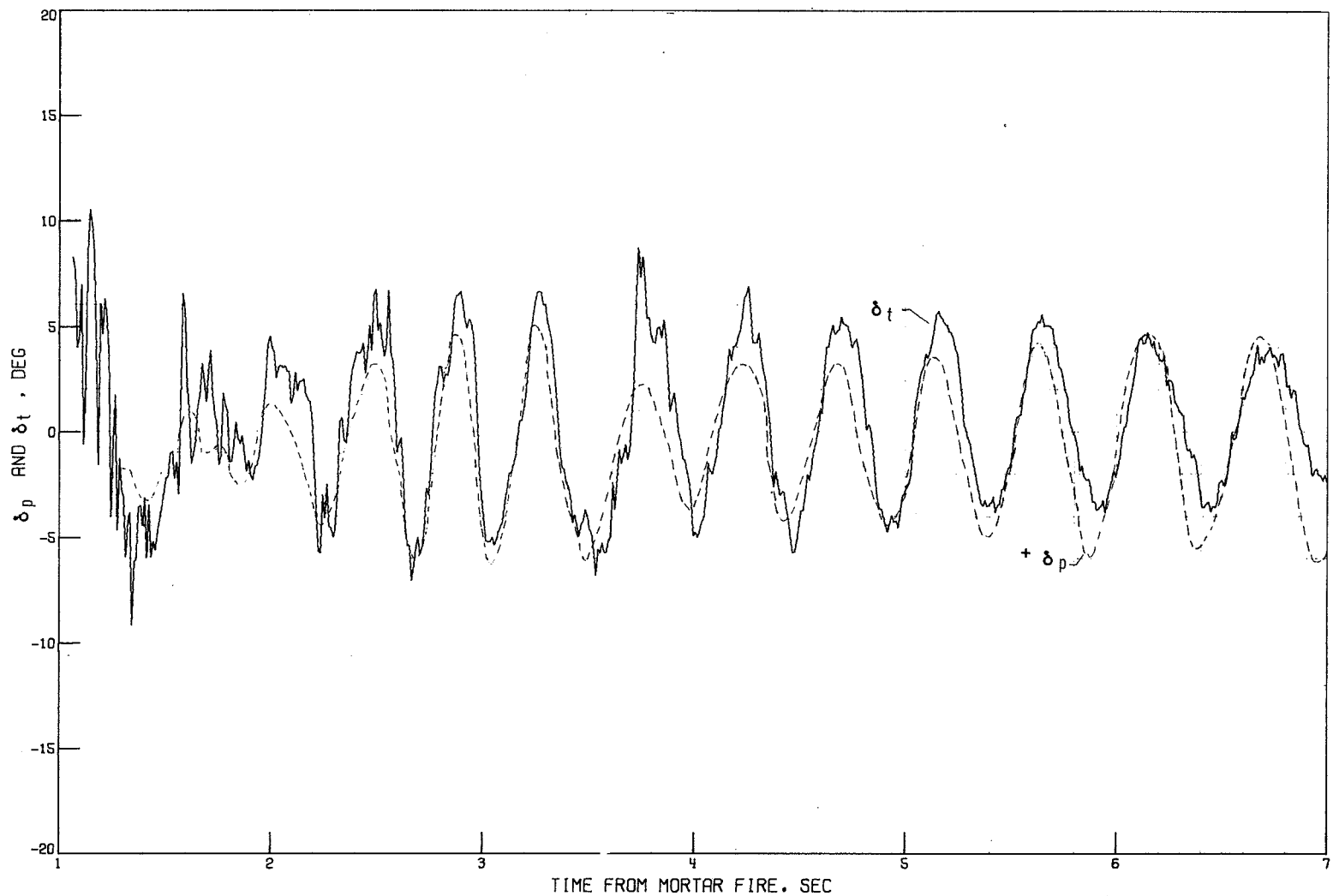
Figure 36.- History of the components in the spacecraft X,Z plane of the total load pull-off angle and the angle between parachute and spacecraft. AV-4; mortar fire, 40.423 sec after drop.
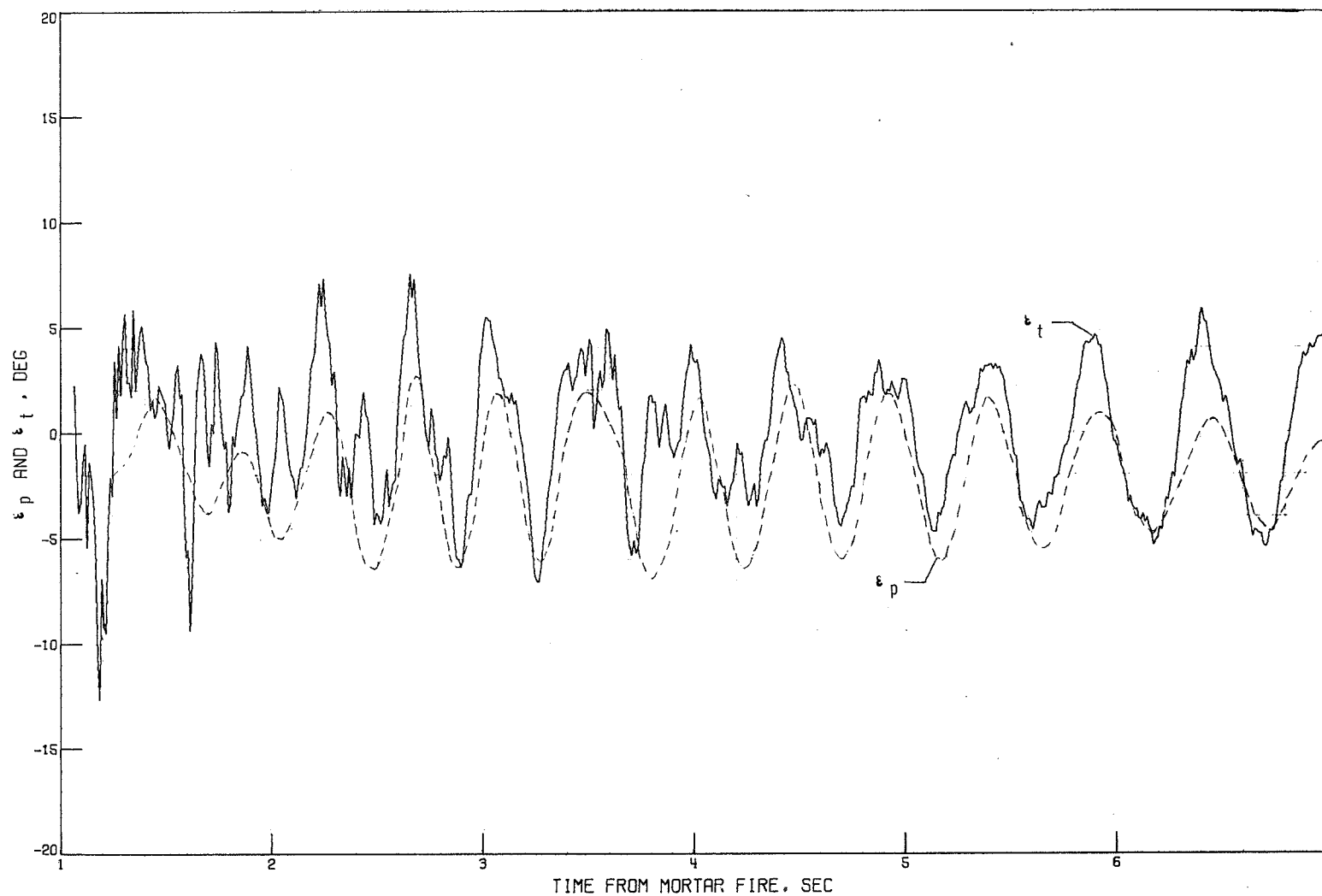
Figure 37.- History of the components in the spacecraft X,Y plane of the total load pull-off angle and the angle between parachute and spacecraft.   AV-4; mortar fire, 40.423 sec after drop.
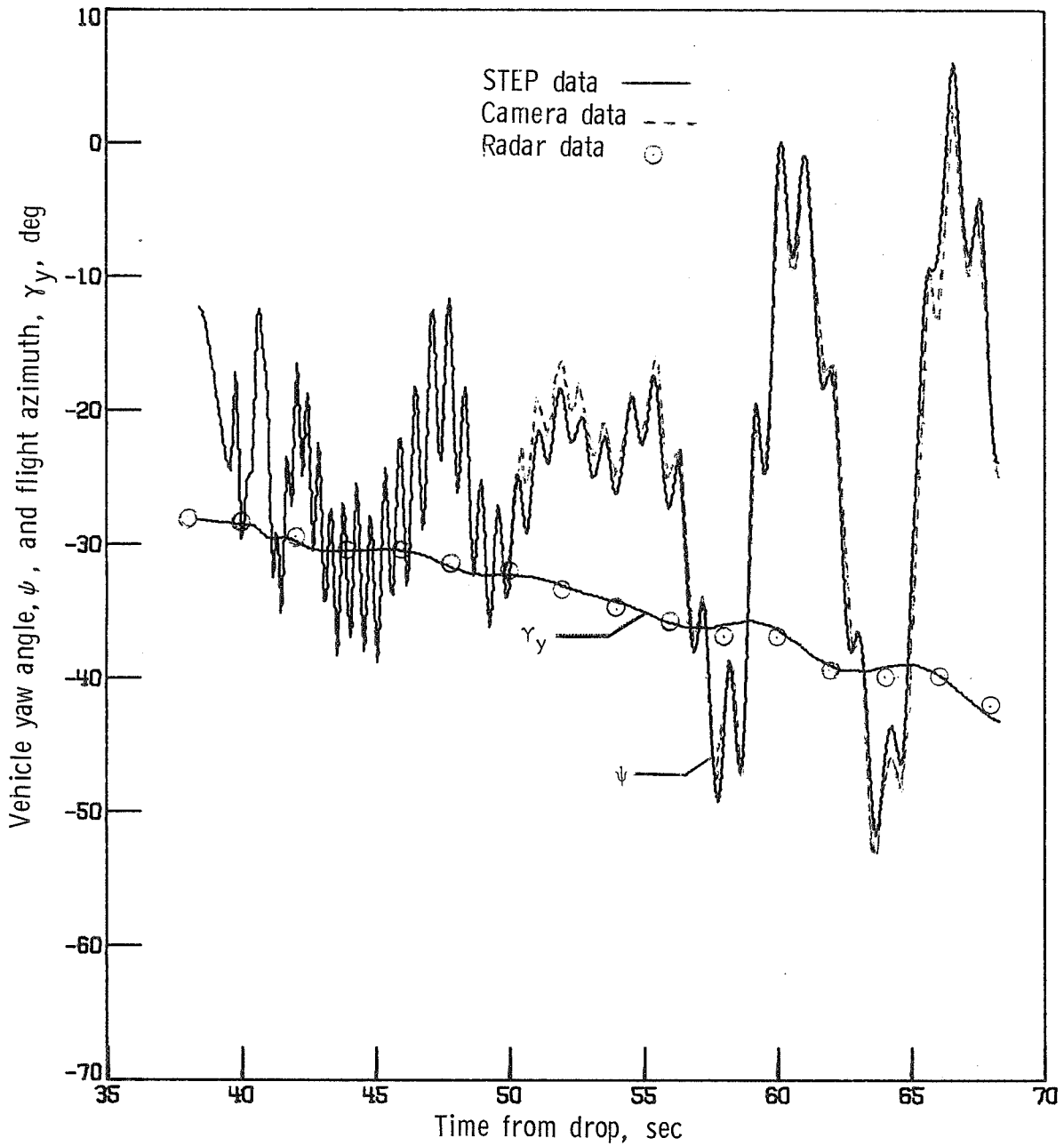
Figure 38.- History of test-vehicle heading ψ and flight azimuth γ_y. AV-1.
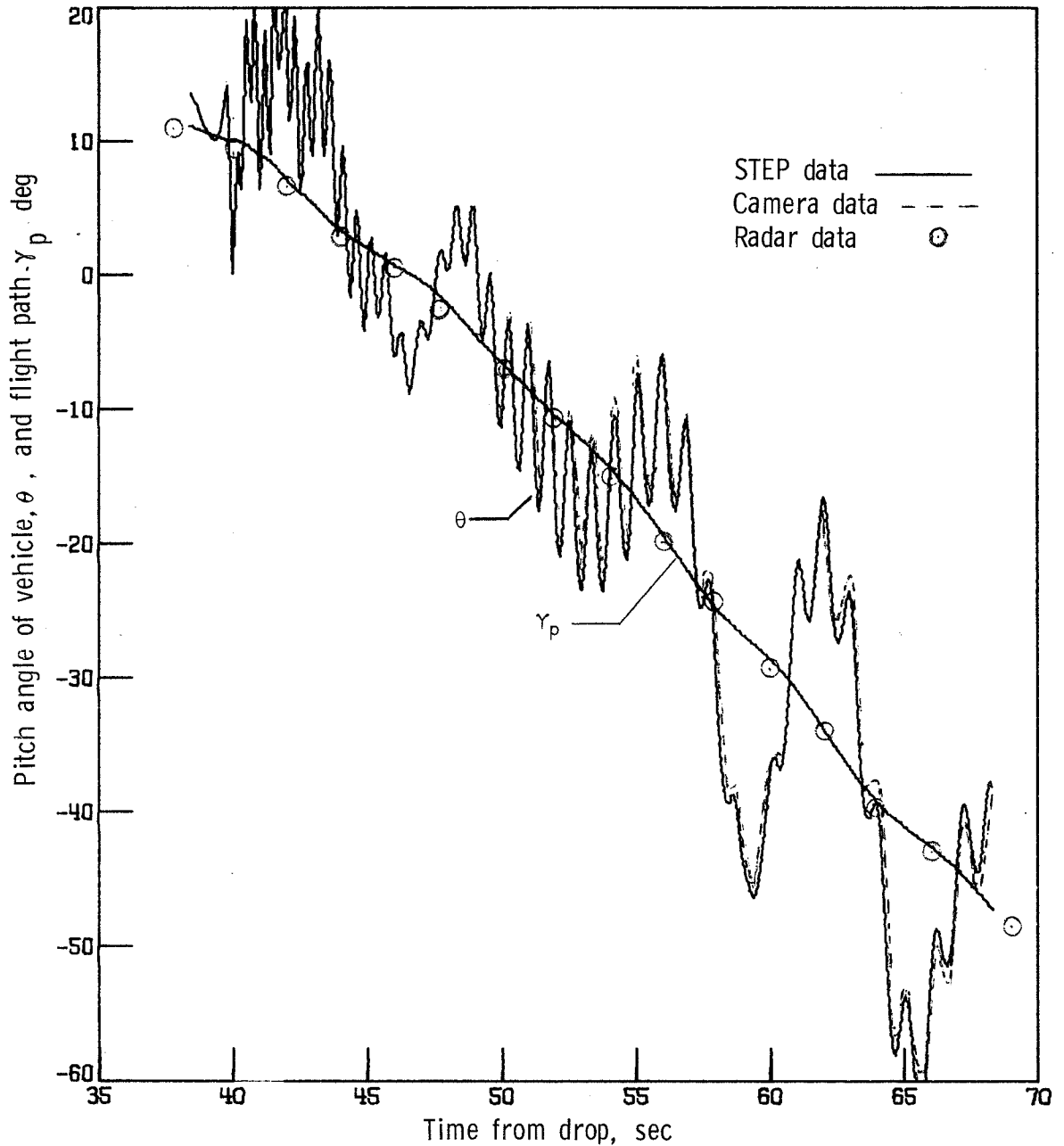
Figure 39.- History of test-vehicle pitch attitude θ and flight-path angle γ_p . AV-1.
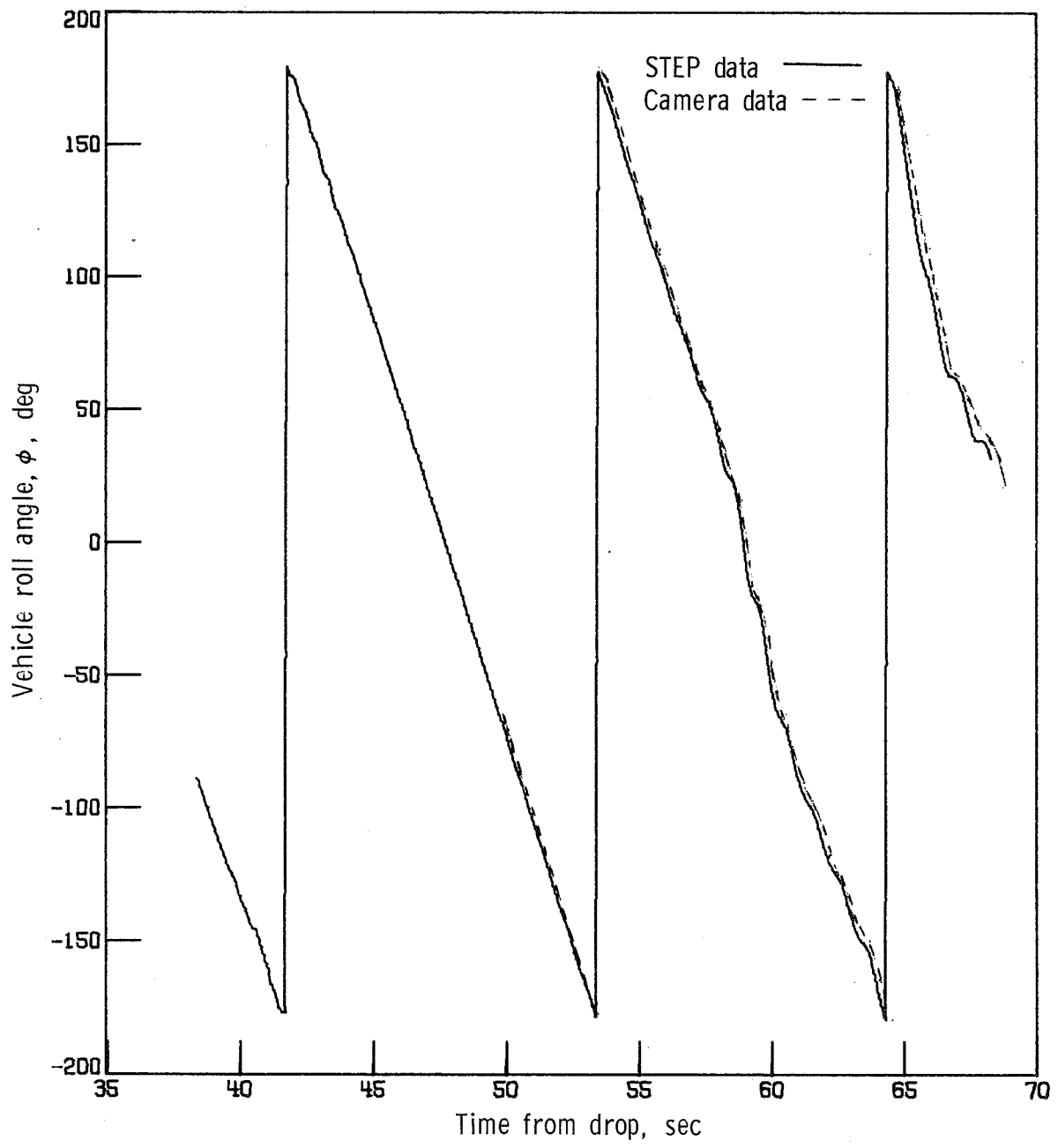
Figure 40.- Test-vehicle roll angle attitude time history.   AV-1.
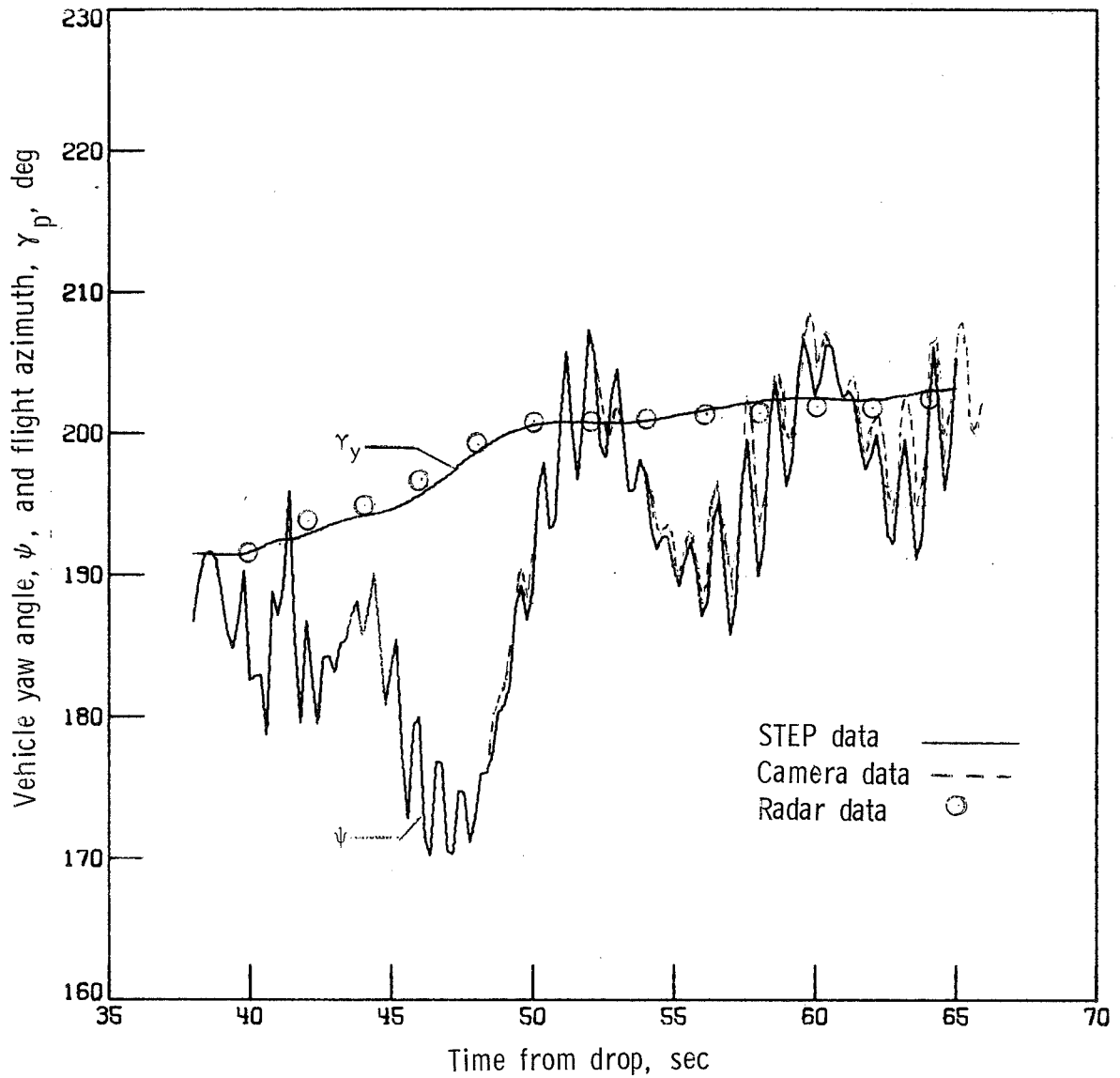
Figure 41.- History of test-vehicle yaw angle ψ and flight azimuth γ_y. AV-2.
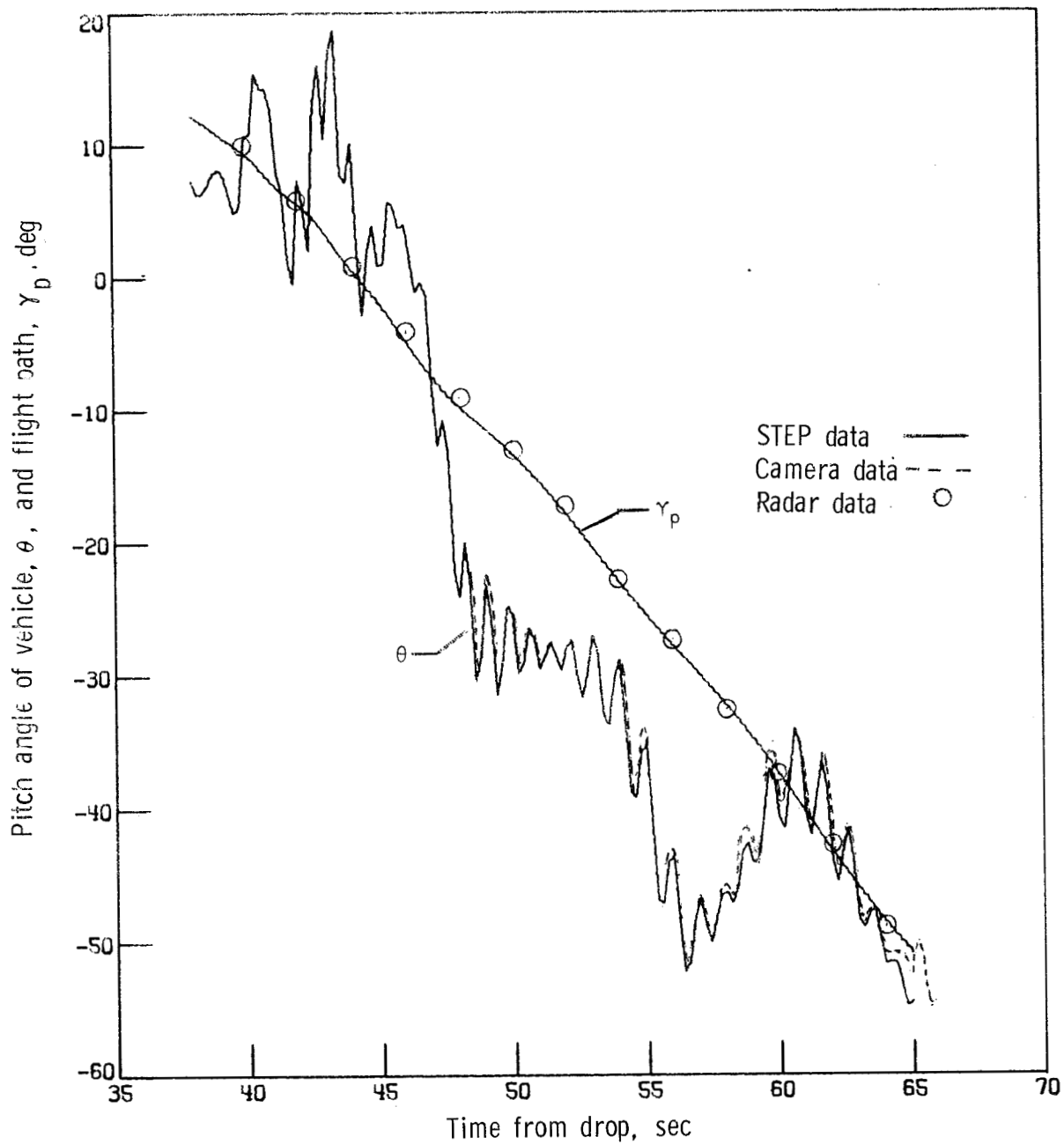
Figure 42.- Time history of test-vehicle pitch attitude θ and flight-path angle γ_p. AV-2.
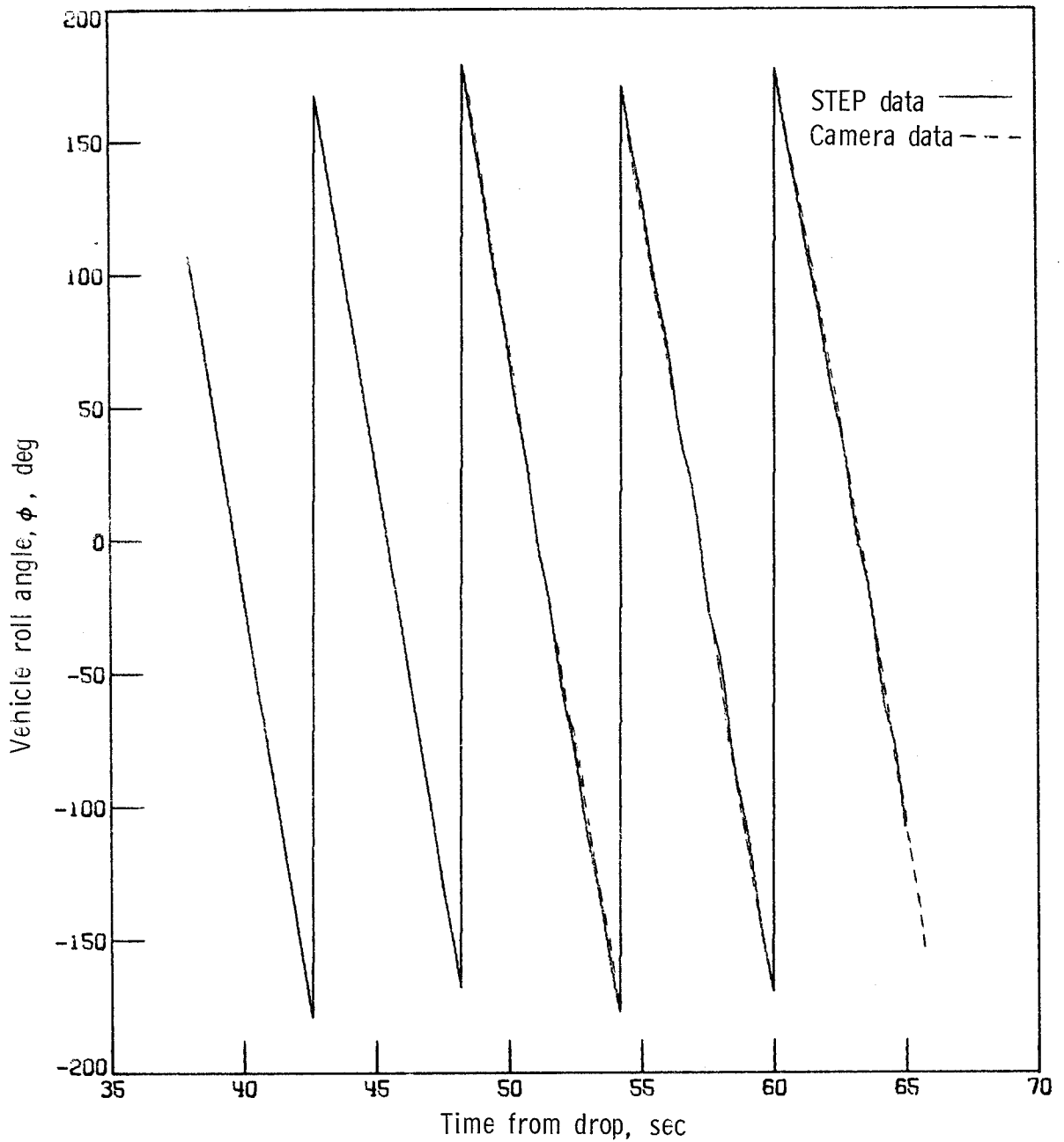
Figure 43.- Test-vehicle roll attitude angle time history. AV-2.
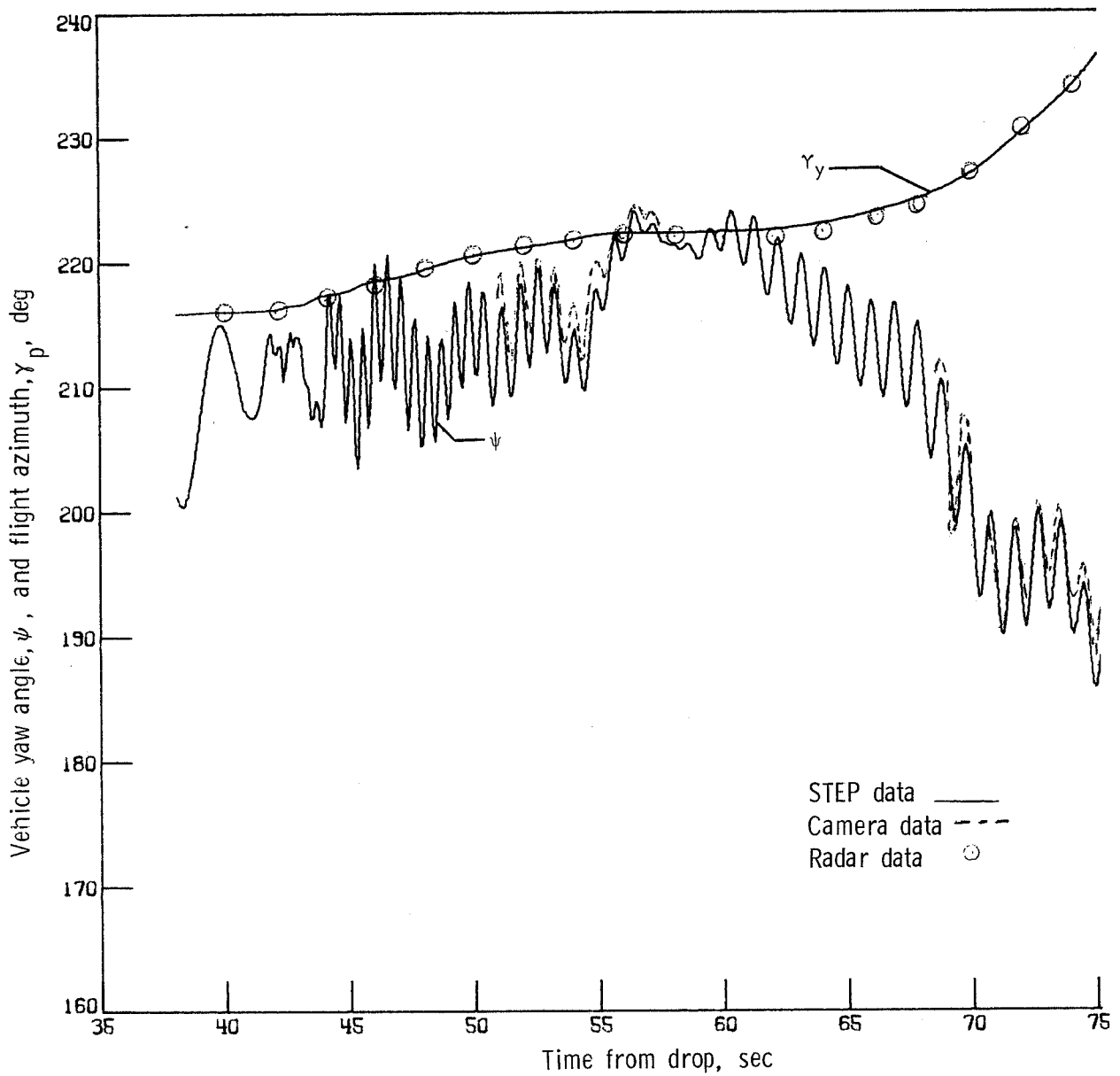
Figure 44.- Time history of test-vehicle yaw angle ψ and flight azimuth γ_y. AV-4.
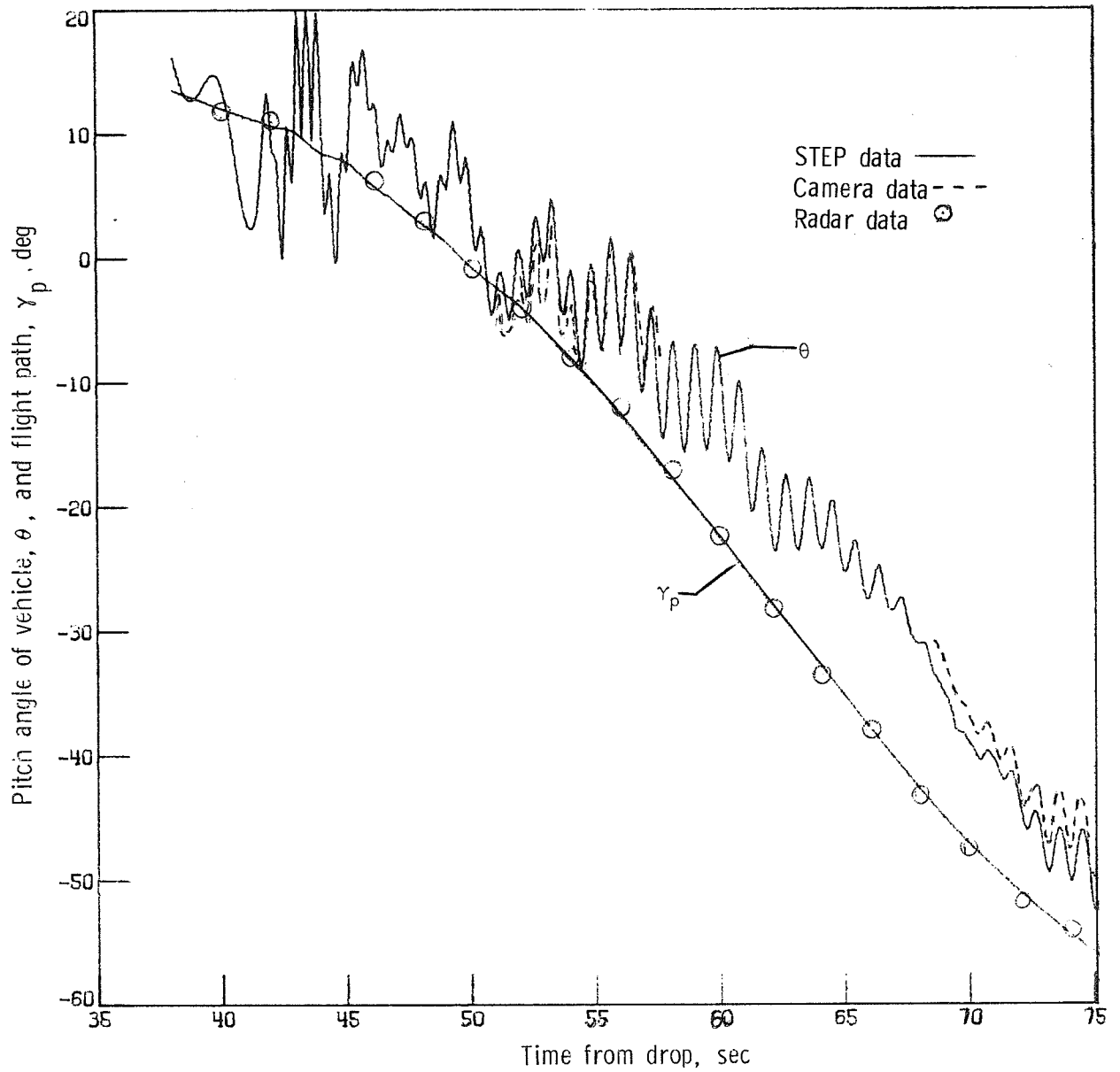
Figure 45.- Time history of test-vehicle pitch attitude angle θ and flight-path angle γ_p. AV-4.
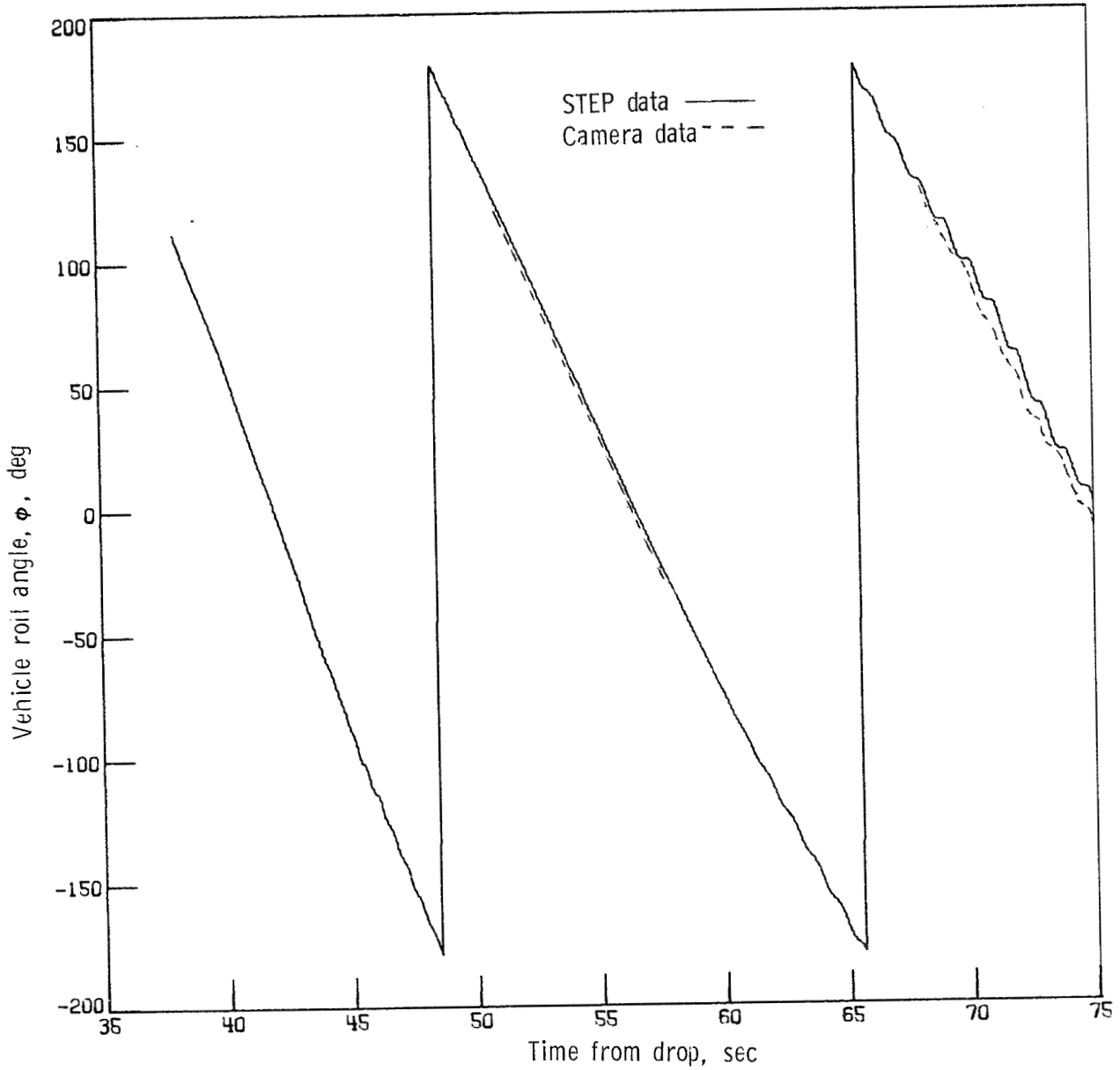
Figure 46.- Test-vehicle roll attitude angle time history.   AV-4.
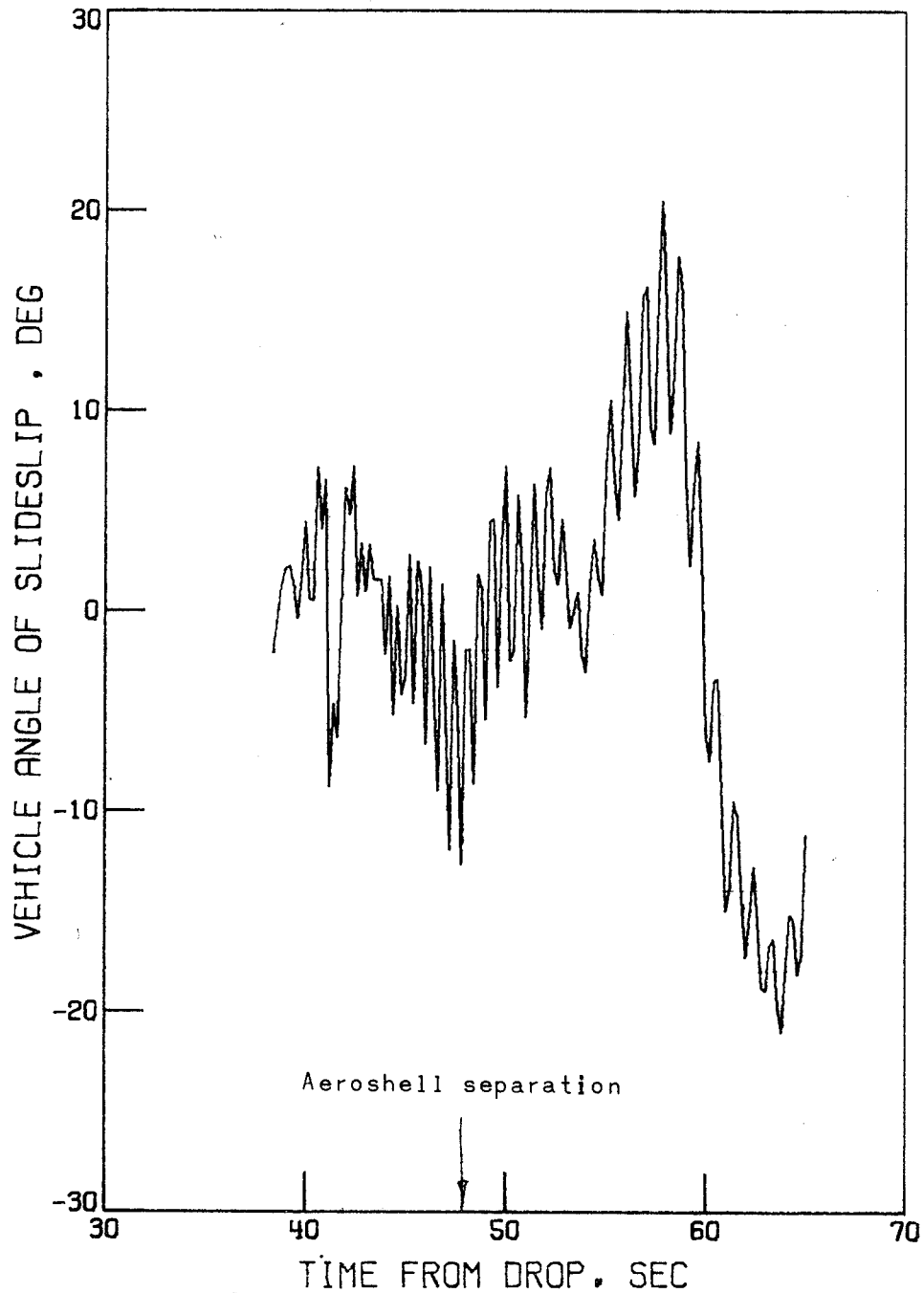
Figure 47.- History of vehicle angle of sideslip obtained from trajectory reconstruction. AV-1.
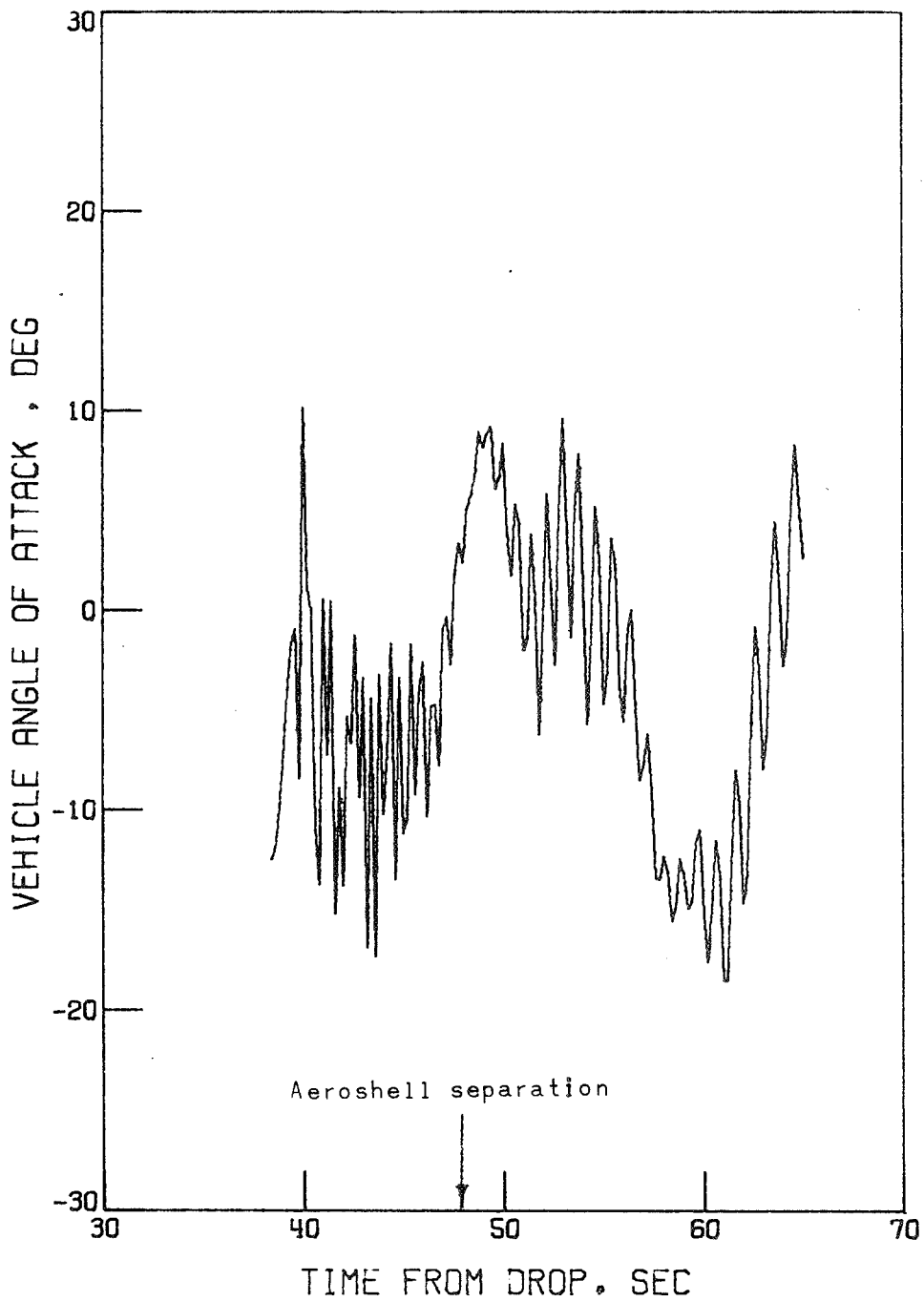
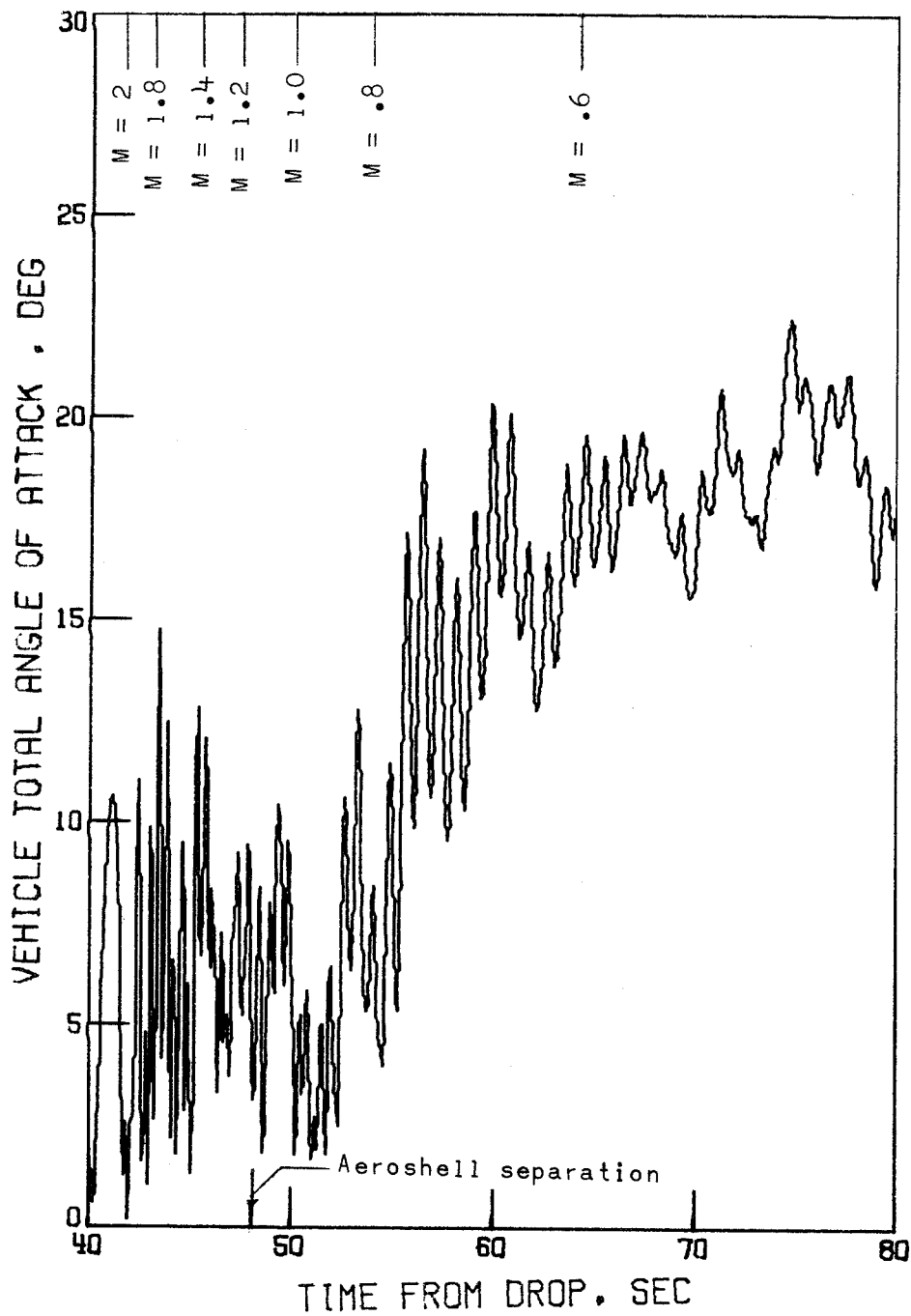Figure 48.- History of vehicle angle of attack obtained from trajectory reconstruction.
AV-1.
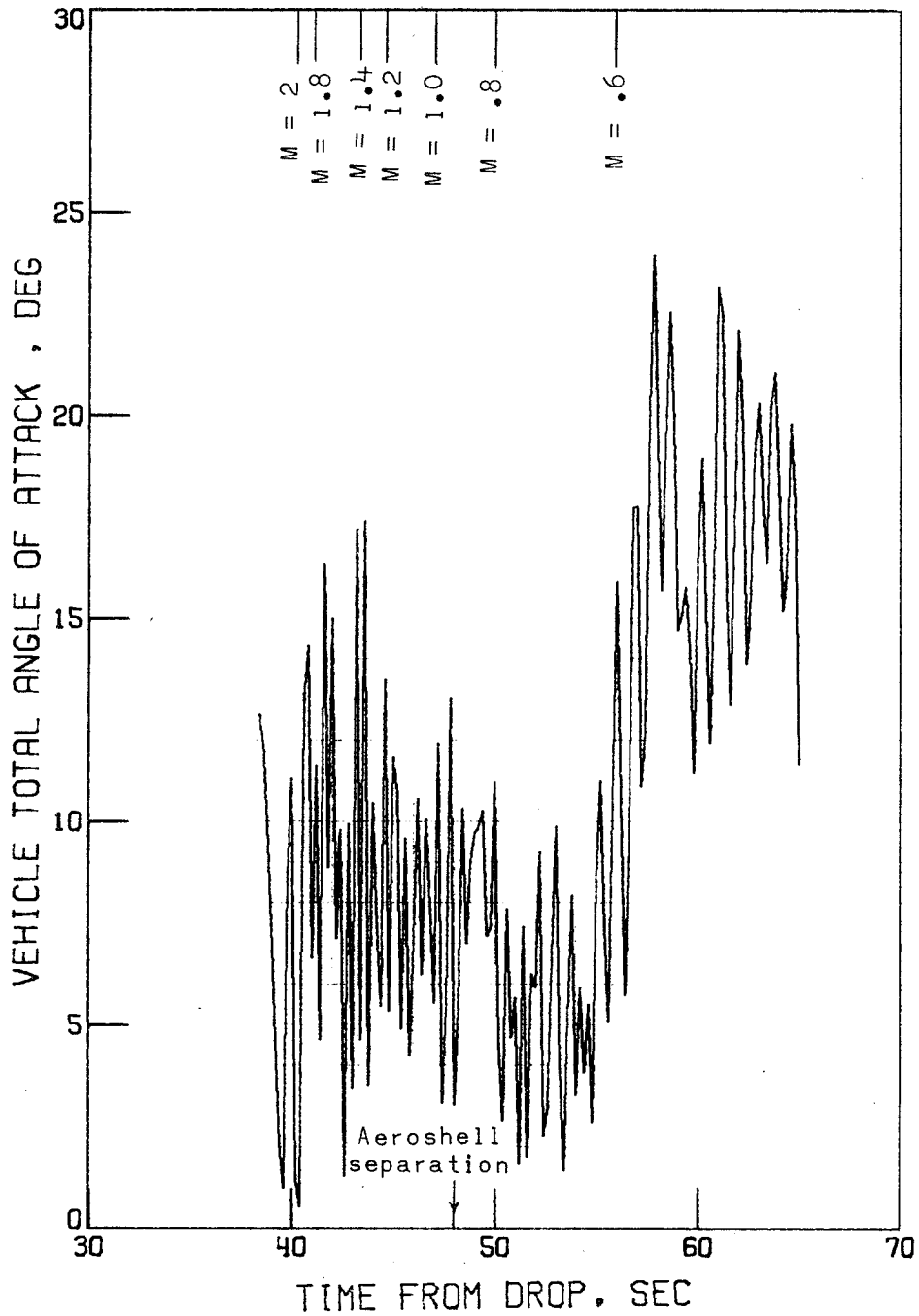
Figure 49.- History of vehicle total angle of attack obtained from trajectory reconstruction. AV-1.
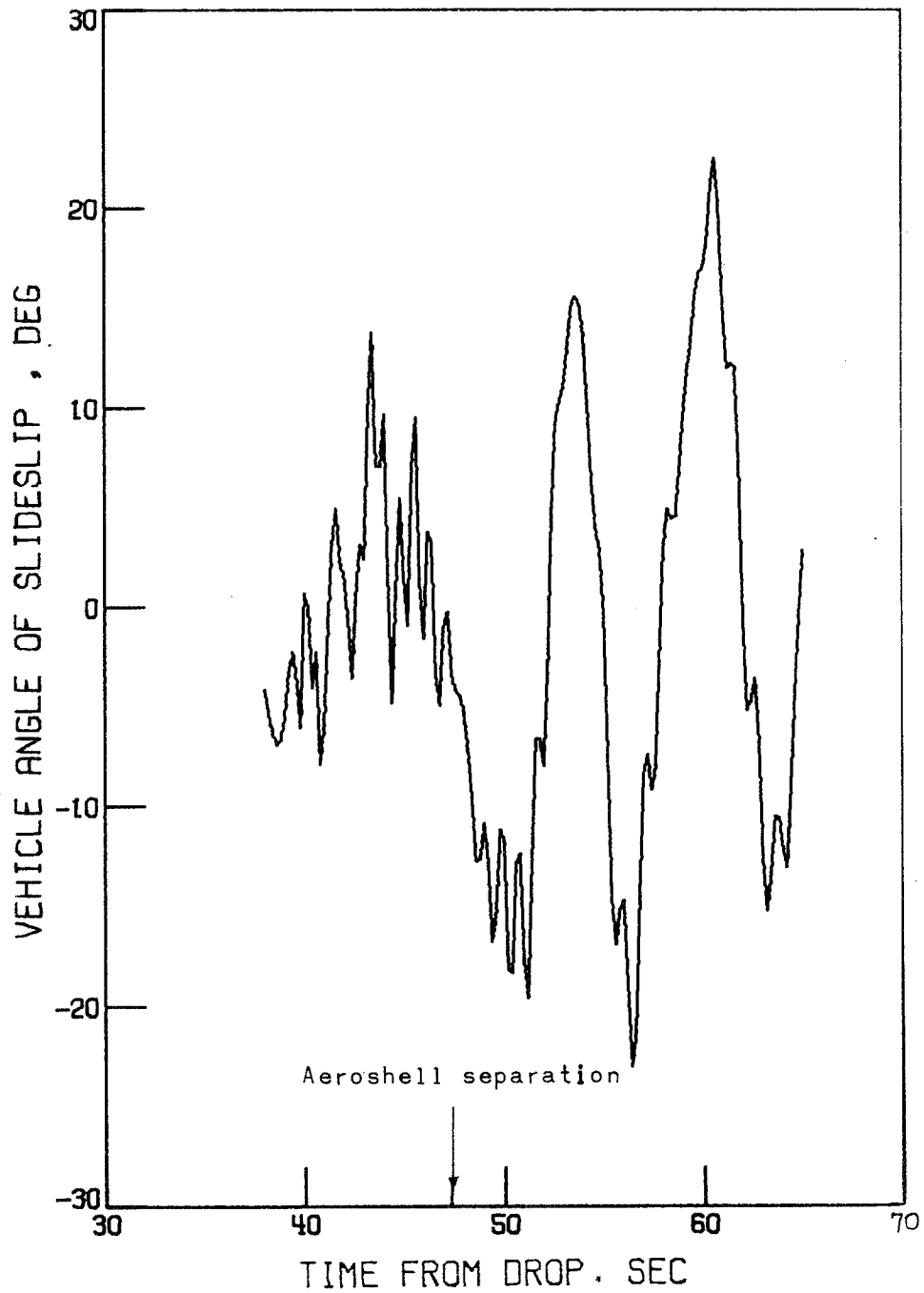
Figure 50.- History of vehicle angle of sideslip obtained from trajectory reconstruction. AV-2.
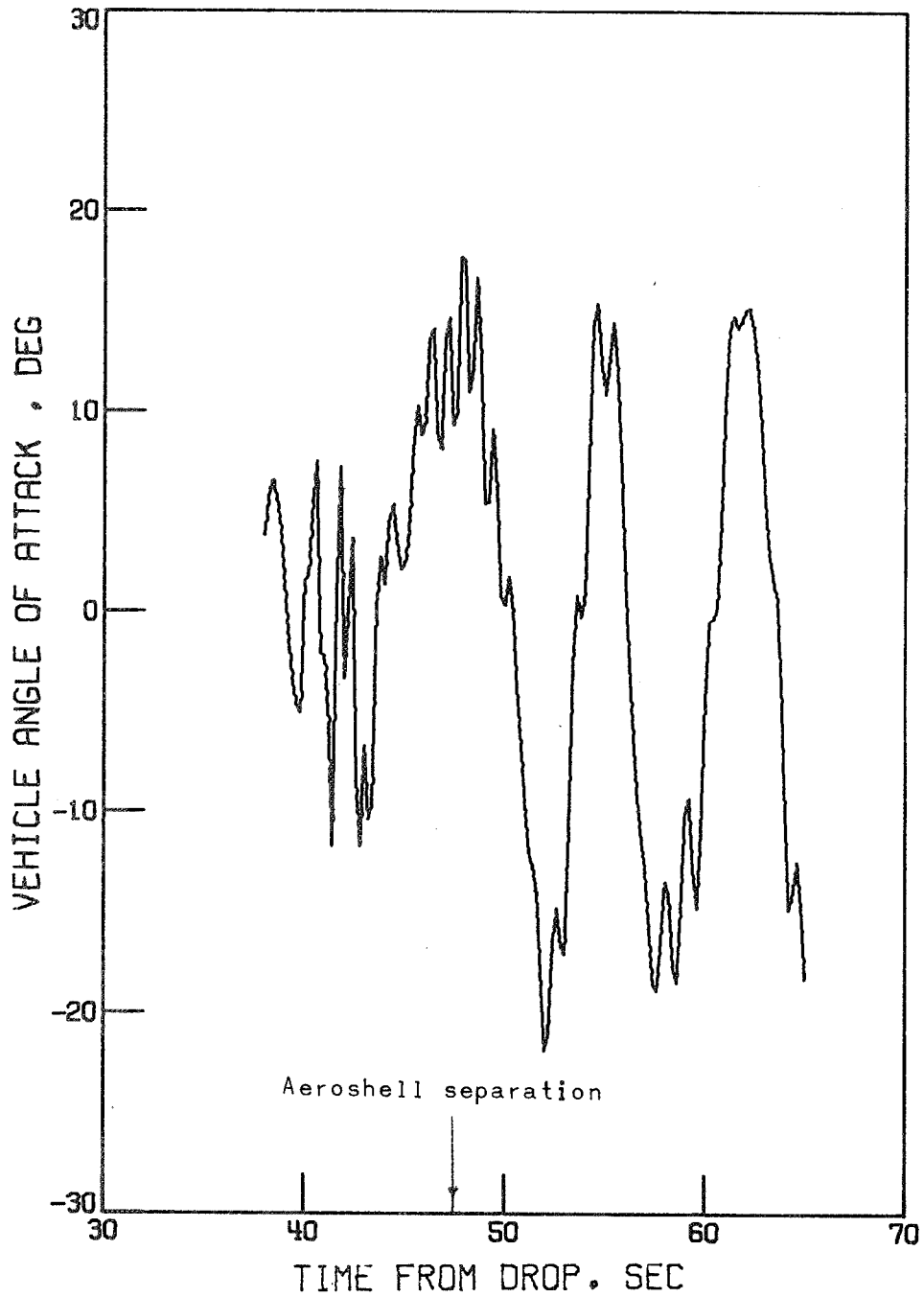
Figure 51.- History of vehicle angle of attack obtained from trajectory reconstruction. AV-2.
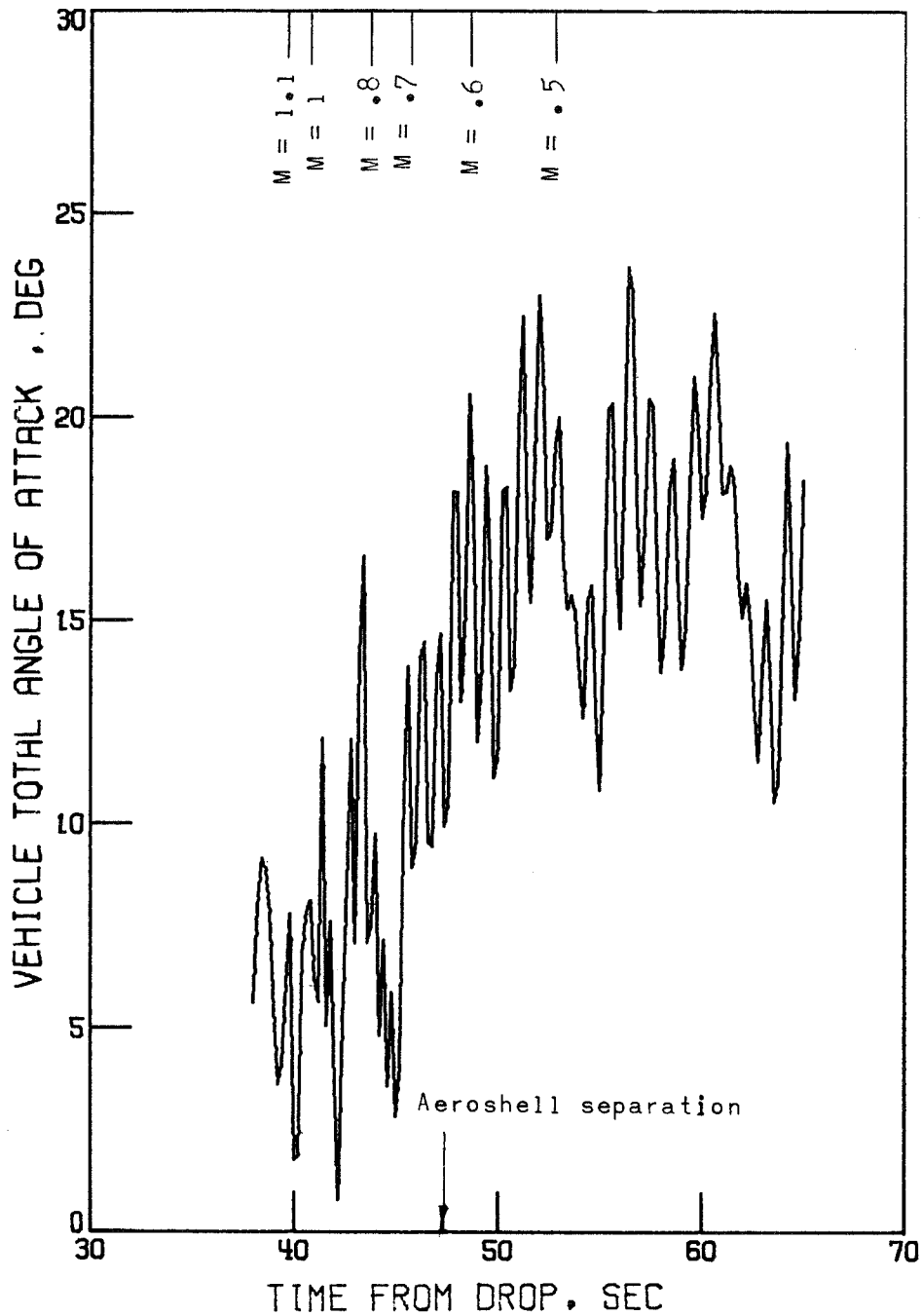
Figure 52.- History of vehicle total angle of attack obtained from trajectory reconstruction. AV-2.
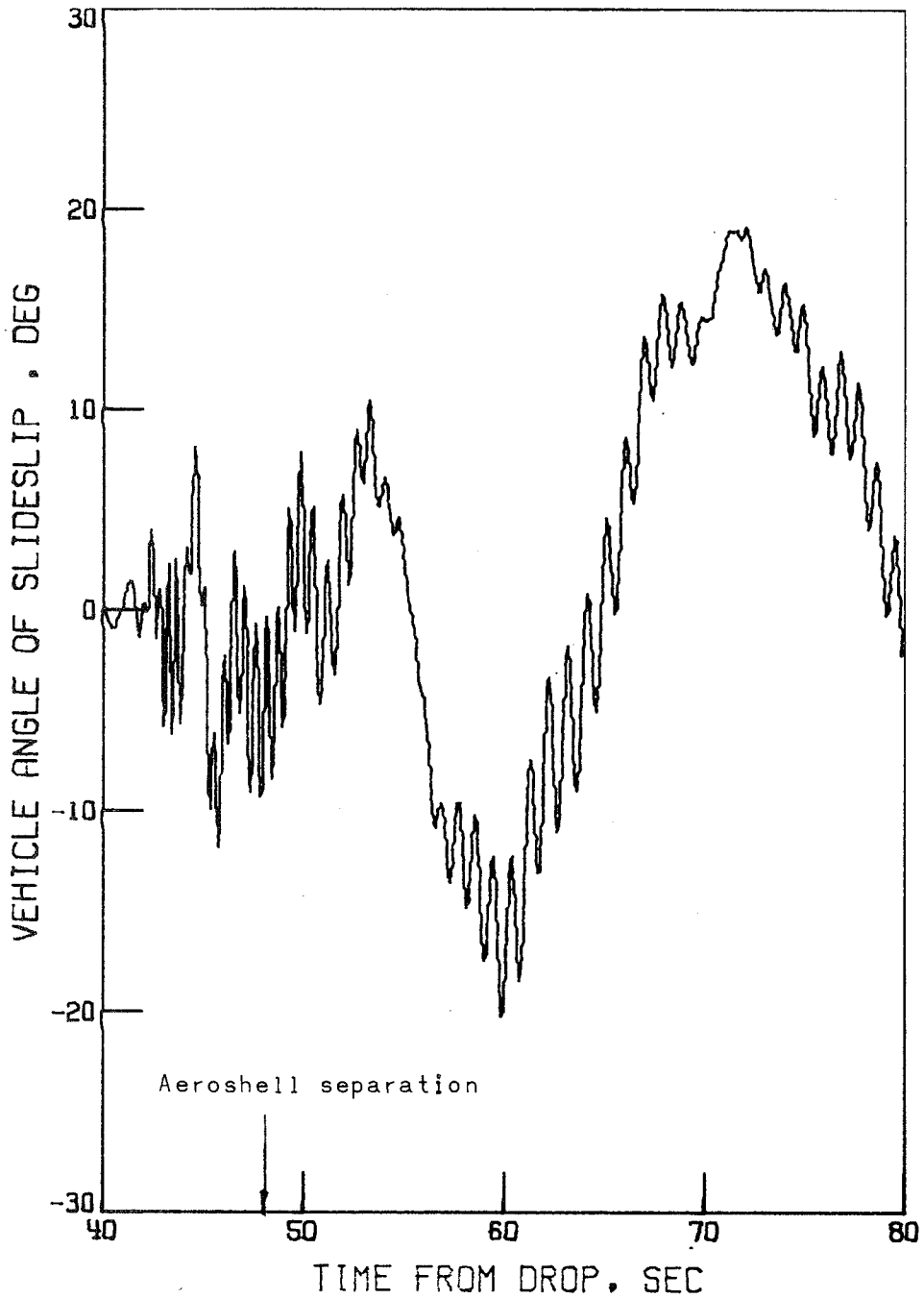
Figure 53.- History of vehicle angle of sideslip obtained from trajectory reconstruction. AV-4.
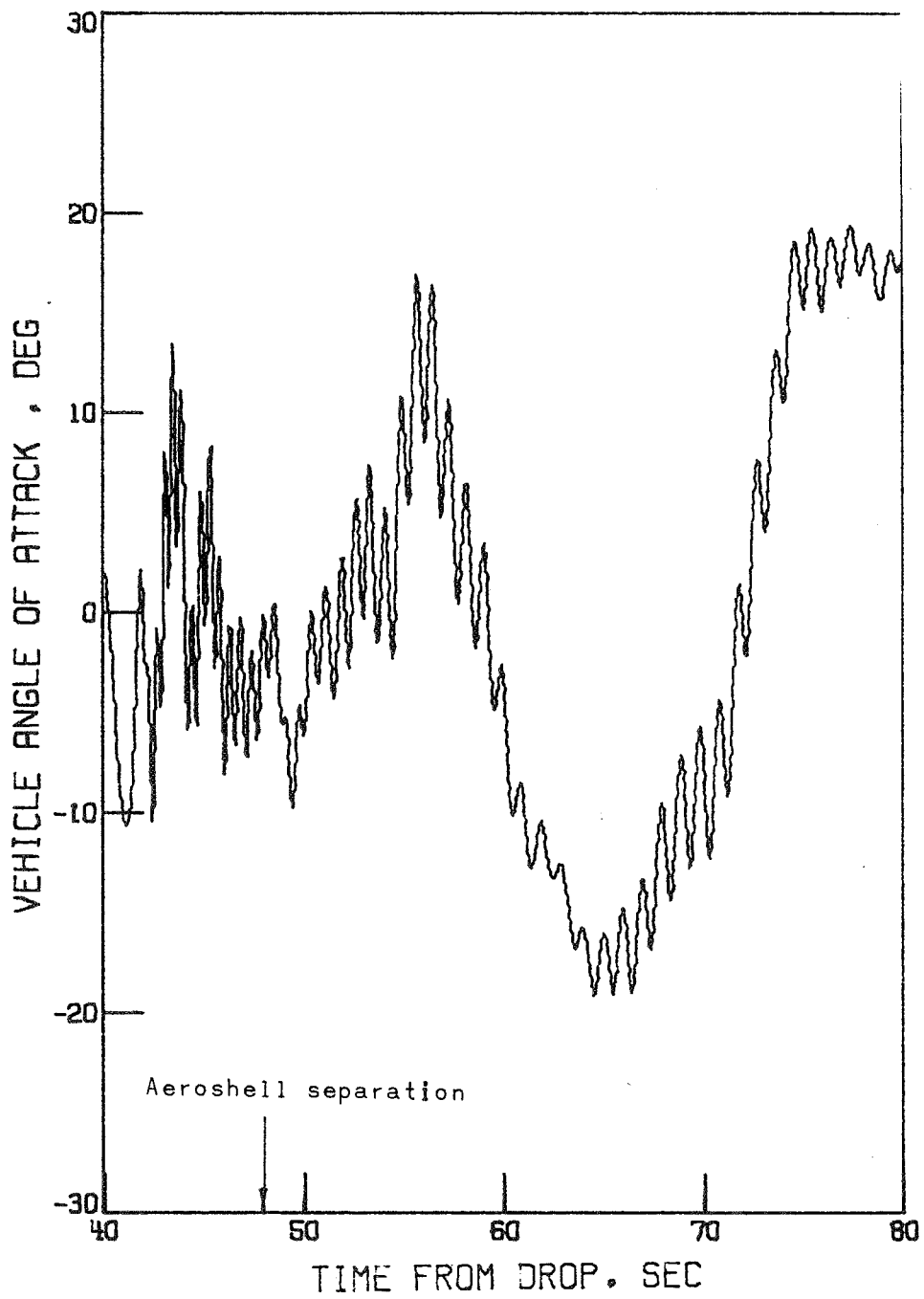
Figure 54.- History of vehicle angle of attack obtained from trajectory reconstruction.
AV-4.

Figure 55.- History of vehicle total angle of attack obtained from trajectory reconstruction. AV-4.
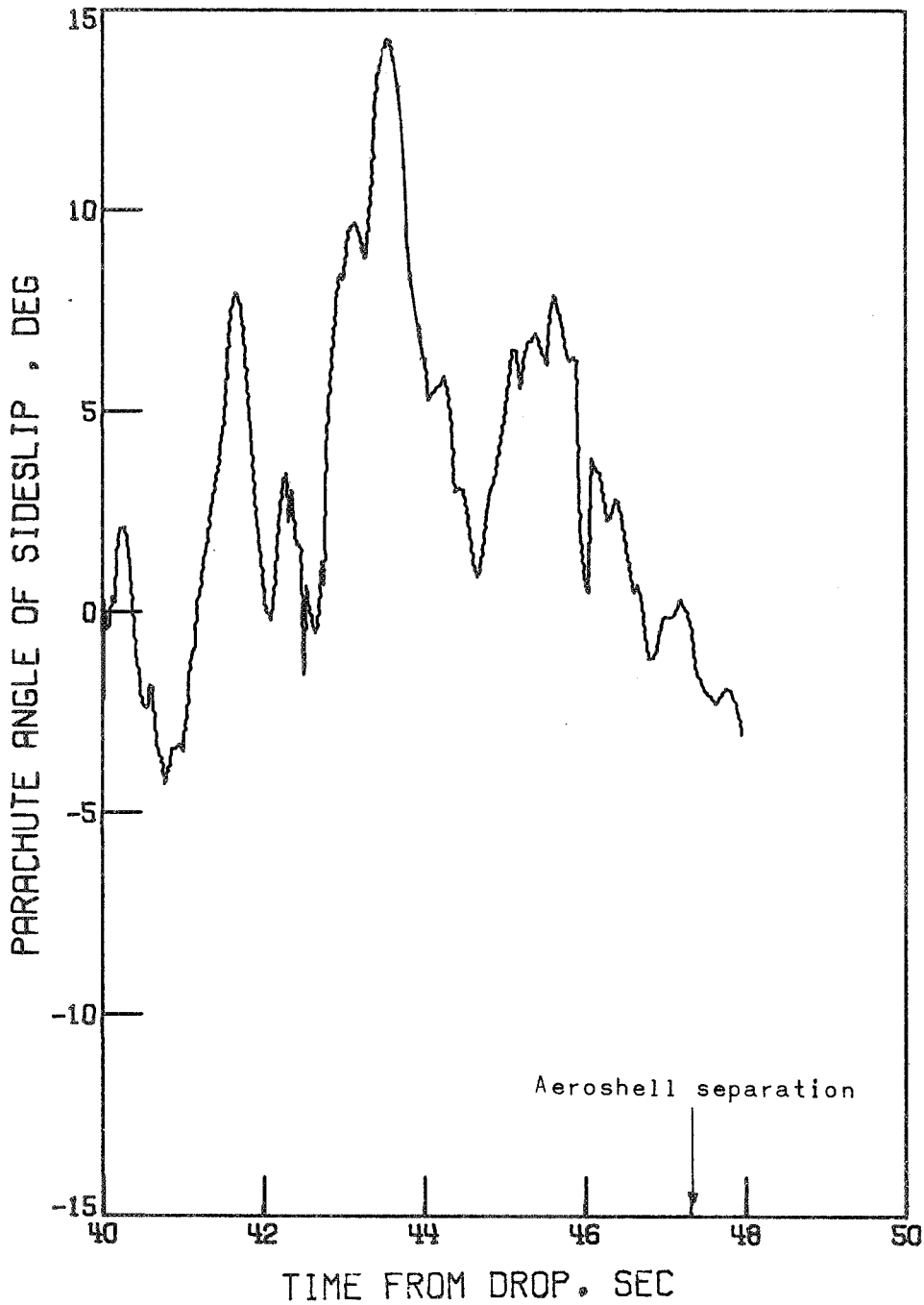
Figure 56.- Angle between the parachute axis and the relative wind projected on the spacecraft X,Y plane. AV-2.
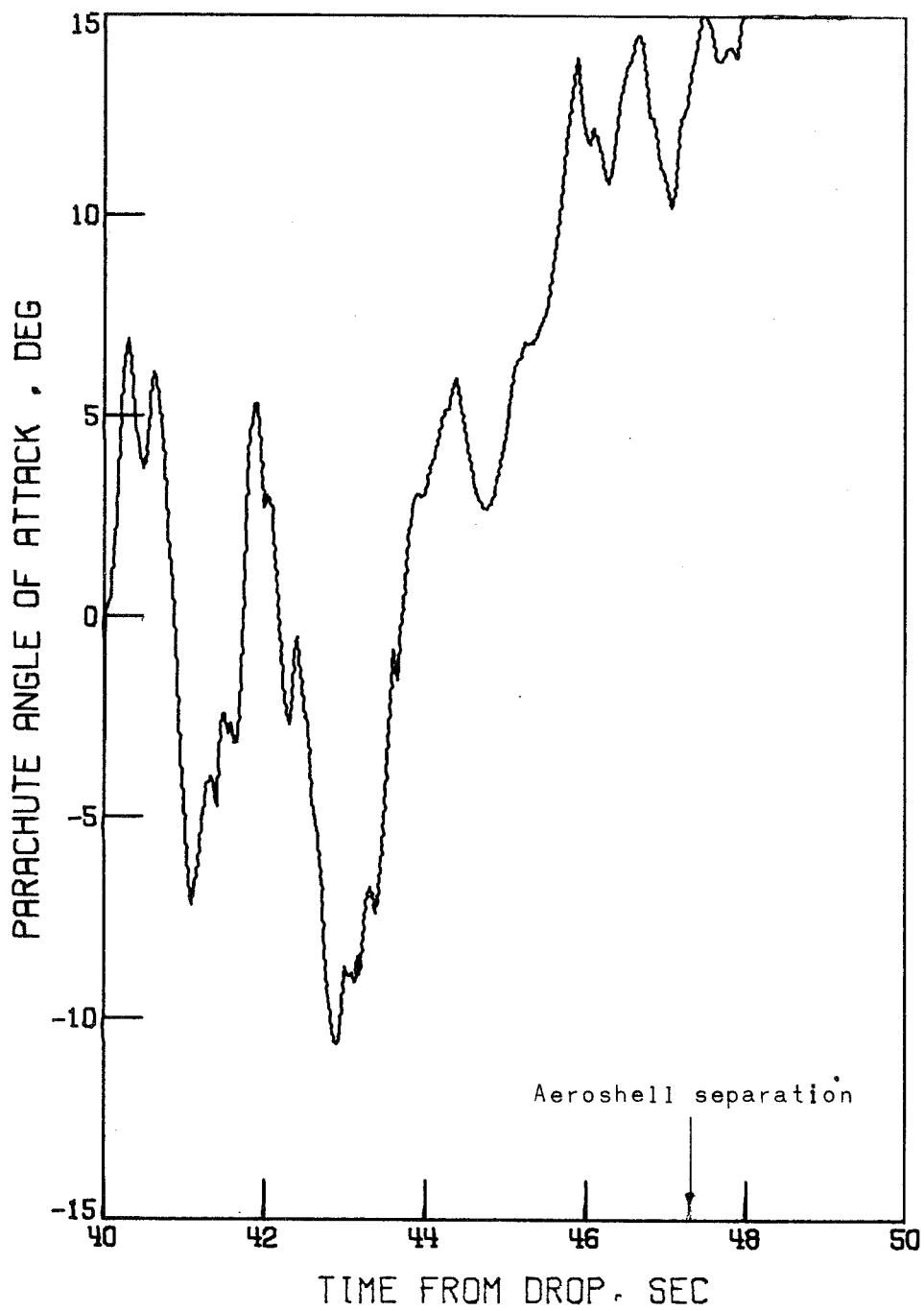
Figure 57.- Angle between the parachute axis and the relative wind projected on the spacecraft X,Z plane. AV-2.
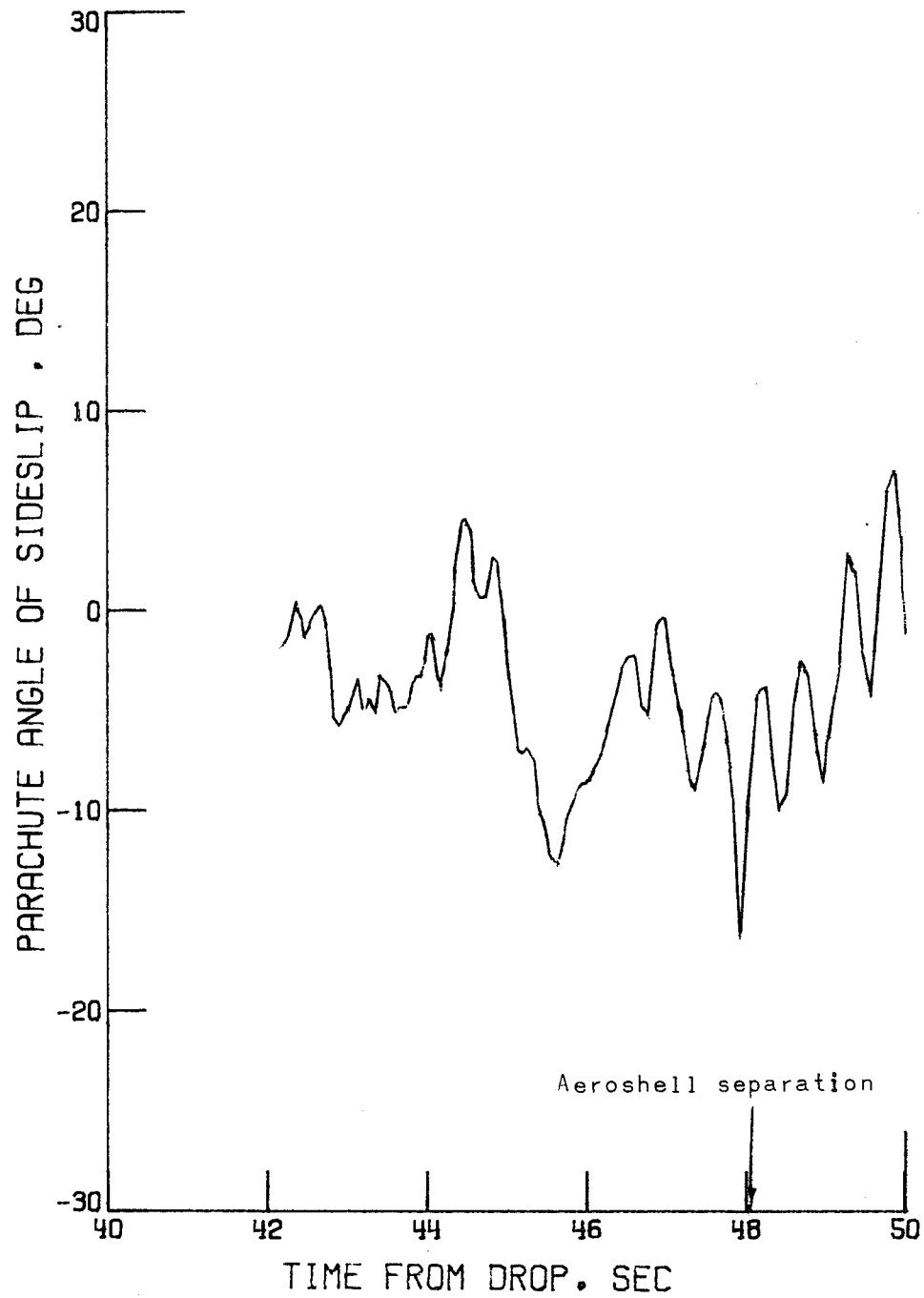
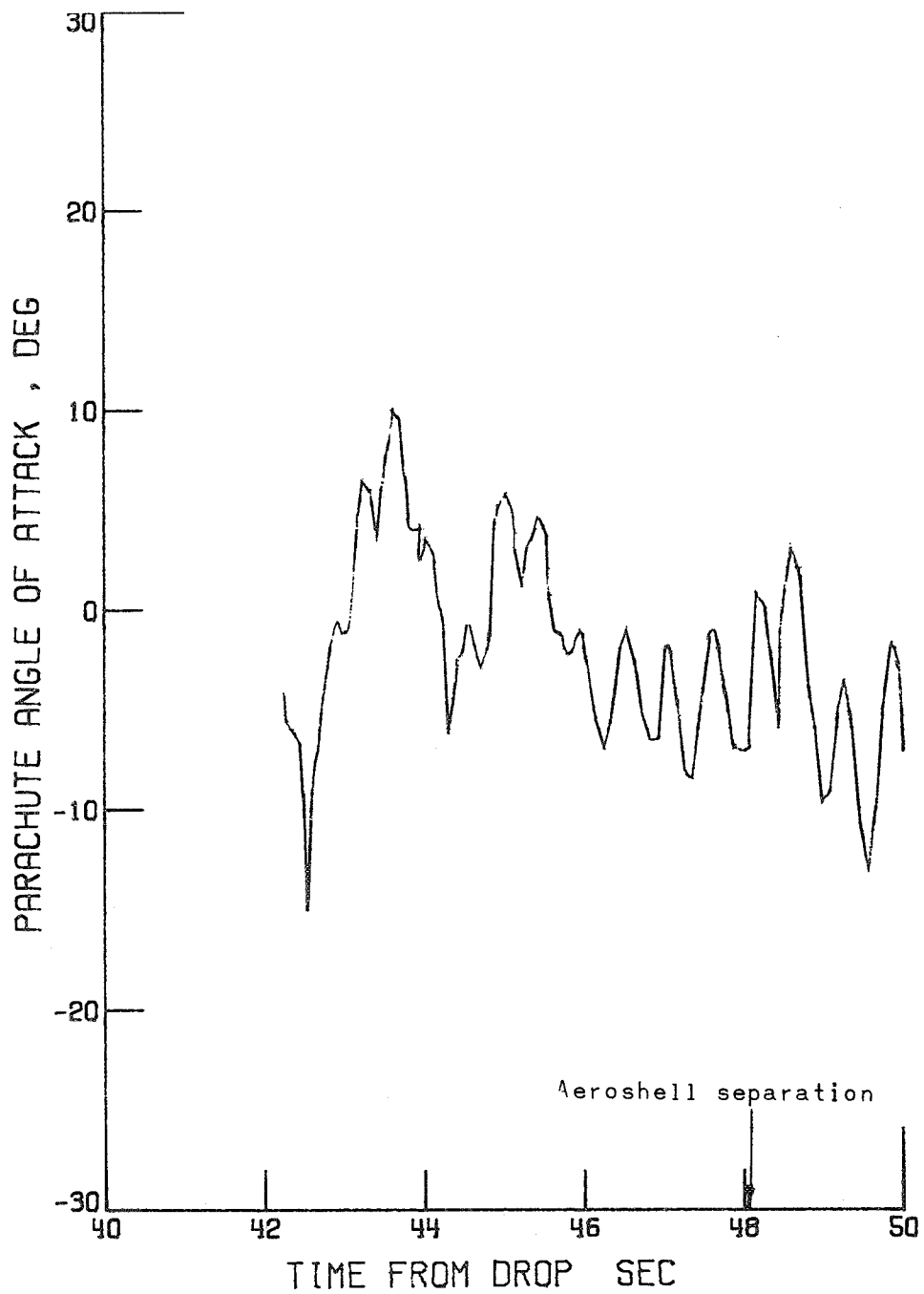Figure 58.- Angle between the parachute axis and the relative wind projected on the spacecraft X,Y plane. AV-4.

Figure 59.- Angle between the parachute axis and the relative wind projected on the spacecraft X,Z plane. AV-4.
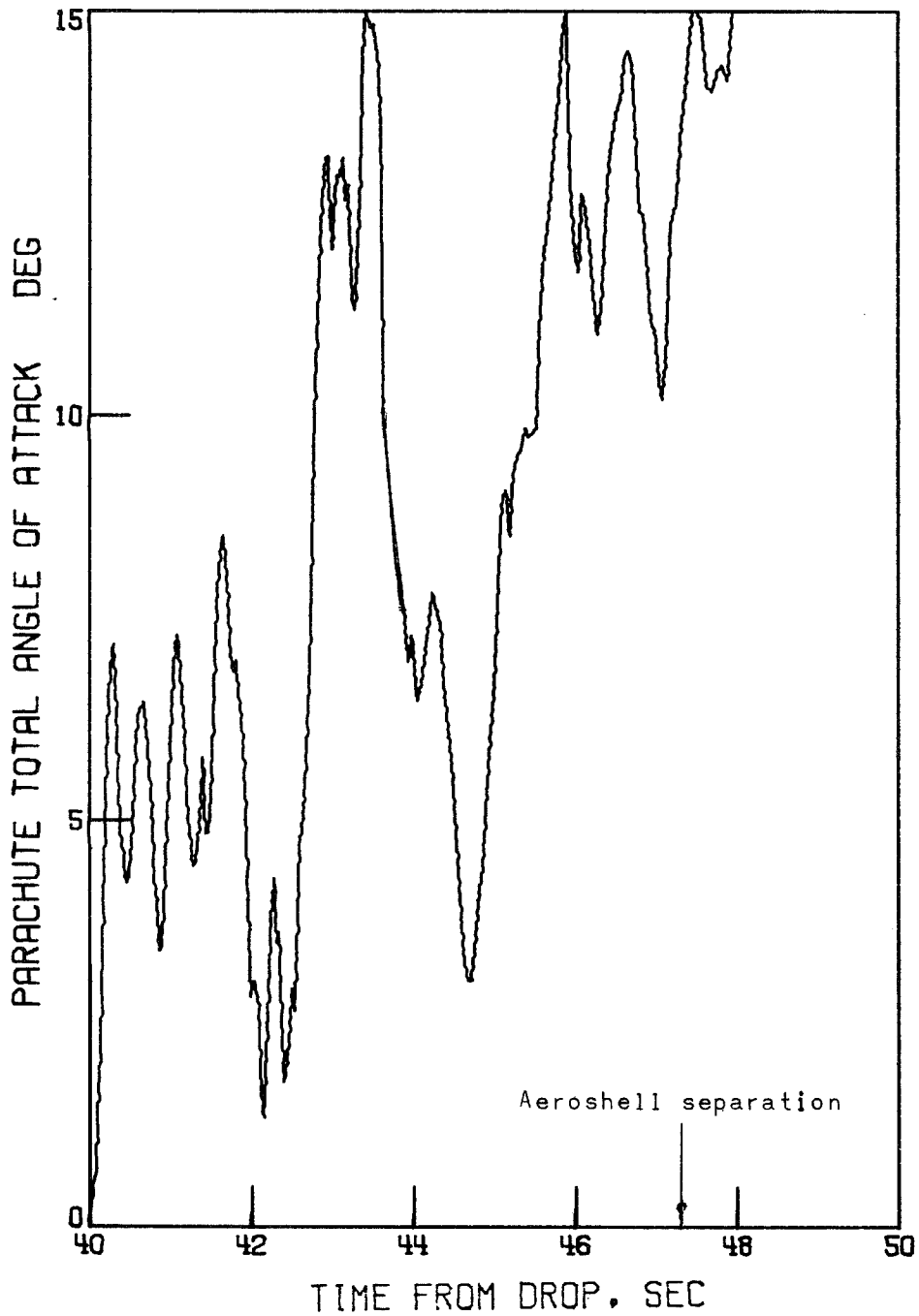
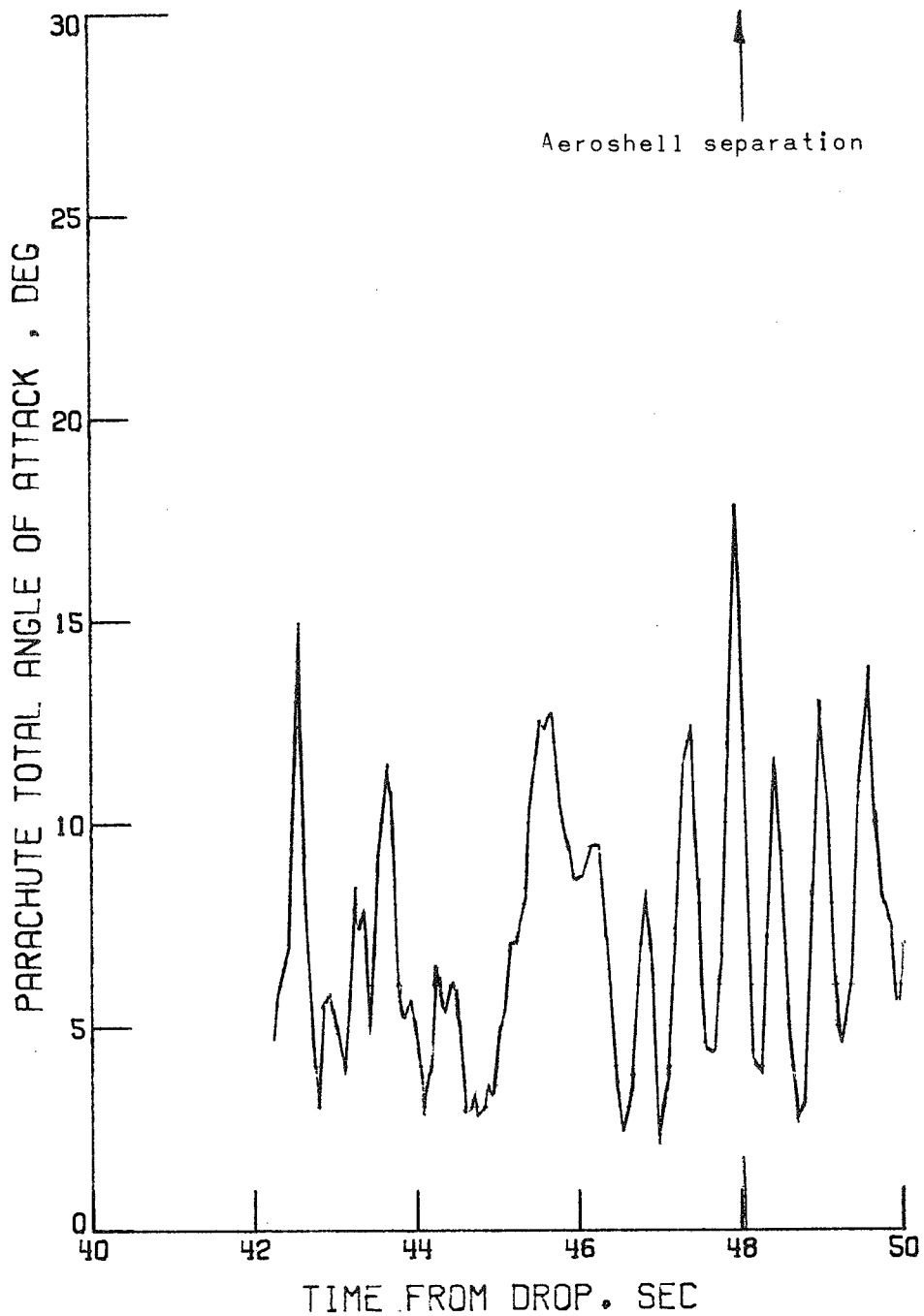Figure 60.- Angle between the parachute axis and the relative wind. AV-2.

Figure 61.- Angle between the parachute axis and the relative wind. AV-4.